Plasma Physics Reports, Vol. 30, No. 8, 2004, pp. 639–651. Translated from Fizika Plazmy, Vol. 30, No. 8, 2004, pp. 691–703.

DUSTY PLASMA

Stimulated Brillouin Scattering in a Dusty Plasma

K. Yu. Vagin, K. N. Ovchinnikov, V. P. Silin, and S. A. Uryupin

Lebedev Physical Institute, Russian Academy of Sciences, Leninskiĭ pr. 53, Moscow, 119991 Russia

Received April 24, 2003; in final form, November 12, 2003

Abstract—A kinetic description is developed for stimulated Brillouin scattering (SBS) in a dusty plasma with negatively charged dust grains. The threshold for SBS and the width of its spectral line are determined in the limits of weak and strong damping of the dust ion acoustic waves involved into the scattering process. For different mechanisms of the dissipation of dust ion acoustic waves, the threshold for SBS and the width of its spectral line are obtained as functions of the dust grain charge and the dust number density. © *2004 MAIK "Nauka/Interperiodica".*

1. INTRODUCTION

In recent years, considerable attention has been devoted to the study of dusty plasmas (see, e.g., [1–4]). A distinguishing feature of dusty plasma is that it contains heavy charged grains, whose mass M_d is much larger than the mass of the ions M_i and which can carry a fairly large effective electric charge Z_d. The wave properties of a dusty plasma differ from those of a conventional plasma: in particular, the presence of dust grains changes the wave spectra peculiar to the latter and gives rise to new waves, which show up even in such dusty plasmas that can easily be created under laboratory conditions [3]. This is exemplified by dust ion acoustic waves [5]. In view of the peculiar features of these waves, it is of interest to consider how they manifest themselves in a parametric instability such as stimulated Brillouin scattering (SBS).

Before proceeding to a description of the distinctive features of SBS in a dusty plasma, it is necessary to recall the known results on dust ion acoustic waves and on dusty plasma itself. In what follows, we will consider a plasma consisting of electrons, one ion species, and dust grains. The electroneutrality condition for such a plasma has the form

$$Z_i N_i = Z_d N_d + n_e, \tag{1.1}$$

where N_i is the ion density, n_e is the electron density, N_d is the dust number density, e is the charge of an electron, $|e|Z_i$ is the charge of an ion, and eZ_d is the charge of a grain. For simplicity, we assume that $Z_i = 1$. The usual practice is to speak of dusty plasma when the mass of the grains in the plasma is several orders of magnitude larger than that of the ions and the dust charge density is not too low in comparison to the electron (or ion) charge density, $Z_d N_d \sim N_i$. The latter condition is satisfied even for a plasma in which the dust number density N_d is relatively low, so that, owing to their large sizes, the grains can carry a rather large charge,

$$Z_d \gg 1. \tag{1.2}$$

In the case in which the grains acquire a negative charge primarily by absorbing the electrons that are incident on their surfaces, condition (1.1) gives $n_e < N_i$. In such a plasma, dust ion acoustic waves can exist that obey the dispersion relation [5]

$$\omega_S = k v_{S,di}, \tag{1.3}$$

and have the phase velocity

$$v_{S,di} = \omega_{Li} r_{De} = \sqrt{\frac{N_i}{n_e}\frac{\kappa_B T_e}{M_i}}, \tag{1.4}$$

where k is the wavenumber, $\omega_{Li} = \sqrt{4\pi e^2 N_i/M_i}$ is the ion Langmuir frequency, $r_{De} = \sqrt{\kappa_B T_e/4\pi e^2 n_e}$ is the electron Debye radius, T_e is the electron temperature, and κ_B is Boltzmann's constant. Note that, in this case, the dust ion acoustic velocity is higher than the thermal velocities of the ions and grains but is lower than the electron thermal velocity.

In this paper, we are interested in the distinctive features of SBS generated during the excitation of dust ion acoustic waves. This is why, in Sections 2 and 3, we present the relevant results on the contributions of the electrons, ions, and grains to the longitudinal dielectric function of the plasma. In Section 4, we present a method of deriving the spectrum of the dust ion acoustic waves and present the rates of collisional and collisionless damping of the dust ion sound by electrons, the rate of its collisionless damping by ions, and the rate of its damping due to collisions of ions with charged grains. In Section 5, we describe the results from investigations of SBS under conditions of the weak damping of dust ion acoustic waves. We obtain expressions for the threshold of SBS and for the width of its spectral line. We show that, in the range of large wavenumbers, the properties of SBS at the threshold and its spectral properties are associated with the collisionless Landau damping by electrons. In the range of smaller wavenumbers, the threshold for SBS and the width of its

1063-780X/04/3008-0639$26.00 © 2004 MAIK "Nauka/Interperiodica"

spectral line are determined by the dissipation of dust ion acoustic waves due to collisions of electrons and ions with grains. We investigate how the charge of dust grains and their number density influence the threshold intensity for SBS and its spectral line width. We derive the scaling formulas that describe the dependence of the threshold and spectral line width of the SBS on the charge and number density of the dust grains under conditions corresponding to different mechanisms for the dissipation of dust ion acoustic waves. We show that, under conditions such that the nonlocal nature of electron transport is important, the threshold and spectral line width of the SBS increase more rapidly with Z_d and N_d than they do in the limit of collisionless Landau damping but less rapidly than in the limit when the collisional damping by ions dominates. We also show that, in a dusty plasma in which the electron density is much lower than the ion density and in which collisional damping is governed by the ion plasma component, the threshold for SBS decreases with n_e. In Section 6, we study SBS under the conditions of strong collisionless damping of the dust ion sound by ions. Such conditions are of interest because they occur in dusty plasmas in which the temperatures of the components are nearly the same and the electron and ion densities are comparable in magnitude. In this case, the threshold intensity for SBS and its spectral line width are rather sensitive to the value of the ratio $N_i/n_e = 1 + Z_d N_d/n_e$, which in turn depends on the dust charge density. We show that, as the parameter $Z_d N_d$ increases, the dissipation of dust ion sound begins to be governed by the mechanism of weak Cherenkov dissipation (this limiting case is the subject of Section 5). In Section 7, we discuss the conditions under which the particle motion can be described by using the kinetic approach, which underlies the theory of SBS in dusty plasmas.

2. ELECTRON CONTRIBUTION TO THE DIELECTRIC FUNCTION OF A DUSTY PLASMA

Here, we consider the electron contribution to the dielectric function of a dusty plasma. Since the grain charge is large, $Z_d \gg 1$, the electron scattering is governed primarily by their collisions with dust grains and is characterized by the mean free path

$$l_{ed} = \frac{3}{4\sqrt{2\pi}} \frac{(\kappa_B T_e)^2}{e^4 Z_d^2 N_d \Lambda}, \tag{2.1}$$

where Λ is the Coulomb logarithm.

In what follows, we will be interested in dust ion acoustic waves with the frequency ω and wavenumber k. We consider conditions under which the electrons can be described in a weakly collisional approximation,

$$k l_{ed} \gg 1. \tag{2.2}$$

In this case, according to [6], the electron contribution to the dielectric function is given by the expression

$$\delta\varepsilon_e(\omega, k) = \frac{1}{k^2 r_{De}^2}\left\{1 + i\frac{\omega}{k v_{Te}}\left[\sqrt{\frac{\pi}{2}} + 2.2\frac{Z_{\text{eff}}^{2/7}}{(k l_{ed})^{3/7}}\right]\right\}, \tag{2.3}$$

where m_e is the mass of an electron, $v_{Te} = \sqrt{\kappa_B T_e/m_e}$ is the electron thermal velocity, and $Z_{\text{eff}} = Z_d^2 N_d/n_e \sim Z_d N_i/n_e$. The first two terms on the right-hand side of expression (2.3) describe the conventional collisionless electron contribution to the dielectric function of the plasma; this contribution is valid in the frequency range

$$\omega \ll k v_{Te}. \tag{2.4}$$

The second of these terms accounts for the dissipation due to collisionless Landau damping by electrons. The last term on the right-hand side of expression (2.3) describes the weakly collisional electron contribution to the plasma dielectric function [6]; this contribution is valid under conditions (1.2) and (2.2) in the range of sufficiently low frequencies:

$$\omega \ll \frac{k v_{Te}}{Z_{\text{eff}}^{5/7}(k l_{ed})^{3/7}} \ll k v_{Te}. \tag{2.5}$$

According to [6], dust ion acoustic perturbations with frequencies in range (2.5) only slightly affect the perturbation of the electron distribution and lead to small corrections that are linear in frequency ω. In frequency range (2.5), the formation of the electron distribution is highly sensitive to the nonlocal nature of the electron transport. In contrast, outside this frequency range, the nonlocal electron transport effects are unimportant.

3. CONTRIBUTION OF THE IONS AND DUST GRAINS TO THE DIELECTRIC FUNCTION OF A DUSTY PLASMA

Here, we derive expressions for the contributions of the ions and dust grains to the dielectric function of a dusty plasma. An expression for the collisional ion contribution to the longitudinal dielectric function, $\delta\varepsilon_i(\omega, k)$, was obtained in [7] in studying ion acoustic waves in a plasma with two ion species. In this expression, which was derived with the help of the Bhatnagar–Gross–Krook (BGK) collision integral, the main dissipative term is the one that describes the contribution from collisions between different ion species.

In a kinetic approach in which the potential energy of interaction between the particles is low in comparison to their kinetic energy, the distance between the particles is much greater than their sizes but is far less than the plasma Debye radius. Under such conditions, the grains can be regarded as massive pointlike charged particles similar to ions with a large charge. This approach makes it possible to use the results of [7, 8] to

describe the contributions of the positively charged ions and negatively charged grains to the longitudinal dielectric function of a dusty plasma. We take into account the facts that the charge-to-mass ratio of the grains is much smaller than that of the ions, $Z_d M_i/M_d \ll 1$, and that, along with this inequality, the condition $M_i N_i \ll M_d N_d$ usually holds with an ample margin for a dusty plasma. As a result, in accordance with [7, 8], we obtain the following expression for the collisional ion contribution to the dielectric function of a dusty plasma:

$$\delta\varepsilon_i(\omega, k) \equiv \delta\varepsilon_i'(\omega, k) + i\delta\varepsilon_i''(\omega, k) = -\frac{\omega_{Li}^2}{\omega^2}\left(1 - i\frac{\nu_{id}}{\omega}\right). \quad (3.1)$$

This expression is valid in the frequency range

$$\omega \gg k v_{Ti}, \nu_{id}, \quad (3.2)$$

which is characteristic of the dust ion sound. Here, $v_{Ti} = \sqrt{\kappa_B T_i/M_i}$ is the ion thermal velocity, T_i is the ion temperature, and $\nu_{id} = 4\sqrt{2\pi}e^4 Z_d^2 N_d \Lambda/[3\sqrt{M_i}(\kappa_B T_i)^{3/2}]$ is the ion–dust collision frequency. Expression (3.1) does not take into account the dissipative contribution due to Landau damping by the ions,

$$\delta\varepsilon_{i,L}''(\omega, k) = i\sqrt{\frac{\pi}{2}}\frac{\omega\omega_{Li}^2}{k^3 v_{Ti}^3}\exp\left(-\frac{\omega^2}{2k^2 v_{Ti}^2}\right), \quad (3.3)$$

which can be important in the wavenumber range

$$k v_{Ti} \gg \nu_{id}. \quad (3.4)$$

Expression (3.1) is certainly valid in the range of sufficiently small wavenumbers that do not satisfy inequality (3.4). This expression is also valid in the range of large wavenumbers (3.4), provided that the following inequality holds under conditions (3.2):

$$\frac{\nu_{id}}{\omega} \gg \sqrt{\frac{\pi}{2}}\frac{\omega^3}{k^3 v_{Ti}^3}\exp\left(-\frac{\omega^2}{2k^2 v_{Ti}^2}\right). \quad (3.5)$$

If the inequality opposite to inequality (3.5) is satisfied, then, instead of expression (3.1), the ion contribution to the dielectric function is collisionless and is described by the formula [9]

$$\delta\varepsilon_i(\omega, k) = \frac{1}{k^2 r_{Di}^2}\left[1 - \frac{\sqrt{2}\omega}{k v_{Ti}}F\left(\frac{\omega}{\sqrt{2}k v_{Ti}}\right) + i\sqrt{\frac{\pi}{2}}\frac{\omega}{k v_{Ti}}\exp\left(-\frac{\omega^2}{2k^2 v_{Ti}^2}\right)\right], \quad (3.6)$$

where $r_{Di} = \sqrt{\kappa_B T_i/4\pi e^2 N_i}$ is the ion Debye radius and $F(x) = \exp(-x^2)\int_0^x dt \exp(t^2)$ is the Dawson integral. Hence, expressions (3.1) and (3.6) describe the ion contribution to the dielectric function of a dusty plasma in the limit in which the dissipation of dust ion acoustic waves is governed by the ion–dust collisions and in the collisionless limit.

For frequencies ω satisfying condition (3.2), expression (3.6) can be rewritten in a simple form:

$$\delta\varepsilon_i(\omega, k) = -\frac{\omega_{Li}^2}{\omega^2}\left[1 - i\sqrt{\frac{\pi}{2}}\frac{\omega^3}{k^3 v_{Ti}^3}\exp\left(-\frac{\omega^2}{2k^2 v_{Ti}^2}\right)\right]. \quad (3.7)$$

Note that, for frequencies satisfying condition (3.2) in both collisional limit (3.1) and collisionless limit (3.7), the imaginary part of the ion contribution $\delta\varepsilon_i(\omega, k)$ is much smaller than its real part; this means that the dissipation is relatively weak.

4. DAMPING OF DUST ION SOUND

In the long-wavelength limit

$$k r_{De} \ll 1 \quad (4.1)$$

and in the range

$$v_{Ti} \ll \omega/k \ll v_{Te}, \quad (4.2)$$

the dispersion relation for longitudinal perturbations with the frequency ω and wavenumber k,

$$\delta\varepsilon_e(\omega, k) + \delta\varepsilon_i(\omega, k) = 0 \quad (4.3)$$

has a solution in the form of (3.1). This solution to dispersion relation (4.3) corresponds to dust ion acoustic waves that propagate with velocity (1.4) and are weakly damped at the rate

$$\gamma_S = \gamma_e + \gamma_i \ll \omega_S. \quad (4.4)$$

In expression (4.4), the rate of damping of the dust ion acoustic waves by electrons has the form

$$\gamma_e = \frac{k v_{S,di}^2}{v_{Te}}\left[\sqrt{\frac{\pi}{8}} + 1.1\frac{Z_{\text{eff}}^{2/7}}{(k l_{ed})^{3/7}}\right]. \quad (4.5)$$

The first term on the right-hand side of expression (4.5) describes collisionless Landau damping of the dust ion acoustic waves by electrons. The second term accounts for the damping of dust ion sound due to infrequent collisions of slow subthermal electrons in a dusty plasma in which the thermal electrons are collisionless. This second term is valid under the conditions

$$1 \ll k l_{ed} \ll \frac{(v_{Te}/v_{S,di})^{7/3}}{Z_{\text{eff}}^{5/3}}, \quad (4.6)$$

which are satisfied for a plasma in which the dust grains carry moderate electric charges:

$$Z_{\text{eff}} = \frac{Z_d^2 N_d}{n_e} \sim Z_d\frac{N_i}{n_e} \ll \left(\frac{v_{Te}}{v_{S,di}}\right)^{7/5}. \quad (4.7)$$

In this case, if the inequality $v_{Te}/v_{S,di} < Z_{\rm eff}$ holds under condition (4.7), then, over the entire range of wavenumbers (4.6), the collisional damping of dust ion acoustic waves by electrons predominates over collisionless Landau damping. For smaller grain charges, $Z_{\rm eff} < v_{Te}/v_{S,di}$, the collisional damping by electrons predominates over the collisionless damping in a narrower wavenumber range, $1 \ll kl_{ed} < Z_{\rm eff}^{2/3}$. For dusty plasmas in which the grain charge is fairly large and fails to satisfy inequality (4.7) and for large wavenumbers that lie beyond range (4.6), the second term in expression (4.5) cannot be used to describe collisional damping by electrons (see [10]).

Expression (4.4) also contains the rate of damping of the dust ion acoustic waves by ions, γ_i. In the wavenumber range

$$1 \ll \frac{kv_{S,di}}{\nu_{id}} \ll \sqrt{\frac{2}{\pi}}\left(\frac{v_{Ti}}{v_{S,di}}\right)^3 \exp\left(\frac{v_{S,di}^2}{2v_{Ti}^2}\right), \qquad (4.8)$$

and under inequalities (3.2) and (3.5), the damping rate γ_i is determined mainly by collisions of ions with charged dust grains (see also [11]):

$$\gamma_i = \nu_{id}/2. \qquad (4.9)$$

In the range of large wavenumbers that fail to satisfy the right-hand side inequality in conditions (4.8), the damping rate γ_i is governed by collisionless Landau damping, so that we have

$$\gamma_i = \sqrt{\frac{\pi}{8}}\frac{kv_{S,di}^4}{v_{Ti}^3}\exp\left(-\frac{v_{S,di}^2}{2v_{Ti}^2}\right). \qquad (4.10)$$

Note that, for dust ion acoustic waves obeying dispersion relation (1.3) and having velocity (1.4), inequalities (4.2) are equivalent to the following restrictions on the plasma parameters: $m_e/M_i \ll n_e/N_i \ll T_e/T_i$.

Under conditions such that $v_{S,di} \sim v_{Ti}$, the collisionless dissipation by ions is significant and the solution to dispersion relation (4.3) describes strongly damped dust ion acoustic waves, whose velocity and damping rate can be determined by numerical simulations.

5. STIMULATED BRILLOUIN SCATTERING UNDER CONDITIONS OF THE WEAK DAMPING OF DUST ION ACOUSTIC MODES

Here, we consider a parametric instability such as SBS. We treat the problem in a formulation that makes it possible to study how the instability evolves with time. We describe SBS by the dispersion relation [12, 13]

$$\frac{1}{\delta\varepsilon_i(\omega,k)} + \frac{1}{\delta\varepsilon_e(\omega,k)} = \frac{k^2|(\mathbf{k}-\mathbf{k}_0)\times\mathbf{v}_E|^2}{4(\mathbf{k}-\mathbf{k}_0)^2\{c^2(\mathbf{k}-\mathbf{k}_0)^2 - (\omega-\omega_0)^2\varepsilon_{\rm tr}(\omega-\omega_0,\,\mathbf{k}-\mathbf{k}_0)\}}. \qquad (5.1)$$

Here, ω_0 and $\mathbf{k}_0$ are the frequency and wave vector of an incident electromagnetic wave; $\omega_0 - \omega$ and $\mathbf{k}_0 - \mathbf{k}$ are the frequency and wave vector of the scattered wave; ω and $\mathbf{k}$ are the frequency and wave vector of an ion acoustic mode involved in the SBS process; $\mathbf{v}_E = e\mathbf{E}_0/m_e\omega_0$ is the electron oscillatory velocity in the field of the incident wave; and the transverse dielectric function $\varepsilon_{\rm tr}$ is given by the expression

$$\varepsilon_{\rm tr}(\omega-\omega_0,\,\mathbf{k}-\mathbf{k}_0) = 1 - \frac{\omega_{Le}^2}{(\omega-\omega_0)^2}\left(1 - i\frac{\nu_{ed}}{\omega-\omega_0}\right), \qquad (5.2)$$

where $\nu_{ed} = v_{Te}/l_{ed}$ is the frequency of collisions of the electrons with dust grains and ω_{Le} is the electron Langmuir frequency. The frequency in Eq. (5.1) is generally complex, $\omega \longrightarrow \omega + i\gamma$, where γ is the temporal growth rate of the ion acoustic mode and, consequently, of the scattered wave produced by it. In what follows, however, we will assume that the frequency ω is real.

In accordance with [12, 13], we invoke the notion of the frequency detuning from resonance in order to write the denominator of the right-hand side of Eq. (5.1) in its conventional form:

$$(\omega-\omega_0)^2{\rm Re}[\varepsilon_{\rm tr}(\omega-\omega_0,\,\mathbf{k}-\mathbf{k}_0)] - c^2(\mathbf{k}-\mathbf{k}_0)^2 = 2\omega_0\Delta, \qquad (5.3)$$

where Δ is the deviation from the parametric resonance frequency.

We are interested in the possible onset and development of an instability that grows with time at the rate

$$\gamma \ll \omega. \qquad (5.4)$$

In our analysis, the development of the SBS instability is attributed to the dust ion sound. First, we consider the simplest case in which the dusty plasma conditions correspond to a weak damping of the dust ion acoustic modes that are involved in the SBS process and whose phase velocity satisfies condition (4.2). Substituting expression (2.3) for $\delta\varepsilon_e$ and expression (3.1) or (3.7) for

$\delta\varepsilon_i$ into Eq. (5.1) and using formula (5.3), we can obtain the following set of equations for Δ and γ:

$$\frac{\omega^2}{\omega_S^2} - 1 = I\gamma_E \frac{\Delta}{\Delta^2 + (\gamma + \gamma_E)^2}, \quad (5.5)$$

$$2\frac{\gamma + \gamma_S}{\omega_S} = I\gamma_E \frac{\gamma + \gamma_E}{\Delta^2 + (\gamma + \gamma_E)^2}. \quad (5.6)$$

Here, $\gamma_E = \nu_{ed}\omega_{Le}^2/(2\omega_0^2)$ is the damping rate of the transverse electromagnetic wave due to its absorption in collisions of electrons with charged dust grains;

$$I = \frac{\omega_0}{\nu_{ed}} \frac{|(\mathbf{k} - \mathbf{k}_0) \times \mathbf{v}_E|^2}{4(\mathbf{k} - \mathbf{k}_0)^2 v_{Te}^2} \quad (5.7)$$

is the dimensionless pump field intensity; and ω_S and γ_S are given by expressions (1.3) and (4.4), respectively. Equations (5.5) and (5.6) are linear in the small parameters γ_S/ω_S and γ/ω.

These equations yield the following expression for the frequency detuning:

$$\Delta = (\gamma + \gamma_E)\frac{\omega^2 - \omega_S^2}{2\omega_S(\gamma + \gamma_S)}. \quad (5.8)$$

Accordingly, the growth rate γ satisfies the equation

$$\frac{\gamma + \gamma_E}{\gamma_E}\left[\frac{(\omega^2 - \omega_S^2)^2}{2\omega_S^3(\gamma + \gamma_S)} + \frac{2(\gamma + \gamma_S)}{\omega_S}\right] = I, \quad (5.9)$$

which yields the following equation for the boundary ($\gamma = 0$) of the instability region:

$$\frac{(\omega^2/\omega_S^2 - 1)^2}{2\gamma_S/\omega_S} + 2\gamma_S/\omega_S = I. \quad (5.10)$$

Equation (5.10) describes the spectral line width of the SBS: it determines the dependence of the frequency ω at the boundary of the instability region on the pump field intensity I. The instability threshold corresponds to the minimum pump intensity I_{th} at which the damping rate of the dust ion acoustic mode vanishes, $\gamma = 0$, and its frequency is equal to ω_{th}. From Eq. (5.10) at the instability threshold, we obtain the relationships (cf. [12])

$$I = I_{\text{th}} = 2\frac{\gamma_S}{\omega_S}, \quad (5.11)$$

$$\omega = \omega_{\text{th}} = \omega_S. \quad (5.12)$$

Using these relationships, we can write the frequency ω_b at the instability boundary as

$$\omega_{b\pm} = \omega_{\text{th}} \pm \gamma_S\sqrt{I/I_{\text{th}} - 1}. \quad (5.13)$$

Formula (5.13) is applicable over a fairly wide range of pump field intensities,

$$I_{\text{th}} \le I \ll 2\omega_S/\gamma_S. \quad (5.14)$$

It should be noted that, according to Eq. (5.9), the instability growth rate γ, as a function of the pump field intensity I, is positive over the frequency range $\omega_{b-} \le \omega \le \omega_{b+}$.

Formula (5.13) gives the following expression for the spectral line width of the SBS:

$$\Delta\omega \equiv \omega_{b+} - \omega_{b-} = 2\gamma_S\sqrt{I/I_{\text{th}} - 1}. \quad (5.15)$$

Far above the threshold ($I \gg I_{\text{th}}$), the spectral line width increases as the square root of the pump field intensity.

In order to better understand what the restrictions are that may be imposed on the range of applicability of linear theory, we analyze the expression for the instability growth rate. For simplicity, we consider the growth rate at $\omega = \omega_{\text{th}} = \omega_S$, in which case Eq. (5.9) yields

$$\gamma = \frac{1}{2}\{\sqrt{(\gamma_S - \gamma_E)^2 + 2\gamma_E\omega_S I} - (\gamma_S + \gamma_E)\}. \quad (5.16)$$

For pump intensities that are sufficiently far above the threshold, we have

$$\gamma = \sqrt{\gamma_E\omega_S I/2}. \quad (5.17)$$

From this expression we can see that, in the case at hand, the above condition for the growth rate of the SBS instability to be low in comparison to the frequency of the dust ion acoustic waves (see condition (5.4)) reduces to the inequality

$$I \ll 2\omega_S/\gamma_E. \quad (5.18)$$

Let us discuss how the presence of dust affects the spectral properties of the SBS as well as its properties at the threshold. First of all, note that, in a plasma with negatively charged dust, the frequency shift of SBS is larger than that in a dust-free plasma with the same ion composition, the same particle temperatures, and the same ion density. The reason is that the velocity $v_{S,di}$ of the dust ion acoustic waves, which determines the frequency shift of SBS (see expression (1.4)), is $\sqrt{N_i/n_e} > 1$ times higher than the velocity of the conventional ion acoustic waves, which determines the frequency shift in a dust-free plasma. An increase in the dust charge density $Z_d N_d$ leads to an increase in the ratio N_i/n_e and, therefore, in the frequency shift of the SBS.

The increase in the velocity $v_{S,di}$ of dust ion acoustic waves that is caused by an increase in the dust charge density also changes the threshold for SBS and the width of its spectral line. It is the change in the velocity $v_{S,di}$ that changes the threshold and spectral line width of the SBS under conditions in which the dissipation of dust ion acoustic waves is determined by the collisionless Landau damping by electrons (see the first term in expression (4.5)) and by ions (see expression (4.10)).

In this case, as the ratio $v_{S,di}/v_{Ti}$ increases, the collisionless Landau damping by ions becomes less intense and, when the values of the ratio $v_{S,di}/v_{Ti}$ are several times larger than unity, it becomes unimportant over a broad range (4.8) of wavenumbers k. Under conditions corresponding to this limit, damping rate (4.4) of the dust ion acoustic waves has the form

$$2\gamma_S = \nu_{id} + \frac{k v_{S,di}^2}{v_{Te}}\left[\sqrt{\frac{\pi}{2}} + 2.2\frac{Z_{\text{eff}}^{2/7}}{(k l_{ed})^{3/7}}\right]. \quad (5.19)$$

With expression (5.19), formulas (5.11) and (5.15) for the threshold and spectral line width of the SBS can be written as

$$\frac{|(\mathbf{k}-\mathbf{k}_0)\times\mathbf{v}_E|_{\text{th}}^2}{4(\mathbf{k}-\mathbf{k}_0)^2 v_{Te}^2} = \frac{2\gamma_S}{k v_{S,di}}\frac{\nu_{ed}}{\omega_0}, \quad (5.20)$$

$$\Delta\omega = 2\gamma_S\sqrt{\frac{|(\mathbf{k}-\mathbf{k}_0)\times\mathbf{v}_E|^2}{|(\mathbf{k}-\mathbf{k}_0)\times\mathbf{v}_E|_{\text{th}}^2} - 1}. \quad (5.21)$$

Hence, the threshold for SBS is determined by the product of the two quantities that depend on the parameters of the dust plasma component: (i) the ratio of the slow damping rate γ_S of the longitudinal dust ion acoustic waves involved in the SBS process to their frequency and (ii) the small ratio ν_{ed}/ω_0, which is associated with the damping of the electromagnetic wave that is scattered due to electron–dust collisions in the plasma. For a dusty plasma, the ratio ν_{ed}/ω_0 is larger than that for a dust-free plasma with the same ion density by a factor of $Z_d^2 N_d/N_i \sim Z_d \gg 1$; this indicates that, in the former, the damping of electromagnetic waves is more intense and the threshold for SBS is higher. In turn, at a fixed amount by which the pump field intensity exceeds the threshold, spectral line width (5.21) of the SBS is directly proportional to growth rate (5.19) of the dust ion acoustic waves. The first term on the right-hand side of expression (5.19) refers to the dissipation of dust ion acoustic waves due to ion–dust collisions. The second term describes the collisionless Landau damping of these waves by electrons. The last (third) term accounts for the influence of the electron–dust collisions on the damping of dust ion acoustic waves with sufficiently small wavenumbers (4.6) under conditions where the nonlocal nature of electron transport is important.

Condition (4.7) fails to hold for a dusty plasma in which the grains carry a large charge. In this case, the last term drops out of expression (5.19) and the damping rate of the dust ion acoustic waves is determined by a competition between the two effects described by the first two terms in this expression. In the range of large wavenumbers such that $\nu_{id} v_{Te}/v_{S,di}^2 \ll k \ll r_{De}^{-1}$, the dissipation of dust ion acoustic modes is governed mainly by the collisionless Landau damping by electrons, in which case the expressions for the threshold and spectral line width of the SBS can be written in the following simple form:

$$\frac{|(\mathbf{k}-\mathbf{k}_0)\times\mathbf{v}_E|_{\text{th}}^2}{4(\mathbf{k}-\mathbf{k}_0)^2 v_{Te}^2} = \sqrt{\frac{\pi}{2}}\frac{v_{S,di}}{v_{Te}}\frac{\nu_{ed}}{\omega_0} \sim \sqrt{\frac{N_i}{n_e}} Z_d^2 N_d, \quad (5.22)$$

$$\Delta\omega = \sqrt{\frac{\pi}{2}}\frac{k v_{S,di}^2}{v_{Te}}\sqrt{\frac{|(\mathbf{k}-\mathbf{k}_0)\times\mathbf{v}_E|^2}{|(\mathbf{k}-\mathbf{k}_0)\times\mathbf{v}_E|_{\text{th}}^2} - 1} \sim \frac{N_i}{n_e}. \quad (5.23)$$

From expression (5.22) we can see that the larger the grain charge and the higher the dust number density, the higher the instability threshold. We stress that, if the dust charge density is so high that $Z_d N_d \approx N_i$, and if, by virtue of electroneutrality condition (1.1), we have $n_e = N_i - Z_d N_d \ll N_i$, then even a slight increase in the dust number density implies that the smaller the difference of $Z_d N_d$ from N_i, the higher the instability threshold. Spectral line width (5.23) of the SBS also increases with the parameter $N_i/n_e > 1$.

In the range of relatively small wavenumbers such that $\max\{l_{ed}^{-1}, \nu_{id}/v_{S,di}\} \ll k \ll \nu_{id} v_{Te}/v_{S,di}^2$, the damping of dust ion acoustic waves is dominated by ion–dust collisions, in which case we obtain the following expression for the SBS instability threshold:

$$\frac{|(\mathbf{k}-\mathbf{k}_0)\times\mathbf{v}_E|_{\text{th}}^2}{4(\mathbf{k}-\mathbf{k}_0)^2 v_{Te}^2} = \frac{\nu_{id}}{k v_{S,di}}\frac{\nu_{ed}}{\omega_0} \sim (Z_d^2 N_d)^2\sqrt{\frac{n_e}{N_i}}. \quad (5.24)$$

From expression (5.24), it is clear that, for a moderate amount of dust in the plasma, and for $n_e \sim N_i$, the larger the grain charge and the higher the dust number density, the higher the instability threshold. Under conditions such that the negative charge in the plasma is carried mainly by the dust grains, and for $Z_d N_d \approx N_i \gg n_e$, the lower the electron density, the lower the threshold for SBS. Under such conditions, the spectral line width of the SBS is determined by the ion–dust collision frequency:

$$\Delta\omega = \nu_{id}\sqrt{\frac{|(\mathbf{k}-\mathbf{k}_0)\times\mathbf{v}_E|^2}{|(\mathbf{k}-\mathbf{k}_0)\times\mathbf{v}_E|_{\text{th}}^2} - 1} \sim Z_d^2 N_d. \quad (5.25)$$

This expression implies that the larger the grain charge and the higher the dust number density, the wider the spectral line of SBS.

For a plasma in which the dust grains carry a moderate charge Z_d consistent with condition (4.7), the dependence of the threshold and spectral line width of the SBS in wavenumber range (4.6) on the dust charge and dust number density is of a fairly peculiar character. This dependence is given by the last term in brackets in expression (5.19) and reflects the influence of nonlocal effects on the damping of dust ion acoustic modes due to electron collisions. If, in this case, the

condition $kl_{ed} < Z_{\text{eff}}^{2/3}$ is satisfied, then the collisionless Landau damping by electrons, which is described by the second term in expression (5.19), is less intense than the collisional damping and the threshold and spectral properties of SBS are governed by dissipation due to collisions of electrons and ions with the dust grains. When the damping of dust ion acoustic waves by ions is unimportant, the spectral properties of SBS and its threshold are governed by the collisional damping by electrons. In this limit, formulas (5.20) and (5.21) for the threshold for SBS and for the width of its spectral line become

$$\frac{|(\mathbf{k}-\mathbf{k}_0)\times\mathbf{v}_E|_{\text{th}}^2}{4(\mathbf{k}-\mathbf{k}_0)^2 v_{Te}^2} = 2.2\frac{v_{S,di}}{v_{Te}}\frac{Z_{\text{eff}}^{2/7}}{(kl_{ed})^{3/7}}\frac{\nu_{ed}}{\omega_0} \sim \sqrt{\frac{N_i}{n_e}}\frac{(Z_d^2 N_d)^{12/7}}{n_e^{2/7}}, \quad (5.26)$$

$$\Delta\omega = 2.2\frac{kv_{S,di}^2}{v_{Te}}\frac{Z_{\text{eff}}^{2/7}}{(kl_{ed})^{3/7}}\sqrt{\frac{|(\mathbf{k}-\mathbf{k}_0)\times\mathbf{v}_E|^2}{|(\mathbf{k}-\mathbf{k}_0)\times\mathbf{v}_E|_{\text{th}}^2}-1} \sim \frac{N_i}{n_e}\frac{(Z_d^2 N_d)^{5/7}}{n_e^{2/7}}. \quad (5.27)$$

Formulas (5.26) and (5.27) demonstrate how the nonlocal effects associated with the damping of dust ion acoustic modes due to electron collisions influence the spectral properties of SBS and its threshold. From these formulas we see that, with increasing dust charge and dust number density, the threshold and spectral line width of the SBS increase to a larger extent than they do in the case described by formulas (5.22) and (5.23), which refer to the collisionless Landau damping of dust ion sound by electrons.

6. STIMULATED BRILLOUIN SCATTERING UNDER CONDITIONS OF THE STRONG DAMPING OF DUST ION ACOUSTIC MODES

Here, we consider the case in which $\omega \sim kv_{Ti} \gg \nu_{id}$ and the dust ion acoustic waves involved in the SBS process are subject to strong dissipation governed by the collisionless Landau damping by ions. As in the case of weak dissipation, which was considered above and in which the set of Eqs. (5.5) and (5.6) was obtained by substituting expression (3.7) into dispersion relation (5.1), we can substitute expression (3.6) for $\delta\varepsilon_i$ into the same dispersion relation to derive an analogous set of equations for determining the frequency detuning Δ and growth rate γ. However, because of the fairly strong dissipation by ions, it is impossible to obtain a simple analytic solution to this set of equations, which thus can be solved only numerically. However, in order to determine the threshold for SBS and the width of its spectral line, it is sufficient to consider

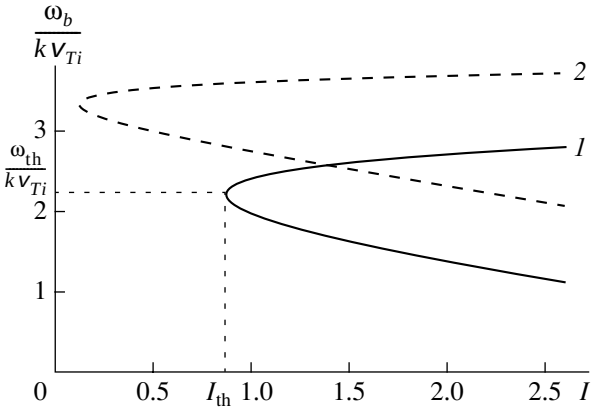

Fig. 1. Boundary frequency ω_b of a dust ion acoustic wave subjected to SBS as a function of the pump field intensity I for ξ = (*1*) 2 and (*2*) 7.

the equation for the boundary of the instability region that follows from this set and has the form (cf. [9])

$$I_b(\omega) = I. \quad (6.1)$$

The function

$$I_b(\omega) = \frac{[\xi + \Phi_1(\omega/kv_{Ti})]^2 + [\Phi_2(\omega/kv_{Ti})]^2}{\xi\Phi_2(\omega/kv_{Ti})}, \quad (6.2)$$

will be termed the boundary intensity. The meaning of this term is that Eq. (6.1) determines the sought spectral line width of the SBS at a given pump wave intensity I. In expression (6.2), we introduce the notation $\Phi_\alpha(z) = F_\alpha(z)/[F_1^2(z) + F_2^2(z)]$, $F_1(z) = [1 - \sqrt{2}\,zF(z/\sqrt{2})]$, and $F_2(z) = \sqrt{\pi/2}\,z\exp(-z^2/2)$ (α = 1, 2). Equation (6.1), which is an analogue of Eq. (5.10), determines the instability boundary and makes it possible to describe the instability region under conditions of strong collisionless dissipation by ions. This is why, in Eq. (6.2), we have omitted an unimportant small term associated with the rate of damping by electrons (see expression (4.5)). From formula (6.2) we see that, under the conditions in question, Eq. (6.1) for the spectral line width of the SBS contains only one dimensionless parameter

$$\xi = N_i T_e/(n_e T_i), \quad (6.3)$$

which determines the dynamic and dissipative properties of the dusty plasmas in which we are interested here. The numerical solution of Eq. (6.1) makes it possible to study the threshold for parametric instability and the spectral width of the instability region. Below, these properties of the instability will be illustrated graphically in the figures.

Curve *1* in Fig. 1 shows the dependence of the normalized (to the quantity kv_{Ti}) frequency ω at the boundary of the SBS instability region on the dimensionless pump field intensity. The frequency was calculated from Eq. (6.1) with ξ = 2. We can see from Fig. 1 that,

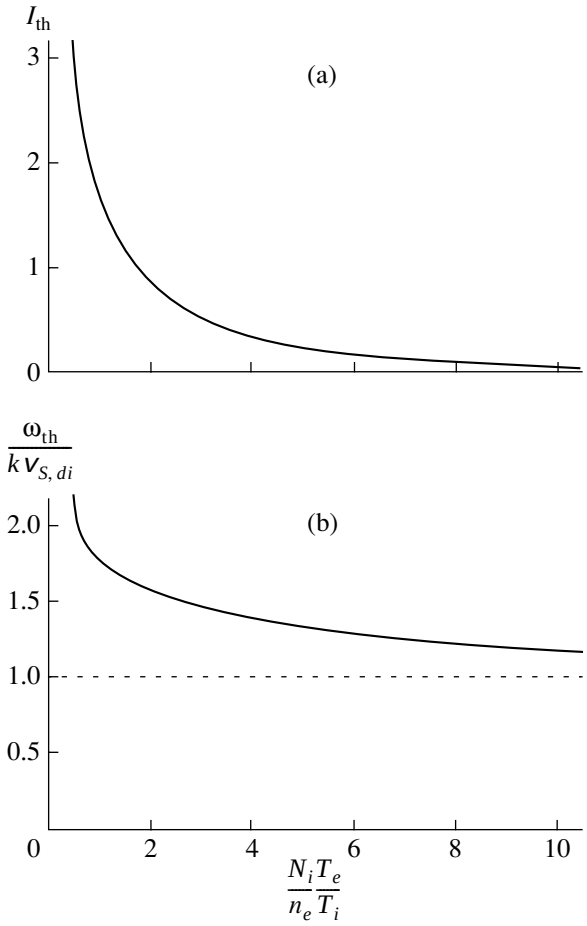

Fig. 2. (a) Threshold intensity I_{th} for the SBS instability and (b) threshold frequency ω_{th} in a dusty plasma as functions of the parameter $\xi \equiv N_i T_e/(n_e T_i)$.

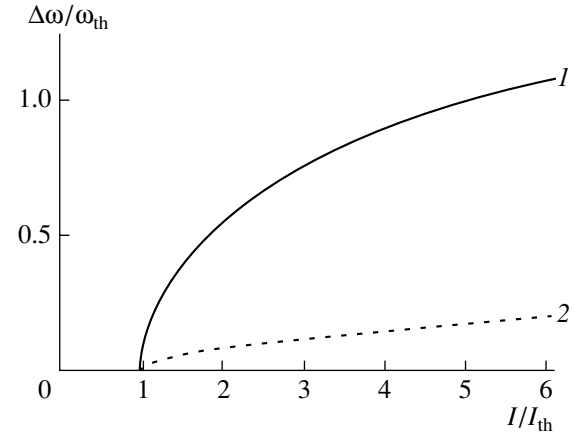

Fig. 3. Relative width of the spectral line of the SBS, $\Delta\omega/\omega_{th}$, as a function of the degree to which the instability threshold is exceeded, I/I_{th}, for a dusty plasma characterized by the same values of the parameter ξ as in Fig. 1.

at the SBS instability threshold, the ratio of the phase velocity of the growing ion acoustic mode to the ion thermal velocity is about $\omega_{th}/kv_{Ti} \cong 2.2$, which corresponds to a fairly strong collisionless Landau damping of the mode in the absence of a pump field. It is precisely the excess of the pump field intensity over the threshold I_{th} that suppresses dissipation and causes the mode to grow, thereby ensuring the amplification of the scattered electromagnetic wave associated with this mode. Curve *1* shows that, when the pump intensity exceeds the threshold by a factor of only two, the width of the instability region $\Delta\omega$ becomes comparable to the threshold frequency ω_{th}, which is a consequence of strong dissipation. Curve *2* in Fig. 1 was calculated for a larger value of the parameter ξ, specifically, $\xi = 7$. We can see that, in this case, the ion acoustic modes involved in the SBS process are characterized by larger values of the ratio of the phase velocity ω/k to the ion thermal velocity v_{Ti} and, accordingly, are subject to the weaker collisionless dissipation by ions (see expression (3.6)). In turn, this weaker dissipation can be suppressed by a lower intensity pump field, so that the SBS instability threshold is lower, which is demonstrated by curve *2* in Fig. 1.

The above properties of the SBS at the threshold are illustrated in Fig. 2. Figure 2a shows the dependence of the threshold intensity I_{th} on the parameter ξ. We see that the SBS instability threshold decreases sharply as the parameter ξ increases, resulting in an increase in the ratio of the phase velocity of the ion acoustic modes involved in the SBS process to the ion thermal velocity, $\omega/(kv_{Ti})$, and, accordingly, in a weakening of the collisionless dissipation by ions. Figure 2b shows the dependence of the ratio of the threshold phase velocity ω_{th}/k of the ion acoustic mode to the phase velocity $v_{S,di}$ (1.4) of the dust ion acoustic waves on the parameter ξ. For $\xi \sim 1$, the threshold phase velocity ω_{th}/k of the ion acoustic mode involved in the SBS process is about two times higher than $v_{S,di}$. As the parameter ξ increases, this difference decreases and, for $\xi \sim 10$, becomes as small as several percent. Hence, for large values of the parameter, $\xi \gg 1$, for which the collisionless dissipation by ions is relatively weak, the threshold frequency of the ion acoustic mode is about $\omega_{th} \approx kv_{S,di}$, which agrees with formula (5.12). In this case, we have $\omega_{th}^2/k^2 v_{Ti}^2 \approx v_{S,di}^2/v_{Ti}^2 \equiv \xi$.

Another manifestation of the weakening of the dissipation by ions with increasing parameter ξ is demonstrated in Fig. 3, which shows how the relative width of the SBS instability region, $\Delta\omega/\omega_{th}$, depends on the degree to which the instability threshold is exceeded, I/I_{th}, for different values of ξ. Curve *1* was calculated for $\xi = 2$, which corresponds to strong collisionless dissipation by ions. From Fig. 3, we can see that, even when the pump field intensity exceeds the threshold by a factor of two, the SBS process involves growing ion acoustic modes with frequencies lying in a wide interval $\Delta\omega$,

whose width is comparable to the threshold frequency ω_{th}. Curve *2*, which was calculated for $\xi = 7$, corresponds to a far narrower frequency interval, which determines the SBS instability region for the same excess of the pump field intensity over the threshold intensity. As the degree I/I_{th} to which the threshold is exceeded increases, the situation does not change qualitatively. Consequently, for $\xi = 2$, the spectral line of SBS is wider than that for $\xi = 7$. Hence, at a fixed value of the ratio I/I_{th}, an increase in the parameter ξ leads to a decrease in the width of the instability region. This regular feature is directly associated with the weakening of dissipation by ions and is fully confirmed by formula (5.15), which was derived in the weak dissipation limit. We thus can conclude that the weaker the dissipation in the plasma, the narrower the spectral line of the scattered radiation, provided that the amount by which the pump field intensity exceeds the threshold is fixed. It should be kept in mind, however, that different threshold intensities I_{th} for the SBS instability correspond to different values of the parameter ξ (see Fig. 2a), so that different pump field intensities I correspond to the different degrees I/I_{th} to which the threshold is exceeded.

7. CONCLUSIONS

We have determined the threshold for the onset of the SBS instability in a dusty plasma and have described the width of the spectral line of SBS under conditions such that this parametric instability is associated with the excitation of dust ion acoustic modes. We have studied these modes in the weak dissipation limit (by taking into account such phenomena as the Cherenkov interaction of electrons and ions with dust ion sound, weakly collisional absorption by electrons, and absorption due to collisions of ions with dust grains) and also in the limit of strong collisionless Landau damping by ions. We have shown that the higher the dust number density and the larger the effective charge of dust grains, the stronger the effect of the dust on the SBS properties.

However, the charge of the dust grains should not be too large. The reason is that a large grain charge (see condition (1.2)) can give rise to a fairly strong Coulomb interaction between charged particles in a dusty plasma. Our analysis was carried out for conditions under which the dusty plasma can be described in the kinetic approximation. This approach is justified for a slightly nonideal plasma, when the energy of Coulomb interaction between charged particles is low in comparison with their kinetic energy and the collective effects are important. Let us assume that the characteristic grain radius a is much less than the mean intergrain distance $d \sim N_d^{-1/3}$. Since the grains carry a large charge, $Z_d \gg 1$, the mean energy of their Coulomb interactions is governed primarily by the interaction among them, whereas the interaction with electrons and ions is weaker. In this case, the condition for the potential energy of Coulomb interaction among the grains to be lower than their thermal energy can be written as $(Z_d e)^2/d \sim (Z_d e)^2 N_d^{1/3} \ll \kappa_B T_d$, where T_d is the dust temperature. Following [2], we rewrite this condition in the form

$$\Gamma_d = \frac{(Z_d e)^2 N_d^{1/3}}{\kappa_B T_d} \ll 1, \qquad (7.1)$$

where we introduce the intergrain interaction parameter Γ_d.

Because of the large dust charge (see condition (7.1)), the mean energy of Coulomb interaction of electrons and ions with dust grains can exceed the mean energy of Coulomb interaction between the electrons and the ions. Under conditions (1.1) and (1.2), which imply that the plasma is electrically neutral and the grain charge is large, the inequality $N_d \ll N_i$ is satisfied. In this case, the mean distance from an ion to the nearest grain is about $\sim 0.5d$ and the absolute energy of Coulomb interaction between ions and grains is about $Z_d e^2/(0.5d) \sim 2Z_d e^2 N_d^{1/3}$, the mean interaction energy of two ions being $e^2 N_i^{1/3}$. For a dusty plasma satisfying the condition $N_i/Z_d^3 < N_d \le N_i/Z_d$, which indicates that the dust number density is not too low and the dust charge is large ($Z_d \gg 1$), we find that the mean energy of the ion–dust Coulomb interaction exceeds that of the ion–ion Coulomb interaction. As a result, the condition for the energy of Coulomb interaction among the ions to be weaker than their mean kinetic energy can be written as $2Z_d e^2 N_d^{1/3} \ll \kappa_B T_i$ or

$$\frac{T_d}{Z_d T_i}\Gamma_d \ll 1. \qquad (7.2)$$

Replacing the ion temperature T_i with the electron temperature T_e yields an analogous condition for the electrons. The usual situation in dusty plasma is such that $T_e \ge T_i$; therefore, the condition that the energy of Coulomb interaction among the ions is weaker than their mean kinetic energy is more stringent than the corresponding condition for the electrons. Let us compare inequalities (7.1) and (7.2). For dusty plasmas, the inequality $T_d \le T_i$ is usually satisfied. Consequently, because of the large grain charge (see condition (1.2)), inequality (7.2) is weaker than inequality (7.1).

Inequality (7.1), which contains only the absolute dust temperature, density, and change, can also be written as

$$\Gamma_d = 1.4 \times 10^{-7} Z_d^2 \frac{(N_d\ [\mathrm{cm}^{-3}])^{1/3}}{T_d\ [\mathrm{eV}]} \ll 1. \qquad (7.3)$$

Condition (7.3) refers to slightly nonideal plasmas in which the density of energetic dust grains is sufficiently

low. This condition is very sensitive to the charge Z_d of the dust grains: the larger the dust charge Z_d, the easier the condition is to satisfy. On the other hand, according to condition (1.2), the charge of a grain should be much larger than unity. Let us show that this can be the case.

An example of a dusty plasma that contains negatively charged dust grains and is slightly nonideal, i.e., satisfies condition (7.3), is a plasma at altitudes of about 80 km in the Earth's upper atmosphere (see, e.g., [4]). For such a plasma, we have $N_d \sim 10$ cm^{-3}, $N_i \sim 10^3$ cm^{-3}, and the particle temperature is about 150 K, so that condition (7.3), which indicates that the plasma is slightly nonideal, and condition (1.2) are satisfied for grains whose charges lie in the range $1 \ll Z_d \ll 200$. Under the assumption that the grains are charged primarily by absorbing the electron and ion fluxes onto their surfaces, the order-of-magnitude estimate of the maximum possible grain charge is provided by the formula [2]

$$Z_d \sim T_e a/e^2 \approx 700 T_e \text{ [eV] } a \text{ [}\mu\text{]}. \quad (7.4)$$

For a grain with a characteristic radius of $a \sim 5$ μm, formula (7.4) gives $Z_d \sim 45$, which agrees with condition (7.3) for the plasma to be slightly nonideal. Hence, under the above conditions in the Earth's ionosphere, the kinetic description of a dusty plasma is justified.

In conclusion, note that we have considered the SBS process under conditions in which the change in the dust charge in the field of a dust ion acoustic wave can be ignored. This approach is justified in situations when SBS develops on time scales shorter than the characteristic time scale of the dust charge variation and the dust charge variation itself has an insignificant effect on the spectral properties of the SBS process and on its properties at the instability threshold. According to formulas (5.20) and (5.21), the threshold for SBS and the width of its spectral line are governed by the dissipative properties of the dusty plasma, namely, by the damping rate of the dust ion acoustic waves involved in the scattering process. In Appendix 1, the expression for the damping rate of the dust ion sound is derived with allowance for dust charging by electron and ion fluxes (see formulas (A1.15)–(A1.17)) and the conditions are determined under which the effect of this charging on the dissipation of dust ion acoustic waves can be ignored. Inequality (A1.19) implies that, in a plasma with an equilibrium dust charge, the grain charge variations have a weak effect on the damping of dust ion sound when the electron temperature is much higher than the ion temperature or when the dust charge density is lower than the electron charge density. In determining the SBS threshold, the grain charge variations in a plasma with a strongly nonequilibrium dust charge can be ignored when the grains are small enough for the characteristic frequencies of variation of their charge to be low (see formulas (A1.8)–(A1.10)) and the variation in Z_d to make a small contribution to the damping rate of the dust ion acoustic waves (see formula (A1.16)).

ACKNOWLEDGMENTS

This work was supported in part by the Russian Foundation for Basic Research (project no. 02-02-16047), the Russian Federal Program for the Development of the Priority Directions in Science and Technology in 2002–2006 (state contract no. 40.165), and the Russian Federal Program for State Support of Leading Scientific Schools (project no. NSh-1385.2003.2).

APPENDIX 1

Contribution of the Grain Charge Variation to the Damping Rate of the Dust Ion Sound

In a dusty plasma in which the grains are charged by electron and ion fluxes onto their surfaces, each grain acquires a negative charge eZ_d in accordance with the equation (see, e.g., [3])

$$\frac{\partial Z_d}{\partial t} = \sqrt{8\pi} a^2 \left[n_e v_{Te} e^{-\frac{Z_d e^2}{a T_e}} - N_i v_{Ti} \left(1 + \frac{Z_d e^2}{a T_i} \right) \right]. \quad (A1.1)$$

In this case, electroneutrality condition (1.1) implies that $n_e < N_i$. For an equilibrium dusty plasma, Eq. (A1.1) yields the following equation for the equilibrium dust charge:

$$n_e v_{Te} e^{-\frac{Z_d e^2}{a T_e}} = N_i v_{Ti} \left(1 + \frac{Z_d e^2}{a T_i} \right). \quad (A1.2)$$

This equation has the solution

$$Z_d^{(eq)} = \frac{a T_e}{e^2} g\left(\frac{n_e v_{Te}}{N_i v_{Ti}}, \frac{T_e}{T_i} \right). \quad (A1.3)$$

Figure 4 shows how the function g depends on the parameter $n_e v_{Te}/(N_i v_{Ti})$ for an isothermal plasma, in which $T_e = T_i$ (curve *1*), and for a plasma with hot electrons such that $T_e = 10 T_i$ (curve *2*). From Fig. 4, we can see that the solution to Eq. (A1.2) that determines the equilibrium negative dust charge exists only in the range $n_e/N_i > v_{Ti}/v_{Te}$. Figure 4 also demonstrates that, over a fairly broad range of values of the parameter $n_e v_{Te}/(N_i v_{Ti})$, the function g takes on values on the order of unity, so that the equilibrium grain charge is given by the approximate expression $Z_d \sim a T_e/e^2$ (cf. formula (7.4)).

Let us calculate the contribution of the variation in the grain charge to the damping rate of the dust ion acoustic waves. To do this, we consider a small perturbation of the electric potential in a dusty plasma and represent it in the form

$$\delta\varphi \exp(i\mathbf{kr} - \omega t). \quad (A1.4)$$

Poisson's equation yields the following equation for the perturbation amplitude $\delta\omega$:

$$k^2\delta\varepsilon(\omega, \mathbf{k})\delta\varphi = 4\pi(\delta\rho_e + \delta\rho_i + \delta\rho_d), \qquad \text{(A1.5)}$$

where the longitudinal dielectric function $\delta\varepsilon(\omega, \mathbf{k})$ of a dusty plasma takes into account the grain charge variation, $\delta\rho_e = e\delta n_e$ and $\delta\rho_i = -e\delta N_i$ are the perturbed charge densities of the electrons and ions, and $\delta\rho_d = eN_d\delta Z_d$ is the perturbed dust charge density. The last expression is written under the assumption that the grains are infinitely heavy and immobile, which is justified for the dust ion acoustic waves under consideration here (those whose phase velocities are high enough to satisfy condition (4.2)).

We describe the perturbations of the electron and ion densities and the perturbed dust charge density by the same spatiotemporal dependence as that used for the perturbing electric potential, namely, by formula (A1.4). We consider perturbations (A1.4) that are sufficiently fast compared to the dust charge variation, i.e., those that satisfy the inequality

$$\omega \gg \left|\frac{1}{Z_d}\frac{\partial Z_d}{\partial t}\right|. \qquad \text{(A1.6)}$$

In order to determine the conditions under which the dust charge variation has an insignificant impact on the properties of the dust ion sound, we restrict ourselves to the simplest approximation in which the temperatures of the plasma components are assumed to be unperturbed. In this case, Eq. (A1.1) leads to the following expression for the perturbed grain charge:

$$\delta Z_d = \frac{1}{\nu_Q - i\omega}\left(\nu_{Qe}\frac{\delta n_e}{n_e} - \nu_{Qi}\frac{\delta N_i}{N_i}\right), \qquad \text{(A1.7)}$$

where we introduce the effective frequencies

$$\nu_Q = \sqrt{8\pi}ae^2\left(\frac{n_e v_{Te}}{T_e}e^{-\frac{Z_d e^2}{aT_e}} + \frac{N_i v_{Ti}}{T_i}\right), \qquad \text{(A1.8)}$$

$$\nu_{Qe} = \sqrt{8\pi}a^2 n_e v_{Te}e^{-\frac{Z_d e^2}{aT_e}}, \qquad \text{(A1.9)}$$

$$\nu_{Qi} = \sqrt{8\pi}a^2 N_i v_{Ti}\left(1 + \frac{Z_d e^2}{aT_i}\right). \qquad \text{(A1.10)}$$

The frequency ν_Q is the dust charging frequency and the frequencies ν_{Qe} and ν_{Qi} characterize the grain charge variations caused by variations in the electron and ion densities in the plasma. Substituting expression (A1.7) into Eq. (A1.5) yields

$$k^2\delta\varepsilon(\omega, k)\delta\varphi = 4\pi e\left[\delta n_e - \delta N_i + \frac{N_d}{\nu_Q - i\omega}\left(\nu_{Qe}\frac{\delta n_e}{n_e} - \nu_{Qi}\frac{\delta N_i}{N_i}\right)\right]. \qquad \text{(A1.11)}$$

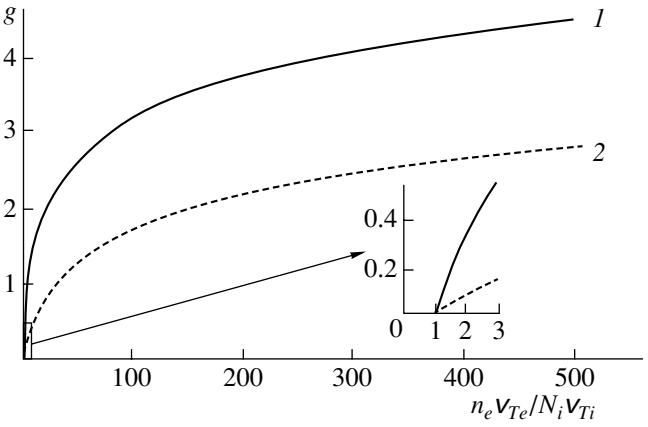

Fig. 4. Function g, which determines the equilibrium charge of the grains, vs. parameter $n_e v_{Te}/(N_i v_{Ti})$ for a dusty plasma with $T_e = (1)\ T_i$ and $(2)\ 10T_i$.

With the electron and ion partial contributions, $\delta\varepsilon_e = 4\pi e\delta n_e/(k^2\delta\varphi)$ and $\delta\varepsilon_i = -4\pi e\delta N_i/(k^2\delta\varphi)$, expression (A1.11) for the dielectric function of a dusty plasma becomes

$$\delta\varepsilon(\omega, \mathbf{k}) = \delta\varepsilon_e(\omega, \mathbf{k})\left(1 + \frac{N_d}{n_e}\frac{\nu_{Qe}}{\nu_Q - i\omega}\right) + \delta\varepsilon_i(\omega, \mathbf{k})\left(1 + \frac{N_d}{N_i}\frac{\nu_{Qi}}{\nu_Q - i\omega}\right), \qquad \text{(A1.12)}$$

where the function $\delta\varepsilon_e(\omega, \mathbf{k})$ is given by formula (2.3) and the function $\delta\varepsilon_i(\omega, \mathbf{k})$ is given by formula (3.1) or (3.6).

We assume that the following inequalities are satisfied:

$$\omega \gg \max\left\{\nu_Q, \frac{N_d}{n_e}\nu_{Qe}, \frac{N_d}{N_i}\nu_{Qi}\right\}. \qquad \text{(A1.13)}$$

Keeping only the lowest order terms in the small parameters determined by inequalities (A1.13), we reduce expression (A1.12) to

$$\delta\varepsilon = \delta\varepsilon_e\left(1 + i\frac{N_d}{n_e}\frac{\nu_{Qe}}{\omega}\right) + \delta\varepsilon_i\left(1 + i\frac{N_d}{N_i}\frac{\nu_{Qi}}{\omega}\right)$$

or

$$\delta\varepsilon \simeq \delta\varepsilon_e' + \delta\varepsilon_i' + i\left[\delta\varepsilon_e'' + \delta\varepsilon_i'' + \frac{1}{\omega}\left(\delta\varepsilon_e'\frac{N_d}{n_e}\nu_{Qe} + \delta\varepsilon_i'\frac{N_d}{N_i}\nu_{Qi}\right)\right]. \qquad \text{(A1.14)}$$

For simplicity, we consider the case of a weak damping by electrons and ions such that the imaginary parts $\delta\varepsilon_e''$ and $\delta\varepsilon_i''$ are small in comparison to the real parts. The dispersion relation for the dust ion sound has

the form $\delta\varepsilon(\omega, \mathbf{k}) = 0$. The real component of this relation is dispersion relation (1.3) for dust ion acoustic waves having velocity (1.4). As for the imaginary component, it makes it possible to determine the damping rate of the dust ion acoustic waves with allowance for variations in the dust grain charge:

$$\gamma_S = \left(\delta\varepsilon''/\frac{\partial\delta\varepsilon'}{\partial\omega}\right)\Bigg|_{\omega=\omega_S} = \gamma_e + \gamma_i + \gamma_Q. \qquad \text{(A1.15)}$$

Here, the first two terms on the right-hand side correspond to electron contribution (4.5) and ion contribution (4.9) or (4.10) to the damping rate of the dust ion sound; these contributions were considered in Section 4. The last (third) term accounts for the contribution of the dust charge variation caused by electron and ion fluxes to the damping rate of the dust ion acoustic waves. This term has the form

$$\gamma_Q = \frac{1}{2}\left(\frac{N_d}{n_e}\nu_{Qe} - \frac{N_d}{N_i}\nu_{Qi}\right). \qquad \text{(A1.16)}$$

It is obvious that, under the condition $|\gamma_Q| \ll \gamma_e + \gamma_i$, this last contribution can be ignored.

Let us consider this condition for a dusty plasma in which the equilibrium grain charge is described by Eq. (A1.2). In this case, condition (A1.6) holds automatically and we have $\nu_{Qe} = \nu_{Qi}$, so that expression (A1.16) for the relevant contribution to the damping rate becomes

$$\gamma_Q = \frac{1}{2}\frac{Z_d^{(eq)}N_d^2}{n_e N_i}\nu_{Qi}. \qquad \text{(A1.17)}$$

When collisional damping by the ions, which governs damping rate (4.9), predominates over that by the electrons, the condition that the damping rate γ_Q be low takes the form $2|\gamma_Q| \ll \nu_{id}$ or

$$\frac{N_d}{n_e}\left(\frac{aT_i}{e^2}\right)^2\left(1 + \frac{Z_d^{(eq)}e^2}{aT_i}\right) \ll \frac{2}{3}Z_d^{(eq)}\Lambda. \qquad \text{(A1.18)}$$

Taking into account formula (A1.3) for the equilibrium dust charge and the relationship $g \sim 1$, which is valid for moderate electron densities, we rewrite inequality (A1.18) as

$$\frac{T_i}{T_e}\left(1 + \frac{T_i}{T_e}\right)\frac{Z_d^{(eq)}N_d}{n_e} \ll \frac{2}{3}\Lambda. \qquad \text{(A1.19)}$$

Hence, in a dusty plasma with comparable charge densities of the electrons and dust grains and with nearly equilibrium dust charge, the dust charge variation has an insignificant effect on the damping of dust ion sound when the electron temperature substantially exceeds the ion temperature, $T_e \gg T_i$. Note that the lower the dust charge density, the easier the condition (A1.19) is to satisfy. It should be stressed that, under the conditions of weak damping of the dust ion acoustic waves ($\gamma_S \ll \omega_S$) and for $|\gamma_Q| \ll \gamma_e + \gamma_i$, inequality (A1.13) is comparatively easy to satisfy.

Inequalities (A1.6) and (A1.13), as well as condition (A1.16), which indicates that the damping rate γ_Q is lower than $\gamma_e + \gamma_i$, are also comparatively easy to satisfy for a dusty plasma with a slowly changing dust charge. The reason is that the smaller the grains, the lower the characteristic frequencies ν_{Qi}, ν_{Qe}, and γ_Q, which determine the dust charge variation and the contribution γ_0 to the damping rate. Consequently, for a plasma with sufficiently small grains, there is no need to take into account the dust charge variations when discussing the dissipative properties of the dust ion sound.

APPENDIX 2

In conclusion, we will say a few words about papers [11, 14], which were brought to our attention by the reviewer. Unlike us, Tsytovich *et al.* [14] studied an incompletely ionized plasma and, consequently, they took into account the important effect of collisions with neutrals. In this connection, the authors of [14] considered the problem of dust acoustic waves in an essentially collisional dusty plasma merely as the simplest example of problems in which oscillations are investigated using a Maxwellian distribution. Our analysis also involves a Maxwellian distribution function. Note, however, that the content of [14] is not concerned directly with the issues under discussion here because, in [14], a study was made of dust acoustic waves, whose frequency is much lower than the frequency of dust ion acoustic waves and which thus cannot manifest themselves in the range of frequency shifts of SBS that was considered above.

Note also that, in [14], nothing was said about the negligible role of Landau damping for dust ion acoustic waves (not to be confused with dust acoustic waves, which are the subject of [14]).

In [11], Tsytovich and Watanabe studied the problem of how to take into account the evolution of the dust charge. Accounting for the evolving grain charge leads to a new spectrum of dust ion acoustic waves (see formula (19) from [11]). However, over a fairly broad range of wavenumbers of dust ion acoustic waves in long-wavelength limit (4.1),

$$\frac{1}{\sqrt{2\pi}}\frac{a}{r_{Di}}\max\left\{1, \frac{Z_d N_d}{n_e}\right\} \ll kr_{De} \ll 1, \qquad \text{(A2.1)}$$

the new spectral details revealed in [11] do not manifest themselves and the spectrum of dust ion sound that was obtained in our study (see formulas (1.3), (1.4)) is valid. This fairly broad range of wavenumbers k is restricted

by the left- and right-hand inequalities (A2.1) under the condition

$$\frac{1}{\sqrt{2\pi}}\frac{a}{r_{Di}} = 1.7\times 10^{-4}\left(\frac{a\ [\mu\mathrm{m}]}{0.1}\right)\sqrt{\frac{N_i\ [\mathrm{cm}^{-3}]/10^8}{T_i\ [\mathrm{eV}]/0.1}} \ll \frac{n_e}{N_i}, \quad \text{(A2.2)}$$

Hence, our approach applies to a dusty plasma in which the dust grains are quite small and the electron density is not too low. We are grateful to the reviewer, whose comments allowed us to derive conditions (A2.1) and (A2.2). Note that, in [11], Landau damping was not considered. As for the collisional damping, the right-hand side of formula (4.9) obtained in our study coincides with the main term on the right-hand side of formula (22) obtained in [11].

Finally, we should say a few words about aperiodic instabilities revealed in [11]. According to inequality (23) from [11], the characteristic time scale on which such instabilities develop is larger than the reciprocal of the ion–dust collision frequency. On the other hand, this collision frequency is much lower than the frequency of the dust ion acoustic waves in which we are interested here (see formula (3.2)). This naturally justifies the quasi-steady approach that was used above to treat SBS and in which the changes that occur in the plasma during one period of the dust ion acoustic waves and that may give rise to the aperiodic instability considered in [11] can be ignored. We emphasize that, according to inequality (23) in [11] and to formulas (4.4), (4.9), and (5.16) derived in our study, the growth rate of the SBS instability exceeds that of the aperiodic instability revealed in [11]. This indicates that the time scale of the parametric SBS instability is too short for the aperiodic instability to develop.

REFERENCES

1. M. Rosenberg, Astrophys. Space Sci. **277** (6), 125 (2001).
2. A. P. Nefedov, O. F. Petrov, and V. E. Fortov, Usp. Fiz. Nauk **167**, 1215 (1997) [Phys. Usp. **40**, 1163 (1997)].
3. P. K. Shukla, Phys. Plasmas **8**, 1791 (2001).
4. D. A. Mendis and M. Rosenberg, IEEE Trans. Plasma Sci. **20**, 929 (1994).
5. P. K. Shukla and V. P. Silin, Phys. Scr. **45**, 508 (1992).
6. V. P. Silin, Usp. Fiz. Nauk **172**, 1021 (2002).
7. K. Yu. Vagin, K. N. Ovchinnikov, and V. P. Silin, Kratk. Soobshch. Fiz., No. 5, 18 (2002).
8. K. Yu. Vagin, K. N. Ovchinnikov, and V. P. Silin, Kratk. Soobshch. Fiz., No. 5, 32 (2002).
9. K. Yu. Vagin, K. N. Ovchinnikov, V. P. Silin, and S. A. Uryupin, Kvantovaya Élektron. (Moscow) **32**, 629 (2002).
10. K. Yu. Vagin, submitted to Fiz. Plazmy.
11. V. N. Tsytovich and K. Watanabe, Contrib. Plasma Phys. **43**, 51 (2003).
12. L. M. Gorbunov, Zh. Éksp. Teor. Fiz. **55**, 2298 (1968) [Sov. Phys. JETP **28**, 1220 (1968)].
13. V. P. Silin, *Parametric Action of High-Power Radiation on Plasmas* (Nauka, Moscow, 1973), p. 147.
14. V. N. Tsytovich, U. de Angelis, and R. Bingham, Phys. Rev. Lett. **87**, 185003 (2001).

Translated by O.E. Khadin

Plasma Physics Reports, Vol. 30, No. 8, 2004, pp. 652–661. Translated from Fizika Plazmy, Vol. 30, No. 8, 2004, pp. 704–712.

DUSTY PLASMA

Transport Properties of Nonideal Systems with Isotropic Pair Interactions between Particles

O. S. Vaulina

Institute for High Energy Densities, Associated Institute for High Temperatures, Russian Academy of Sciences, Izhorskaya ul. 13/19, Moscow, 125412 Russia

Received October 2, 2003; in final form, December 11, 2003

Abstract—Results are presented from numerical investigations of the mass transfer and pair correlation in systems of interacting grains for different types of isotropic interaction potentials. The parameters are determined that govern the transport properties of nonideal dissipative systems with a large variety of model potentials. An analytic approximation for the dust grain diffusion coefficient in strongly nonideal systems is obtained. © *2004 MAIK "Nauka/Interperiodica".*

1. INTRODUCTION

Problems associated with transport processes in dissipative systems of interacting particles are of considerable interest for different fields of science and technology (hydrodynamics, plasma physics, molecular biophysics, medical engineering, physics and chemistry of polymers, etc.) [1–8]. A good experimental model for studying such transport processes is provided by a laboratory dusty plasma—a weakly ionized gas with micron-size dust grains [8–13]. In a dusty plasma, such grains can acquire a considerable electric charge and can form liquidlike and solidlike quasi-steady dust structures.

Investigations of the properties of nonideal dusty plasmas can play an important role in the development of new phenomenological models for nonideal liquidlike systems. Such investigations take on special importance because, in contrast to the theory of gases, the theory of liquids deals with strong interactions between particles and thus does not contain a small parameter that can provide an analytic description of the states of a liquid and of its thermodynamic properties [1–7]. Another difficulty in studying nonideal media is associated with the fact that, in most cases, the actual potentials of interaction between particles in physical systems are unknown. Therefore, the prevailing view is that this difficulty cannot be resolved in terms of molecular theory alone. As a result, a new model approach, called the concept of effective semiempirical model potentials, has been developed and has become widely accepted. In this approach, the shape of model potentials is almost always specified in advance and the parameters of a chosen model function are reconstructed from the experimentally measured parameters of the medium under investigation [14, 15].

In contrast to the particles of actual liquids and gases, micron-size dust grains in plasmas are large enough to be recorded by a video camera. This greatly simplifies the use of nonintrusive methods for diagnosing them and offers the possibility of studying the physical properties of nonideal systems at the kinetic level. The common practice is to describe the interaction between grains in a dusty plasma by a Yukawa-type screened Coulomb potential,

$$U = a_0 \exp(-r/\lambda)/r. \quad (1)$$

Here, r is the distance; λ is the screening length; and a_0 is a parameter equal to $(eZ_p)^2$ for two identical grains of charge eZ_p, where e is the charge of an electron. Potential (1) agrees well with both the data from measurements of the forces of interaction between two dust grains [14] and the results of numerical calculations of the structure of the screening cloud [15], but only for short distances from a grain, $r < 5\lambda_D$, where λ_D is the plasma Debye radius. The longer the distance r from the grain, the weaker the screening effect; at distances $r \gg \lambda_D$, the potential U behaves asymptotically as a power function, $U \propto r^{-2}$ [16] or $U \propto r^{-3}$ [17]. The cited papers [14–17] present the results of investigations of solitary grains in a plasma. At present, there is no final explanation of how the shape of the intergrain interaction potential is affected by the presence of other particles in a dust cloud, the gas ionization processes, the collisions of electrons and ions with the neutral particles of the surrounding gas, and a host of other factors. Hence, the actual potentials of interaction between dust grains in a plasma are unknown (as is the case in many physical problems in which it is necessary to take into account the interparticle interaction forces), so that an important task for the physics of nonideal dusty plasmas and for other branches of natural science is to determine the parameters that govern the state of a system of interacting particles. As an example, in [18, 19], the two dimensionless parameters were found that are responsible for the mass transfer processes in Yukawa dissipative systems (with $\kappa = r_p/\lambda < 6$–7) and for their

1063-780X/04/3008-0652$26.00 © 2004 MAIK "Nauka/Interperiodica"

phase state. These are the effective coupling parameter $\Gamma^* = \Gamma\{(1 + \kappa + \kappa^2/2)\exp(-\kappa)\}^{1/2}$ and the scaling parameter $\xi = \nu_{fr}^{-1} eZ_p\{(1 + \kappa + \kappa^2/2)\exp(-\kappa)n_p/\pi m_p\}^{1/2}$. Here, n_p is the particle density, $\Gamma = (Z_p e)^2/(Tr_p)$ is the Coulomb coupling parameter, T is the particle temperature, $r_p = n_p^{-1/3}$ is the mean interparticle distance, and ν_{fr} is the coefficient of friction of grains against neutrals of the surrounding gas. In [20–22], the numerical model just described was checked against the conditions of laboratory experiments with dusty plasmas in different types of gas discharges. Experimental investigations showed that the dynamics of dust grains in the plasma under analysis can be described in terms of the two main parameters, Γ^* and ξ; however, determining the parameters of the interparticle interaction potential requires additional information about its shape.

Hence, it was pointed out that the mass transfer processes and the spatial correlation between the grains in Yukawa systems ($\kappa < 6$–7) are determined by the ratio of the second derivative U'' of the pair interaction potential $U(r)$ at the mean intergrain distance r_p to the particle temperature T. In the systems under study, the crystallization and melting processes ($\Gamma^* \sim 102$–106) and the formation of regular dust clusters ($\Gamma^* \sim 22$–25) were observed to occur at fixed values of the effective parameter Γ^* [18, 19]. It is logical to suppose that, under certain conditions, systems with a wider variety of pair interaction potentials will also possess these properties. In order to confirm this supposition, we have analyzed the mass transfer processes, the shape of the pair correlation functions, and the conditions for phase transitions in systems with different types of radial repulsive potentials, described by the different superpositions of power functions and exponentials that are used to model repulsion in the kinetics of interacting particles [3–7]:

$$U = U_c a_1 (r_p/r)^n, \tag{2}$$

$$U = U_c[a_1 \exp(-\kappa_1 r/r_p) + a_2 \exp(-\kappa_2 r/r_p)], \tag{3}$$

$$U = U_c[a_1 \exp(-\kappa_1 r/r_p) + a_2 (r_p/r)^n]. \tag{4}$$

Here, a_1, a_2, κ_1, κ_2, and n are the parameters that were varied in simulations and $U_c = a_0/r$ is the Coulomb potential. Along with potential (1), of particular interest for dusty plasma physics are model potentials (3) and (4) (the latter at $n = 1$ and $n = 2$), which makes it possible to take into account weakening of the screening effect with increasing interparticle distance [14–17]. Analogous models are also applied to account for repulsion between atoms in covalent metals or in polymer physics [3–7].

2. PARAMETERS OF THE NUMERICAL PROBLEM

A correct simulation of grain transport in a dusty plasma requires the use of the molecular dynamics method, which is based on solving a set of ordinary differential equations involving the Langevin force F_{br} that takes into account random impacts of the surrounding gas molecules and other stochastic processes causing the dust grains to relax to an equilibrium (steady-state) kinetic temperature T, characterizing the energy of their stochastic (thermal) motion [7, 23, 24]. Microscopic processes occurring in uniform extended clouds of interacting dust grains are usually modeled by using periodic boundary conditions and by taking into account not only the random forces F_{br} that are responsible for dust thermal motion but also the pair interaction forces F_{int} [18–24]:

$$m_p \frac{d^2\mathbf{l}_k}{dt^2} = \sum_j F_{int}(l)|_{\mathbf{l}=|\mathbf{l}_k-\mathbf{l}_j|} \frac{\mathbf{l}_k - \mathbf{l}_j}{|\mathbf{l}_k - \mathbf{l}_j|} - m_p \nu_{fr} \frac{d\mathbf{l}_k}{dt} + \mathbf{F}_{br}, \tag{5}$$

where $\mathbf{l} = |\mathbf{l}_k - \mathbf{l}_j|$ is the interparticle distance, m_p is the mass of a particle, ν_{fr} is the friction coefficient of dust grains [25, 26], and $F_{int}(l) = -\partial U/\partial l$ is the pair interaction–driven force. The computations were carried out for Yukawa potentials with $\kappa = 2.4$ and 4.8. The screening length λ was chosen to provide a correct simulation of the dynamics of the systems under investigation (the cell size of the numerical grid being $R \gg \lambda$) [27]. Additional simulations were carried out for different combinations of power functions and exponentials given by formulas (2)–(4).

The pair correlations in systems of particles interacting by means of different types of isotropic repulsive potentials (1)–(4) were analyzed by solving three-dimensional equations of motion (5) for different values of the effective parameters that were introduced by analogy with the parameters obtained for Yukawa systems, specifically, the effective coupling parameter

$$\Gamma^* = Q_p^{*2}/Tr_p, \tag{6}$$

and the scaling parameter

$$\xi = \omega^*/\nu_{fr}, \tag{7}$$

where the characteristic frequency of collisions among the grains is given by relationship

$$\omega^* = Q_p^*(n_p/\pi m_p)^{1/2}, \tag{8}$$

and Q_p^* is the effective grain charge defined by

$$Q_p^* = [U''/2n_p]^{1/2}. \tag{9}$$

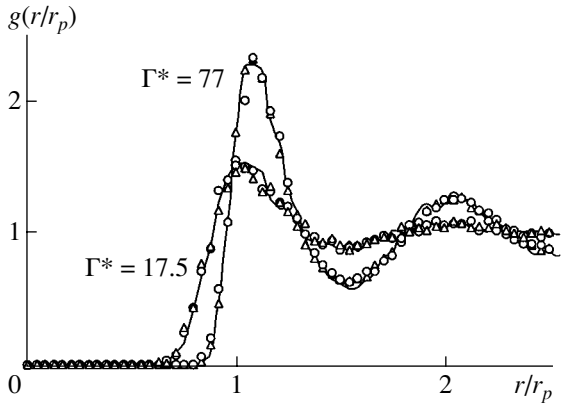

Fig. 1. Illustration of pair correlation functions $g(r/r_p)$ for different model potentials and for different values of the parameters ξ and Γ*. For Γ* = 77, the solid curve refers to ξ = 0.14 and $U/U_c = \exp(-4.8r/r_p)$, the triangles refer to ξ = 0.14 and $U/U_c = 0.1\exp(-2.4r/r_p) + \exp(-4.8r/r_p)$, and the circles refer to ξ = 1.22 and $U/U_c = \exp(-4.8r/r_p) + 0.05r_p/r$. For Γ* = 17.5, the solid curve refers to ξ = 1.22 and $U/U_c = \exp(-2.4r/r_p)$, the triangles refer to ξ = 1.22 and $U/U_c = 0.1\exp(-2.4r/r_p) + \exp(-4.8r/r_p)$, and the circles refer to ξ = 0.14 and $U/U_c = 0.05(r_p/r)^3$.

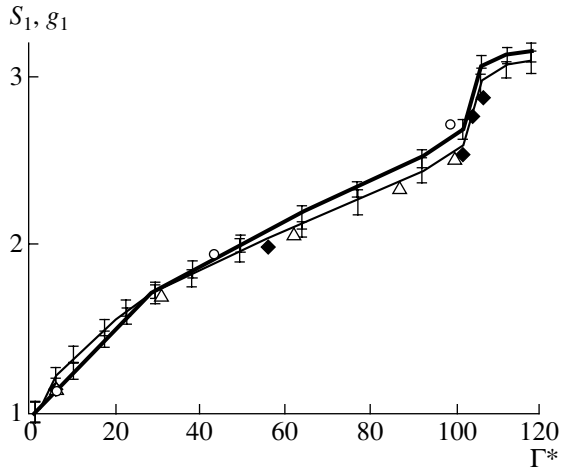

Fig. 2. Dependence of the first maxima of the structure factor S_1 (heavy curve) and of the pair correlation function g_1 (light curve) on Γ*. The closed diamonds are for the values of g_1 in the Yukawa dispersive model ($\nu_{fr} = 0$) [28], the triangles are for the values of g_1 in the OCP model [29], and the circles are for the values of S_1 in the OCP model [29]. The vertical bars show the absolute deviations for different values of the scaling parameter in the range ξ = 0.04–3.6 and for different potentials satisfying condition (10).

Note that the use of notation (9) makes it possible to analyze each of potentials (1)–(4) in terms of the effective parameters (Γ*, ξ, ω*). For Yukawa potential (1), the effective charge can be written as $Q_p^* = eZ_p(1 + \kappa + \kappa^2/2)^{1/2}\exp(-\kappa/2)$.

Simulations of the pair interactions were carried out for 125 particles in the central numerical cell, the total number of particles being up to about 3000. The interparticle interaction potential was cut off at the distance $L_{cut} = 4r_p$. The extent to which the calculated results are independent of the number of particles and on the cutoff distance was checked in additional test simulations that were carried out for systems with Γ* = 1.5, 17.5, 25, 49, and 92, for 512 particles in the central cell and for $L_{cut} = 7r_p$. The final results of these simulations were found to differ by no more than ±(1–3)%, which does not exceed the computational errors. The computation procedure was described in detail in [18, 22]. The scaling parameter was varied in the range between ξ ≈ 0.04 and ξ ≈ 3.6, which is typical of the conditions of experiments with gas discharge plasmas. The value of the effective parameter Γ* was varied from 1 to 110.

Numerical simulations showed that, in the systems under study, the mass transfer processes, the formation of ordered structures, and the phase states are described completely by the effective parameter Γ*, provided that the long-range potentials obey the empirical condition

$$2\pi|U'(r_p)| > |U''(r_p)|r_p, \qquad (10)$$

which, in a first (linear) approximation, is the condition that the pair interaction forces at the mean interparticle distance are stronger than the forces driven by collisions between the dust grains.

3. FORMATION OF ORDERED STRUCTURES

The formation of ordered structures in the systems under study was analyzed with the help of the pair correlation function $g(r)$ and the structure factor $S(q)$. The shapes of the pair correlation functions $g(r)$ calculated for different model potentials obeying empirical condition (10), for two different values of the parameter Γ*, and for different values of ξ are compared in Fig. 1. The dependence of the first maxima (g_1, S_1) of the correlation functions $g(r)$ and $S(q)$ and of the positions of the maxima ($r = d_{g1}$, $q = d_{S1}$) on the parameter Γ* is illustrated in Figs. 2 and 3, in which the vertical bars show the absolute deviations of the plotted quantities for different values of the scaling parameter in the range ξ = 0.04–3.6 and for different potentials given by formulas (1)–(4). In order to compare the results from the calculation of the pair correlation function of the particles in the dissipative systems under examination ($\nu_{fr} \neq 0$) with the solution to the reversible equations of motion for Yukawa dispersive systems ($\nu_{fr} = 0, \xi \longrightarrow \infty$) and with the results obtained in the one-component plasma (OCP) model, Fig. 2 also presents the maxima of the functions $g(r)$ and $S(q)$ that were obtained in [28, 29].

An analysis of the results of our numerical simulations shows that the spatial correlation of the grains in the systems under study is independent of the friction coefficient ν_{fr} and is determined completely by the

value of the effective parameter Γ*—from the values corresponding to systems in a gaseous state (Γ* ~ 1) to the values corresponding to the crystallization point (Γ* ~ 102–104). In all of the systems under investigation, the dust was observed to crystallize in body-centered cubic (bcc) lattice. The positions of the first maxima of the correlation functions $g(r)$ and $S(q)$ for a crystalline structure correspond to a bcc lattice: $d_{g1} \cong (3\sqrt{3}/4n_p)^{1/3}$, $d_{S1} \cong 2\pi(\sqrt{2}n_p)^{1/3}$, and $k_p = 2\pi n_p^{1/3}$ (see Fig. 3). The first maxima of $g(r)$ and $S(q)$ are seen to increase sharply (by a jump) in magnitude from 2.65 to 3.1 in the range of values of the normalized coupling parameter Γ* from the crystallization point, $\Gamma_c^* \cong 102$–104, to the melting point in the system, $\Gamma_{cm}^* \cong 106$–107 (Fig. 3). Hence, the value $\Gamma_{cm}^* \cong 104.5$ (±2) may serve as a criterion for the phase transition from a liquidlike system to a bcc lattice.

Since the value $\Gamma_{cm}^* \cong 104.5$ (±2%) is independent of the viscosity of the surrounding gas, this criterion agrees with the results of simulations of crystallization in Yukawa systems by the molecular dynamics methods in which the friction between particles is ignored [28–31]. The relevant results of these simulations differ from the value $\Gamma_{cm}^* \cong 104.5$ by no more than ±5%; this discrepancy can be attributed to the differences in the numerical methods used to analyze the system (different numbers of particles, different integration steps, etc.) and also to the choice of the Γ* value (either at the melting point or at the crystallization point). The calculated value $\Gamma_{cm}^* \cong 104.5$ (±2%) also agrees with the results of theoretical investigations carried out by Slattery *et al.* [32]. For the coupling parameter at the phase transition line in the OCP model, they obtained the value 105(±3%), which agrees with the results of calculations carried out for different criteria for liquid–crystal phase transitions (crystallization) [33] and crystal–liquid phase transitions (melting) [34].

To conclude this section, note that, since the shape of the correlation functions $g(r)$ in question, i.e., those satisfying condition (10), is determined by the value of the effective parameter Γ*, the methods for reconstructing the interparticle interaction potential from the experimental data on the structure factor on the basis of the hyperchain approximation, which makes use of the direct functional relationships between $g(r)$, $S(q)$, and $U(r)$ [5, 6, 29], are inapplicable to the systems under analysis. It should also be noted that the results obtained here can explain the wide use of different phenomenological criteria for crystallization and melting, which are formulated in terms of the fixed maximum values of the correlation functions or in terms of the fixed relationships between the maximum and minimum (at $r \neq 0$) values of these functions at the phase transition lines regardless of the type of interparticle interaction potential.

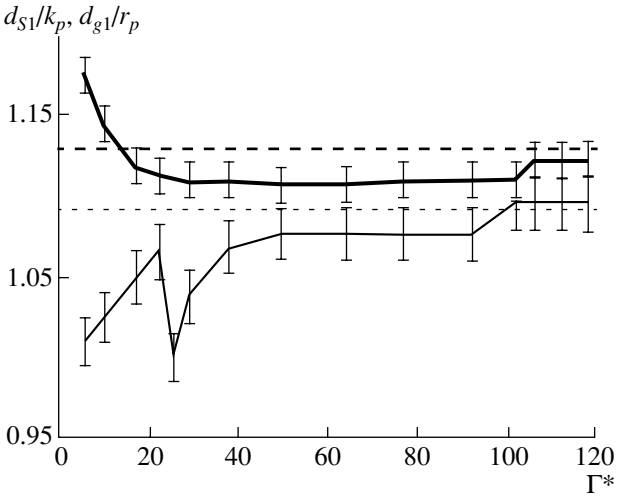

Fig. 3. Dependence of the relative position d_{S1}/k_p of the maximum of S_1 (heavy curve) and of the relative position d_{g1}/r_p of the maximum of g_1 (light curve) on Γ*. The dashed line and dotted line show the positions of the maxima of the correlation functions for a bcc lattice. The vertical bars show the absolute deviations for different values of the scaling parameter in the range ξ = 0.04–3.6 and for different potentials satisfying condition (10).

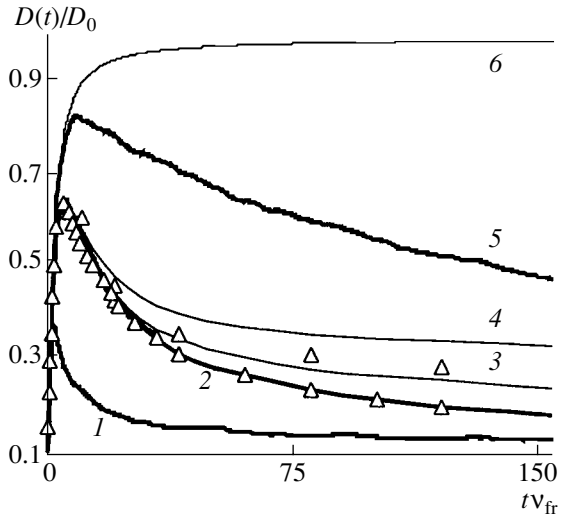

Fig. 4. Dependence of the ratio $D(t)/D_0$ on $t\nu_{fr}$ for the Yukawa potential (κ = 2.4) and for different values of the parameters ξ and Γ*: (*1*) ξ = 0.41, Γ* = 80; (*2*) ξ = 0.14, Γ* = 80; (*3*) ξ = 0.14, Γ* = 60; (*4*) ξ = 0.14, Γ* = 30; and (*5*) ξ = 0.04, Γ* = 80. Curve *6* shows the ratio $D(t)/D_0$ calculated from formula (12). The triangles show the points along curves *3* and *2* (with ξ = 0.14 and Γ* = 60 and 80, respectively) for which the calculations with the potential $U/U_c = \exp(-4.8r/r_p) + 0.05r_p/r$ were carried out.

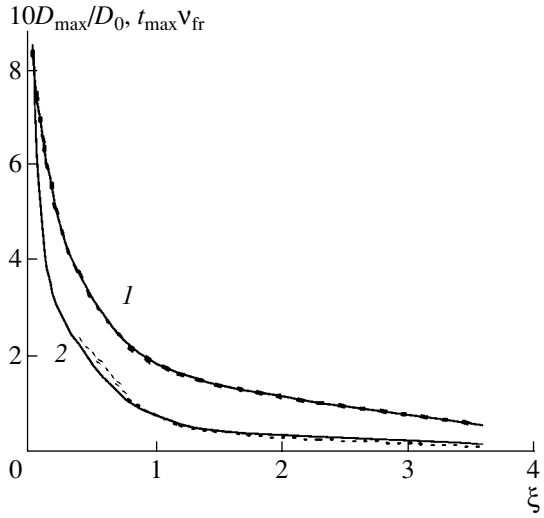

Fig. 5. Dependence of the ratio D_{max}/D_0 (curve *1*) and of the quantity $t_{max}\nu_{fr}$ (curve *2*) on the parameter ξ. The dotted curves show the approximations of D_{max}/D_0 and $t_{max}\nu_{fr}$ by relationships (13) and (14), respectively.

4. EVOLUTION OF THE MASS TRANSFER PROCESSES

In contrast to the phase states, the mass transfer processes in the systems under study are determined by the two main parameters, Γ* and ξ (see Fig. 4). The coefficient of diffusion of the dust grains, $D = \lim_{t\to\infty} D(t)$, and the time evolution of the dust mass transfer, $D(t)$, were analyzed based on the relationship

$$D(t) = \langle\langle|\mathbf{l}(t)-\mathbf{l}(0)|^2\rangle_N\rangle_t/6t \cong \frac{1}{N_p 6 N_t t_{jk}} \sum_{\substack{k=1 \\ (j-k)=\text{const}}}^{N_t} \sum_{i=1}^{N_p} (\Delta\mathbf{l}_i(t_{jk}))^2, \quad (11)$$

where $\Delta\mathbf{l}(t_{jk}) = \mathbf{l}(t_j) - \mathbf{l}(t_k)$ is the distance by which the ith particle is displaced during the time $t \equiv t_{jk} = (j-k)\Delta t$ from its initial position $\mathbf{l}_i(t_k)$ at the time t_k, $k = 1–N_t$, $j = k(N_t + k)$, Δt is the time resolution (determined, e.g., by the frame frequency of a video camera or the time interval between successive outputs of the information on the grain position in numerical solution of the problems), $N_t\Delta t$ is the total measurement time (e.g., the duration of a video recording or the run time of the code), the symbol $\langle\rangle_N$ denotes averaging over the ensemble (N), and the symbol $\langle\rangle_t$ denotes averaging over all time intervals of duration $t = t_{jk}$ during the total measurement time $N_t\Delta t$.

Figure 4 displays the dependence of the ratio of the function $D(t)$ for charged grains to the coefficient of diffusion of noninteracting Brownian grains, $D_0 = T/(\nu_{fr} m_p)$, on time (expressed in units of the inverse friction rate ν_{fr}^{-1}) for systems with different pair interaction potentials and with different values of the parameter ξ. Curve *6* is the exact solution to the Langevin equation for noninteracting grains [7]:

$$D(t)/D_0 = 1 - [1 - \exp(-\nu_{fr}t)]/\nu_{fr}t. \quad (12)$$

Hence, on time scales longer than the inverse friction rate ($\nu_{fr} \gg 1$), we have $D(t) = D_0$, whereas, on short time scales ($\nu_{fr}t \ll 1$), the grain undergoes ballistic motion: $\langle[\Delta l(t)]^2\rangle \approx 3Tt^2/m_p$ and $D(t) \propto t$.

When the interaction is taken into account, the behavior of the function $D(t)$ on short time scales remains the same and the ratio $D(t)/D_0$ on time scales $t < t_{max}/2$ is determined by formula (12) for noninteracting grains (see Fig. 4). On longer time scales, the function $D(t)$ reaches its maximum value D_{max}, which can be used to analyze the mass transfer processes for short observation times. Note that the coefficient D_{max} is smaller than D_0 and approaches the latter as the viscosity (ν_{fr}) of the surrounding gas increases. Figure 5 gives the dependences of the maximum value of the ratio $D(t)/D_0$ and its temporal position $t_{max}\nu_{fr}$ on the parameter ξ. It should be noted that the ratio D_{max}/D_0 and the temporal position $t_{max}\nu_{fr}$ are both independent of the parameter Γ*. An empirical fit of the numerical results for the curves $D(t)$ that decrease monotonically after reaching their maximum value yields the following relationship for the dependence $D_{max}(\xi)$:

$$D_{max} \approx D_0/(1 + b\xi). \quad (13)$$

For the temporal position t_{max} of the maximum of the ratio $D(t)/D_0$ in the case of weakly dissipative systems with $\xi > 0.25$, this empirical fit gives

$$t_{max}\nu_{fr} = \pi/[(b\xi)^2 - 1]^{1/2}, \quad (14)$$

where $b = 4$. Approximate relationships (13) and (14) describe the results of numerical simulations (see Fig. 5) with an accuracy of about 5%. The relationships were obtained by solving the problem of the motion of a one-dimensional oscillator whose frequency is given by the formula

$$\omega_c^2 = 2|U''(r_p)|/(\pi m_p) \equiv 4\omega^{*2}, \quad (15)$$

and corresponds to the characteristic oscillation frequency of particles in a bcc lattice [18]. The frequency ω_c is close to the mean oscillation frequency of particles in a liquidlike Yukawa system, obtained by processing the autocorrelation functions of their velocities [35]: $\omega_c^2 \approx (2\omega_\perp^2 + \omega_\parallel^2)/(4\pi)$, where $\omega_\perp$ and $\omega_\parallel$ are the frequencies of transverse and longitudinal oscillations, respectively.

The behavior of the functions $D(t)$ under analysis illustrates how statistical equilibrium is established in a slightly perturbed system. Simulations show that a system of interacting particles can be characterized by the equilibrium values of the transport coefficients only on time scales $t \gg t_{max}$; this is in contrast to a system of Brownian particles, for which we have $D(t) = D_0$ on time scales $t \gg \nu_{fr}^{-1}$. The analysis of the behavior of the function $D(t)$ for short observation times can be useful for obtaining independent estimates of the parameter ξ, which contains information about the interparticle interaction potential, and for recovering the dust grain temperature T (when the resolution of a measuring instrument is insufficient to correctly determine the velocity spectrum of dust grains).

5. THERMAL DIFFUSION COEFFICIENT

On infinitely long time scales ($t \longrightarrow \infty$), the function $D(t)$ (11) approaches its constant value $D = \lim_{t\to\infty} D(t)$, which corresponds to the standard definition of the particle diffusion coefficient as one of the main coefficients describing transport processes. The results of simulations of the diffusion of dust grains for different values of the scaling parameter ξ and for different model potentials (1)–(4) are illustrated in Fig. 6 in the form of the dependence of the ratio of the diffusion coefficient of the charged grains, D, to that of the Brownian grains, D_0, on the effective coupling parameter. It is easy to see that the diffusion coefficients of dust grains interacting by means of different potentials (1)–(4) are determined by the two main parameters, Γ^* and ξ. Recall that, as the effective coupling parameter increases to a value of $\Gamma^* \sim 106$, the dust in such systems crystallizes in a bcc lattice, in which case the diffusion coefficient of the grains decreases rapidly to zero (see Fig. 6).

The normalized function $D^* = D(1 + \xi)/D_0 \equiv D(\nu_{fr} + \omega^*)m_p/T_p$, averaged over all values $\xi \approx 0.045$–3.65 and over all potentials (1)–(4) used in simulations, is shown in Fig. 7. The scatter in the values of this function does not exceed ±5% for different values of the parameters under analysis (U and ξ) and for different values of Γ^*, except for the range of values of the effective coupling parameter from 22 to 30, in which the spread in the calculated D^* values is larger (±10%), and the diffusion coefficient depends nonmonotonically on Γ^* (see Figs. 6, 7). This latter result can be attributed to the formation of regular dust clusters at $\Gamma^* > 22$–25 and leads to conclusions about the possible effect of the type of intergrain interaction potential on the dynamics of the phase transition in question. The formation of such clusters, which was revealed earlier in numerical investigations of Yukawa systems [17, 36], provides a topological confirmation of the melting scenario observed in some experimental studies [36–38].

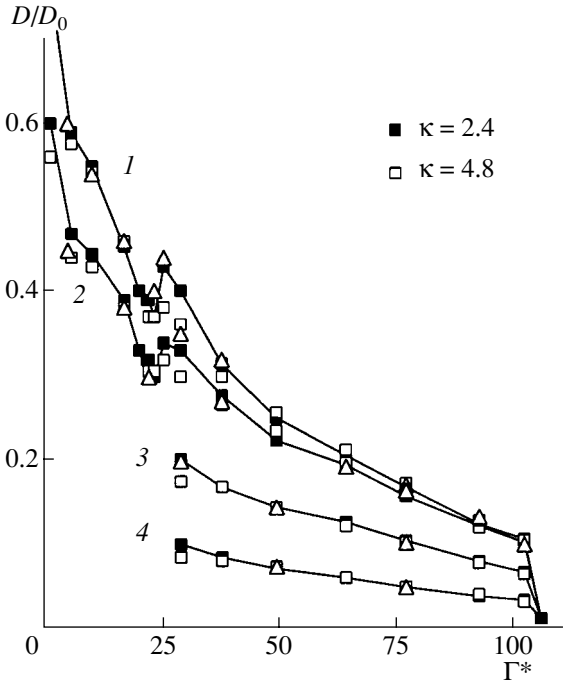

Fig. 6. Dependence of the ratio D/D_0 on the parameter Γ^* for Yukawa dissipative systems (closed and open squares) with different κ values [17] and systems with potentials (2)–(4) (triangles) whose parameters are given in the caption in Fig. 1 and for different values of the scaling parameter: ξ = (*1*) 0.14, (*2*) 0.41, (*3*) 1.22, and (*4*) 3.65.

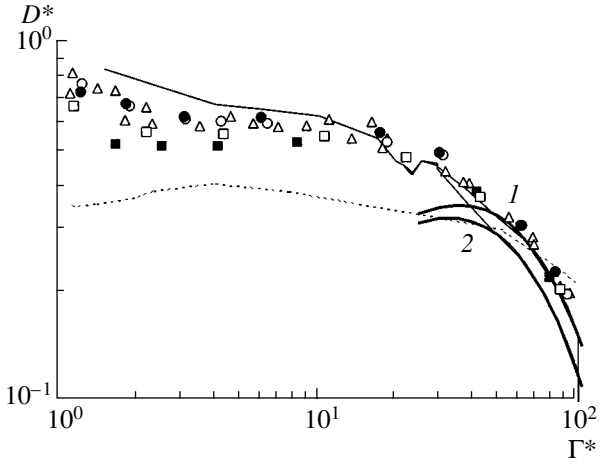

Fig. 7. Dependence of the normalized function D^* (light curves), averaged over the results of numerical simulations, on the parameter Γ^* and approximation of this function (heavy curves) by relationship (16) for (*1*) $\xi \geq 0.41$ and (*2*) $\xi \leq 0.14$. The values of D^* for Yukawa dispersive systems ($\xi \longrightarrow \infty$) [35] are also shown for $\kappa = 0.16$ (open circles), 0.48 (closed circles), 0.97–2.26 (triangles), 3.2 (open squares), 4.8 (closed squares), and 8 (dotted curve).

Hence, it is found that, for weakly correlated systems, as well as for strongly correlated systems, the normalized function D^* is determined by the effective

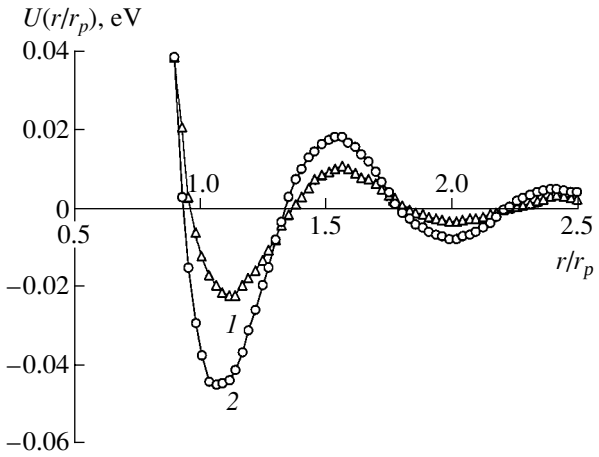

Fig. 8. Illustration of pair interaction potentials for sodium: curve *1* and triangles are for the first Parskin–Rahman potential and curve *2* and circles are for the second Parskin–Rahman potential.

coupling parameter Γ*. For strongly correlated systems, we have Γ* > 40–50 and the diffusion coefficient can be represented in a form analogous to that for Yukawa systems [17]:

$$D \cong \frac{T\Gamma^*}{12\pi(\omega^* + \nu_{fr})m_p}\exp\left(-c\frac{\Gamma^*}{\Gamma_c^*}\right), \qquad (16)$$

where $\Gamma_c^* = 102$ is the crystallization point, $c = 2.9$ for $\xi \geq 0.41$, and $c = 3.15$ for $\xi \leq 0.14$. For Γ* values from 50 to 102, the error of approximating the calculated D values by formula (16) does not exceed 3%. For smaller Γ* values (up to 40), the approximation error is larger, 7–13%, and, for $\Gamma^* \approx 30$, it is as large as 25–30%. Relationship (16) agrees with the theory of "jumps" developed for molecular liquids [1] and offers the possibility of determining the effective coupling parameter Γ* from the results of measurements of the mean distance between dust grains, their temperature, and their diffusion coefficient in liquidlike systems without making any additional assumptions about the shape of the pair intergrain interaction potential. The results from numerical calculations of D^* that are shown in Fig. 7 can be useful in diagnosing weakly correlated systems with Γ* < 50. Earlier, the forces of intergrain interactions in the processes of thermal diffusion of dust grains were taken into account by means of virial expansions or by using relationships analogous to those describing critical phenomena in liquids [2, 35, 39]. Both of these approaches require that the coefficients in the corresponding approximations be additionally recalculated for different values of the parameters of the system under consideration.

In order to compare the results calculated here with the results of calculations of the self-diffusion coefficient in dispersive Yukawa systems ($\nu_{fr} \equiv 0$, $\xi \longrightarrow \infty$), Fig. 7 also depicts the results of numerical simulations carried out by Ohta and Hamaguchi [35] for potentials with $\kappa \sim 0.15$–4.85 and for systems with $N_p = 600$–1000. It is easy to see that, for all values of the coupling parameter Γ* from about 15 to 100, the values of the normalized self-diffusion coefficient D^* for dispersive systems agree well (to within ±3%) with the results of simulations of weakly dissipative systems with $\xi \geq 0.41$. In contrast to the calculated results presented here (which were obtained by the Brownian molecular dynamics method and with periodic boundary conditions), Ohta and Hamaguchi [35] used a method based on solving the reversible equations of motion (this method requires that the calculated results be renormalized from time to time in order for the system to remain in thermodynamic equilibrium) and simulated a system consisting of an infinite number of particles by special tensor transformations. Because of the latter approximation, the final values of the diffusion coefficient can depend on the boundary conditions and, accordingly, can differ somewhat (by an amount of up to about 10–15% for Γ* < 15) from the numerical results given in Fig. 7.

To conclude this section, note that, as the screening parameter increases, potential (1) fails to satisfy condition (10) even for $\kappa > 5.1$. However, since condition (10) is empirical and merely determines the corresponding lower limit (for most of the potentials under discussion, the factor π in this condition can be replaced with 4), the transport properties of Yukawa systems are determined by the parameters (Γ*, ξ) up to $\kappa \sim 7$. A comparison of the D^* value for $\kappa \sim 8$ [35] with the numerical results obtained here for $\kappa < 5$ is given in Fig. 7.

6. TRANSPORT PROPERTIES OF SYSTEMS WITH ATTRACTIVE PAIR POTENTIALS BETWEEN GRAINS

Since condition (10), which determines the scales on which transport processes occur in nonideal systems with different potentials of interaction between the particles, was derived by analyzing different isotropic repulsive potentials (1)–(4), it is expedient to examine the transport properties of systems with attractive pair potentials between the grains. As an example, we consider the pair correlation functions $g(r)$ and the self-diffusion coefficients D calculated numerically by Parskin and Rahman [40] for two different attractive potentials (see Fig. 8). The first potential (shown by curve *1* in Fig. 8) agrees well with the data from measurements of the pair correlation function $g(r)$ for sodium at a temperature of about 100°C by a method based on neutron scattering and with the data from measurements of the diffusion of sodium atoms under the same conditions. The second potential (shown by curve *2* in Fig. 8) is close to the potentials calculated in [41] for sodium with the help of the Born–Green theory. Each of the two Parskin–Rahman potentials satisfies condition (10). In [40], the transport properties of sodium were calculated

by the molecular dynamics method (i.e., by solving the reversible equations of motion) for about 600 particles. Both the potentials were truncated at a distance of about 8.2 Å, the mean interparticle distance r_p being about 3.4 Å. The results from calculating the correlation functions and the function $D(t)$ are shown in Figs. 9 and 10. For the first potential (curve *1* in Fig. 8), the self-diffusion coefficient $D = \lim_{t\to\infty} D(t)$ was calculated to be about 5.8×10^{-5} cm^2/s, and the same coefficient for the second potential was found to be $D \approx 1.9 \times 10^{-5}$ cm^2/s.

It is easy to see that the pair correlation function calculated for the first potential is close to that calculated in the present paper for $\Gamma^* \approx 77$. For the coefficient of self-diffusion in liquid sodium ($\nu_{fr} \equiv 0$), formula (16) can be rewritten as

$$D \cong \frac{r_p}{12}\sqrt{\frac{T\Gamma^*}{\pi m_p}}\exp\left(-2.9\frac{\Gamma^*}{\Gamma_c^*}\right). \qquad (17)$$

For $\Gamma^* \approx 77$, formula (17) yields $D \approx 5.77 \times 10^{-5}$ cm^2/s, which is in complete accord with the results of [40]. Taking into account the maximum value of the correlation function calculated for the second potential (Fig. 9), we see that this value of the self-diffusion coefficient corresponds to the metastable region between the melting and crystallization lines for the system under investigation, $\Gamma^* \approx 104 \pm 2$ (see Fig. 2). This agrees well with the results of calculations of the r.m.s. deviation of the interparticle distance that were carried out by Randolph [42] for a potential close to the potential under consideration here (see curve *2* in Fig. 8). Randolph revealed that $\langle(\Delta l)^2\rangle$ behaves in a manner characteristic of those for solid bodies. It is incorrect to calculate the diffusion coefficient in the metastable region from formula (17) (see Fig. 6), because, in this case, the formula gives $D \approx 3 \times 10^{-5}$ cm^2/s, which is somewhat larger than the value $D \approx 1.9 \times 10^{-5}$ cm^2/s, obtained in [40].

It is worth noting that the temporal positions t_{max} of the maxima of the function $D(t)$ for the two Parskin–Rahman potentials agree completely with the values of the effective coupling parameter Γ^* obtained by analyzing the pair correlation functions (see Fig. 10). Thus, the Γ^* value calculated from relationship (14) for the first potential was found to be about $\Gamma^* \approx 76.5$ ($t_{max} \approx 1.44 \times 10^{-13}$ s) and the corresponding Γ^* value for the second potential was about 106.5 ($t_{max} \approx 1.22 \times 10^{-13}$ s). However, for both of the potentials, the values of the effective coupling parameter calculated from formula (13) with allowance for the maximum values D_{max} of the functions $D(t)$ were found to be underestimated: $\Gamma^* \approx 53.5$ ($D_{max} \approx 7.4 \times 10^{-5}$ cm^2/s) and $\Gamma^* \approx 84$ ($D_{max} \approx 5.9 \times 10^{-5}$ cm^2/s) for the first and second potentials, respectively. This could stem from the truncation of the pair interaction potentials at fairly short distances (~$2.5r_p$) as well as from an insufficiently large number of particles in the ensemble over which the averaging was performed [21].

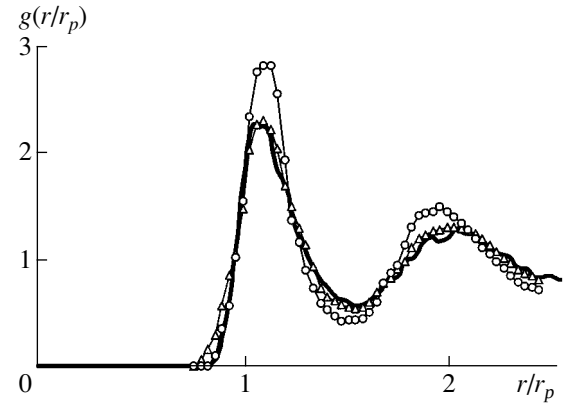

Fig. 9. Pair correlation functions $g(r/r_p)$ obtained in calculations [45] for the first (triangles) and second (circles) Parskin–Rahman potentials. The heavy curve shows the results of modeling the pair correlation function in a system with $\Gamma^* = 77$.

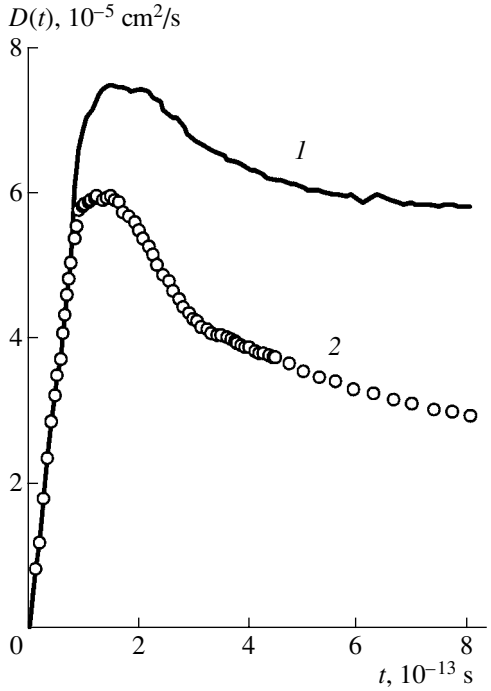

Fig. 10. Time dependences $D(t)$ calculated for (*1*) the first (solid curve) and for (*2*) the second (circles) Parskin–Rahman potentials [45].

To conclude this section, note that the existing data from measurements of the diffusion coefficient for liquid sodium at temperatures of $T \sim 100$°C yield $D \sim (3.8 \pm 4) \times 10^{-5}$ cm^2/s [41, 43], which agrees well with the results of calculations from formula (17):

$D(T = 100°C) \approx 3.3 \times 10^{-5}$ cm^2/s and $D(T = 125\ °C) \approx 4 \times 10^{-5}$ cm^2/s.

7. CONCLUSIONS

In the present paper, a numerical analysis has been carried out of the mass transfer and diffusion processes in the dust plasma component and of the spatial correlation between the dust grains interacting by means of various types of isotropic repulsive potentials over a wide range of phase states ($\Gamma^* \sim 1$–110) of nonideal systems. The dimensionless parameters that are responsible for the mass transfer process in the dust component and for the phase state of dissipative systems with long-range potentials obeying empirical condition (10) have been determined. These are the effective coupling parameter Γ^* and the scaling parameter ξ. Along with the particle temperature, they completely determine the transport properties of the systems under consideration. It has been shown that, for a wide variety of the isotropic potentials of the intergrain interaction, the shape of the pair correlation function $g(r)$ is determined by the value of the effective parameter Γ^*. This circumstance eliminates the possibility of recovering the shape of such potentials by inverting the function $g(r)$. An analytic approximation for the particle diffusion coefficient D in strongly nonideal systems (with $\Gamma^* > 50$) has been derived that makes it possible to determine the diffusion coefficient D as a function of the particle temperature T_p and of the parameters Γ^* and ξ.

The results obtained can be used to develop new methods for passive (nonintrusive) diagnostics of nonideal liquidlike systems and for the analysis of the effect of interparticle interaction on the transport properties of a system in the course of the experiment. The numerical model proposed here can also be applied to describe the properties of simple monatomic liquids, at least those that crystallize in bcc lattices, such as, e.g., liquid alkali metals. However, such a description requires an analysis of the transport properties of these liquids (such as the self-diffusion coefficients and pair correlation functions); this will be dealt with in our future papers.

ACKNOWLEDGMENTS

This work was supported in part by the Russian Foundation for Basic Research (project no. 04-02-16362) and INTAS (grant no. 01-0391).

REFERENCES

1. J. Frenkel, *Kinetic Theory of Liquids* (Nauka, Leningrad, 1945; Clarendon Press, Oxford, 1946).
2. H. Z. Cummins and E. R. Pike, *Photon Correlation and Light Beating Spectroscopy*, Ed. by H. Z. Cummins and E. R. Pike (Plenum Press, New York, 1974; Mir, Moscow, 1978).
3. B. Pullman, *Intermolecular Interactions: From Diatomics to Biopolymers* (Wiley, Chichester, 1978).
4. I. M. Torrens, *Interatomic Potentials* (Academic, New York, 1972).
5. R. Balescu, *Equilibrium and Nonequilibrium Statistical Mechanics* (Wiley, New York, 1975; Mir, Moscow, 1978).
6. N. K. Ailawadi, Phys. Rep. **57**, 241 (1980).
7. A. A. Ovchinnikov, S. F. Timashev, and A. A. Belyĭ, *Kinetics of Diffusion-Controlled Chemical Processes* (Khimiya, Moscow, 1986).
8. H. M. Thomas and G. E. Morfill, Nature (London) **379**, 806 (1996).
9. J. Chu and I. Lin, Phys. Rev. Lett. **72**, 4009 (1994).
10. H. Thomas, G. Morfill, V. Demmel, *et al.*, Phys. Rev. Lett. **73**, 652 (1994).
11. A. Melzer, T. Trottenberg, and A. Piel, Phys. Lett. A **191**, 301 (1994).
12. V. E. Fortov, A. P. Nefedov, V. M. Torchinskiĭ, *et al.*, Pis'ma Zh. Éksp. Teor. Fiz. **64**, 86 (1996) [JETP Lett. **64**, 92 (1996)].
13. A. M. Lipaev, V. I. Molotkov, A. P. Nefedov, *et al.*, Zh. Éksp. Teor. Fiz. **112**, 2030 (1997) [JETP **85**, 1110 (1997)].
14. U. Konopka, G. E. Morfill, and R. Ratke, Phys. Rev. Lett. **84**, 891 (2000).
15. J. E. Daugherty, R. K. Porteous, M. D. Kilgore, *et al.*, J. Appl. Phys. **72**, 3934 (1992).
16. J. E. Allen, Phys. Scr. **45**, 497 (1992).
17. D. Montgomery, G. Joyce, and R. Sugihara, Plasma Phys. **10**, 681 (1968).
18. O. S. Vaulina and S. V. Vladimirov, Plasma Phys. **9**, 835 (2002).
19. O. S. Vaulina, S. V. Vladimirov, O. F. Petrov, and V. E. Fortov, Phys. Rev. Lett. **88**, 245002 (2002).
20. V. E. Fortov, O. S. Vaulina, O. F. Petrov, *et al.*, Phys. Rev. Lett. **90**, 245005 (2003).
21. O. S. Vaulina, O. F. Petrov, V. E. Fortov, *et al.*, Fiz. Plazmy **29**, 698 (2003) [Plasma Phys. Rep. **29**, 642 (2003)].
22. V. E. Fortov, O. S. Vaulina, O. F. Petrov, *et al.*, Zh. Éksp. Teor. Fiz. **126**, 798 (2003) [JETP **96**, 704 (2003)].
23. V. V. Zhakhovskiĭ, V. I. Molotkov, A. P. Nefedov, *et al.*, Pis'ma Zh. Éksp. Teor. Fiz. **66**, 392 (1997) [JETP Lett. **66**, 419 (1997)].
24. O. S. Vaulina, A. P. Nefedov, O. F. Petrov, and V. E. Fortov, Zh. Éksp. Teor. Fiz. **118**, 1319 (2000) [JETP **91**, 1147 (2000)].
25. E. M. Lifshitz and L. P. Pitaevskiĭ, *Physical Kinetics* (Nauka, Moscow, 1979; Pergamon Press, Oxford, 1981).
26. N. A. Fuchs, *The Mechanics of Aerosols* (Dover, New York, 1964).
27. R. T. Farouki and S. Hamaguchi, Appl. Phys. Lett. **61**, 2973 (1992).
28. M. O. Robbins, K. Kremer, and G. S. Grest, J. Chem. Phys. **88**, 3286 (1988).
29. S. Ichimaru, Rev. Mod. Phys. **54**, 1017 (1982).
30. E. J. Meijer and D. Frenkel, J. Chem. Phys. **94**, 2269 (1991).

31. S. Hamaguchi, R. T. Farouki, and D. H. E. Dubin, Phys. Rev. E **56**, 4671 (1997).
32. W. L. Slattery, G. D. Doollen, and H. E. DeWitt, Phys. Rev. A **21**, 2087 (1980).
33. E. L. Plolloc and J. P. Hansen, Phys. Rev. A **8**, 3110 (1973).
34. H. M. van Horn, Phys. Lett. A **28A**, 707 (1969).
35. H. Ohta and S. Hamaguchi, Phys. Plasmas **7**, 4506 (2000).
36. O. S. Vaulina, O. F. Petrov, V. E. Fortov, *et al.*, Zh. Éksp. Teor. Fiz. (2005) (in press).
37. G. E. Morfill, H. M. Thomas, and M. Zuzic, *Advances in Dusty Plasma*, Ed. by P. K. Shukla, D. A. Mendis, and T. Dessai (World Scientific, Singapore, 1997), p. 99.
38. W. T. Juan, M. H. Chen, and I. Lin, Phys. Rev. E **64**, 016 402 (2001).
39. J. M. A. Hofman, Y. J. H. Clercx, and P. J. M. Schram, Phys. Rev. E **62**, 8212 (2000).
40. A. Parshin and A. Rahman, Phys. Rev. Lett. **16**, 300 (1966).
41. *Physics of Simple Liquids*, Ed. by H. N. V. Temperley, J. S. Rowlinson, and G. S. Rushbrooke (North-Holland, Amsterdam, 1968; Mir, Moscow, 1971).
42. P. D. Randolph, Phys. Rev. Lett. **134**, A1238 (1964).
43. *Handbook of Physical Quantities*, Ed. by I. S. Grigor'ev and E. Z. Meĭlikhov (Énergoatomizdat, Moscow, 1991).

Translated by G.V. Shepekina

Plasma Physics Reports, Vol. 30, No. 8, 2004, pp. 662–670. Translated from Fizika Plazmy, Vol. 30, No. 8, 2004, pp. 713–721.

PLASMA INSTABILITY

Vortex Electron Dynamics in a High-Current Plasma Lens

A. A. Goncharov*, V. I. Maslov, and I. N. Onishchenko****

** Institute of Physics, National Academy of Sciences of Ukraine, pr. Nauki 144, Kiev, 03039 Ukraine*

*** National Science Center Kharkov Institute for Physics and Technology, Akademicheskaya ul. 1, Kharkov, 61108 Ukraine*

Received March 26, 2003; in final form, October 20, 2003

Abstract—An analytic study is made of the following problems: the instability of a plasma against the excitation of vortex turbulence, the turbulence saturation amplitude, the types and spatial structures of the nascent vortices, and their nonlinear growth rates in an electrostatic plasma lens for focusing high-current ion beams.

1. INTRODUCTION

The objective of this paper is to analytically investigate the excitation of vortex turbulence in a plasma lens for focusing high-current ion beams [1, 2]. The radial focusing electric field in the lens is created by an electron cloud. At each point within the lens, the density of the cloud electrons n_{0e} is higher than the ion beam density n_{0i} by the amount $N_e \equiv n_{0e} - q_i n_{0i}/e$, where q_i and e are the charges of an ion and an electron, respectively. In other words, the space charge of an ion beam is overneutralized by the electrons of the plasma lens. The radial electron density distribution is approximately uniform, which ensures that the lens aberrations are low. The lens is in the form of a cylinder of finite length; the secondary electrons are emitted from its inner surface when it is bombarded by peripheral beam ions. It is these electrons that form the focusing cloud [1, 2]. The lens is in the magnetic field of a short solenoid. The solenoidal magnetic field structure is such that, as the emitted secondary electrons move from the ends of the cylinder toward its center, the field acts to displace them toward the solenoid axis.

The cylinder is separated along its length into several azimuthally symmetric rings, which are kept at definite electric potentials. Most of the electrons are confined within the plasma lens by the space charge of the ion beam during its transport. It is these electrons that make it possible to achieve high beam currents. The remaining electrons are confined within the plasma lens by the magnetic field of the short solenoid and by the electric field of the ring electrodes. It is these electrons that produce the radial electric field focusing an ion beam.

It was shown in [1–3], however, that such a plasma lens is unstable against the excitation of oscillating fields that act as a source of lens aberrations. The excitation of oscillations is attributed to the specific spatial structure of the magnetic field of the short solenoid: the longitudinal magnetic field $H_0(r)$ increases from the axis of the solenoid toward its surface. In other words, it is the positive radial magnetic field gradient $dH_0/dr > 0$ that causes the plasma to become unstable against the bunching of the electrons that are uniformly distributed over the lens.

Since the field configuration in the plasma lens is governed by the crossed radial focusing electric field E_{0r} and longitudinal magnetic field H_0, the electrons drift along the azimuthal coordinate θ with the velocity $V_{\theta 0} = -eE_{0r}/m_e\omega_{He} = (\omega_{pe}^2/2\omega_{He})(N_e/n_{0e})r \equiv r\omega_{\theta 0}$, where $\omega_{He} = eH_0/m_e c$ is the electron gyrofrequency.

Any perturbation of the initially uniform electron density gives rise to an electric field perturbation in its vicinity. Consequently, in the vicinity of the density perturbation, the field configuration is that of the crossed perturbed electric and longitudinal magnetic fields. This results in vortex electron dynamics in the field of the density perturbation. The vortex electron dynamics in crossed radial electric and longitudinal magnetic fields is being widely studied for the cases of a purely electron plasma [4–7] as well as charged and quasineutral plasmas [3, 8–12].

This paper is devoted to a theoretical study of the excitation of vortex perturbations in a plasma lens.

2. DYNAMIC EQUATIONS FOR NONLINEAR VORTEX PERTURBATIONS

Here, we derive equations describing the excitation of nonlinear vortex perturbations in a cylindrical plasma lens and the properties of these perturbations. To do this, we use the electron hydrodynamic equations

$$\partial_t \mathbf{V} + (\mathbf{V}\cdot\nabla)\mathbf{V} = (e/m_e)\nabla\varphi + \boldsymbol{\omega}_{He}\times\mathbf{V} - (V_{\text{th}}^2/n_e)\nabla n_e,$$
$$\partial_t n_e + \nabla(n_e\mathbf{V}) = 0, \quad (1)$$

where $\partial_t \equiv \partial/\partial t$ and the vector ω_{He} has the same direction as the magnetic field in the definition of ω_{He}.

1063-780X/04/3008-0662$26.00 © 2004 MAIK "Nauka/Interperiodica"

Assuming that the ions are unmagnetized, we describe them by the hydrodynamic equations

$$\begin{aligned} \partial_t \mathbf{V}_i + (\mathbf{V}_i \cdot \nabla)\mathbf{V}_i &= -(q_i/m_i)\nabla\varphi, \\ \partial_t n_i + \nabla(n_i \mathbf{V}_i) &= 0 \end{aligned} \tag{2}$$

and Poisson's equation for the electric potential φ,

$$\Delta\varphi = 4\pi(en_e - q_i n_i). \tag{3}$$

Here, $\mathbf{V}$ and n_e are the electron velocity and electron density, V_{th} is the electron thermal velocity, $\mathbf{V}_i$ and n_i are the ion density and ion velocity, and q_i and m_i are the charge and mass of an ion.

As will be shown below, the spatial scales on which the vortex perturbations occur are much larger than the electron Debye radius $r_{de} \equiv V_{\text{th}}/\omega_{pe}$, where $\omega_{pe} \equiv (4\pi n_{0e}e^2/m_e)^{1/2}$. This allows us to ignore the last term on the right-hand side of the first of Eqs. (1).

By analogy with [12], Eqs. (1) can be reduced to the equations

$$\begin{aligned} d_t[(\alpha - \omega_{He})/n_e] &= [(\alpha_0 - \omega_{He})/n_{e0}]\partial_z V_z, \\ d_{t0} V_z &= (e/m_e)\partial_z\varphi, \end{aligned} \tag{4}$$

$$d_t \equiv \partial_t + (\mathbf{V}_\perp \cdot \nabla_\perp),$$

$$\begin{aligned} d_{t0} &\equiv \partial_t + V_{\theta 0}\nabla_\theta = \partial_t + \omega_{\theta 0}\partial_\theta, \\ \partial_z &\equiv \partial/\partial z, \quad \partial_\theta \equiv \partial/\partial\theta, \end{aligned} \tag{5}$$

which describe the nonlinear transverse dynamics of the electrons and also their linear longitudinal dynamics under the assumptions $\boldsymbol{\omega}_{He} = \mathbf{e}_z\omega_{He}$ and $\partial_z\omega_{He} = 0$. In Eqs. (4), we take into account only the lowest order terms in the longitudinal perturbations; i.e., we omit the terms that are nonlinear in the longitudinal perturbations and also the terms that contain the products of the quantities describing the linear longitudinal perturbations with any of the quantities describing the transverse perturbations. There are three reasons for treating the longitudinal electron dynamics in a linear approximation: the length of the plasma lens is greater than its radius, the longitudinal scales of the vortex perturbations are close to the length of the lens, and the transverse scales of the perturbations are smaller than the lens radius. The notation in Eqs. (4) and (5) is as follows: $\mathbf{V}_\perp$ and V_z are the transverse and longitudinal electron velocities, respectively; $\mathbf{e}_z$ is a unit vector directed along the system axis; and the vorticity α, which characterizes the vortex motion of the electrons, is given by the expression

$$\alpha \equiv \mathbf{e}_z \cdot (\nabla \times \mathbf{V}) = r^{-1}\partial_r r V_\theta - r^{-1}\partial_\theta V_r, \tag{6}$$

where α_0 is the unperturbed value of α. The physical meaning of the vorticity α becomes especially obvious if we introduce the angular velocity of rotation of the electrons in the vortex, $\Omega \equiv V_\theta/r$, in terms of which the vorticity has the form

$$\alpha = 2\Omega + r\partial_r\Omega - r^{-1}\partial_\theta V_r. \tag{7}$$

For $\Omega \neq \Omega(r)$ and $V_r = 0$, the vorticity is two times the angular velocity of rotation of the electrons, $\alpha = 2\Omega$.

From Eqs. (1) we obtain the following equation for the transverse electron velocity $\mathbf{V}_\perp$:

$$\begin{aligned} \mathbf{V}_\perp &= (e/m_e\omega_{He})(\mathbf{e}_z \times \nabla_\perp\varphi) \\ &- \omega_{He}^{-1}\partial_t(\mathbf{e}_z \times \mathbf{V}_\perp) - \omega_{He}^{-1}(\mathbf{e}_z \times (\mathbf{V}_\perp \cdot \nabla_\perp)\mathbf{V}_\perp) \end{aligned} \tag{8}$$

or

$$\begin{aligned} \mathbf{V}_\perp &= -(e/m_e\omega_{He})(\mathbf{e}_z \times \mathbf{E}_{r0}) + (e/m_e\omega_{He})(\mathbf{e}_z \times \nabla_\perp\phi) \\ &- \omega_{He}^{-1}\partial_t(\mathbf{e}_z \times \mathbf{V}_\perp) - \omega_{He}^{-1}(\mathbf{e}_z \times (\mathbf{V}_\perp \cdot \nabla_\perp)\mathbf{V}_\perp), \\ \nabla\varphi &\equiv \nabla\phi - \mathbf{E}_{0r}. \end{aligned} \tag{9}$$

Retaining the lowest order (linear) terms in Eqs. (8) and (9) and taking the limit $(\omega_{pe}^2/\omega_{He}^2)(N_e/n_{0e}) \ll 1$, we get

$$\begin{aligned} \mathbf{V}_\perp &\approx (e/m_e\omega_{He})(\mathbf{e}_z \times \nabla_\perp\varphi) + (e/m_e\omega_{He}^2)\partial_t\nabla_\perp\varphi \\ &= \mathbf{V}_{\theta 0} + (e/m_e\omega_{He})(\mathbf{e}_z \times \nabla_\perp\phi) + (e/m_e\omega_{He}^2)\partial_t\nabla_\perp\phi. \end{aligned} \tag{10}$$

With allowance for the dependence $\omega_{He}(r)$, from Eq. (6) and relationship (10) we obtain the following approximate expression for the vorticity:

$$\begin{aligned} \alpha &\approx -2eE_{0r}/rm_e\omega_{He} - (eE_{0r}/m_e)\partial_r(1/\omega_{He}) \\ &+ (e/m_e\omega_{He})\Delta_\perp\phi + (e/m_e)(\partial_r\phi)\partial_r(1/\omega_{He}) \\ &+ (e/m_e)\partial_t(\mathbf{e}_z \cdot (\nabla_\perp \times \omega_{He}^{-2}\nabla_\perp\phi)) \\ &= (\omega_{pe}^2/\omega_{He})N_e/n_{e0} + r\omega_{pe}^2(N_e/2n_{e0})\partial_r(1/\omega_{He}) \\ &+ (e/m_e\omega_{He})\Delta_\perp\phi + (e/m_e)(\partial_r\phi)\partial_r(1/\omega_{He}) \\ &+ (e/m_e)\partial_t(\mathbf{e}_z \cdot (\nabla_\perp \times \omega_{He}^{-2}\nabla_\perp\phi)), \end{aligned} \tag{11}$$

where E_{0r} is the radial focusing electric field and ϕ is the electric potential of the vortex perturbation.

Expression (11) yields the following relationship for the unperturbed vorticity:

$$\begin{aligned} \alpha_0 &\approx -2eE_{0r}/rm_e\omega_{He} - (eE_{0r}/m_e)\partial_r(1/\omega_{He}) \\ &= (\omega_{pe}^2/\omega_{He})N_e/n_{e0} + r\omega_{pe}^2(N_e/2n_{e0})\partial_r(1/\omega_{He}). \end{aligned} \tag{12}$$

Expression (11) is convenient for the physical interpretation of the relation between the perturbation of the electron density δn_e and the vortex motion of electrons in a plasma lens. In order to understand this relation, we consider the limiting case in which the ions are assumed to be immobile and the radial magnetic field

gradient is ignored. In this case, Eq. (3) and expression (11) give the following approximate expression

$$\alpha \approx (\omega_{pe}^2/\omega_{He})N_e/n_{e0} + (\omega_{pe}^2/\omega_{He})\delta n_e/n_{e0}. \quad (13)$$

Here, the first term describes the electron motion along closed trajectories in the crossed fields of the plasma lens and the second term indicates that any perturbation δn_e of the electron density sets the electrons into vortex motion. Expression (13) also implies that, when the amplitude of the vortex perturbations is sufficiently small, the vorticity has the same sign over the entire plasma lens. In some regions within the lens, the vorticity can change its sign when the amplitudes of the vortices become larger than a certain value.

As will be shown below, the characteristic perturbation frequencies are on the order of the ion plasma frequency ω_{pi}. We take this circumstance into account and assume that the electron gyrofrequency is much higher than the electron plasma frequency, $\omega_{He} \gg \omega_{pe}$. We also retain terms up to first order in ω_{pe}/ω_{He} and use the fact that, according to expression (11), the vorticity α is proportional to $\omega_{pe}^2/\omega_{He}$. As a result, keeping only the lowest order terms in Eqs. (4), we arrive at the equations

$$d_t(\omega_{He}/n_e) \approx (\omega_{He}/n_{0e})\partial_z V_z, \quad d_{t0}V_z = (e/m_e)\partial_z\phi, \quad (14)$$

where the electron density n_e is determined from Poisson's equation:

$$n_e = n_{e0} + (q_i/e)\delta n_i + \Delta\phi/(4\pi e). \quad (15)$$

We single out the vortex motion in crossed fields with the velocity $V_{v\theta}$ in the azimuthal direction and the time derivative ∂_τ, which describes how the vortex perturbation changes with time, to obtain

$$\begin{aligned} d_t &= \partial_\tau + (\mathbf{V}_\perp \cdot \nabla_\perp) - V_{v\theta}\nabla_\theta, \\ d_{t0} \equiv \partial_\tau + V_{\theta 0}\nabla_\theta - V_{v\theta}\nabla_\theta &= \partial_\tau + \omega_{\theta 0}\partial_\theta - V_{v\theta}\nabla_\theta. \end{aligned} \quad (16)$$

Since the beam ions are heavy and fly rapidly (with the velocity V_{ib}) through the plasma lens, their dynamics can be described in a linear approximation. From Eqs. (2) we obtain the following equation for the ion density perturbation $\delta n_i = n_i - n_{i0}$:

$$\begin{aligned} (\partial_t - V_{ib}\partial_z)^2 n_i &\equiv (\partial_\tau - V_{ib}\partial_z - V_{v\theta}\nabla_\theta)^2 n_i \\ &= n_{i0}(q_i/m_i)\Delta\phi, \end{aligned} \quad (17)$$

where V_{ib} is the unperturbed longitudinal velocity of the ion beam.

Equations (9) and (14)–(17) describe the excitation and properties of finite-amplitude vortex perturbations. In what follows, we will use these equations to describe the structure of vortex perturbations, the excitation of linear vortex perturbations, and the excitation of nonlinear small-amplitude vortex perturbations.

3. LINEAR THEORY OF THE DEVELOPMENT OF INSTABILITY IN A PLASMA LENS

We first consider the development of instability in the linear approximation. To do this, we derive the linear dispersion relation for the oscillations excited in a cylindrical plasma lens. Representing the dependence of the perturbed quantities on z and θ in the form $\exp(ik_z z + il_\theta\theta)$, from Eq. (17) we obtain

$$\delta n_i = -n_{i0}(q_i/m_i)\Delta\phi/(\omega - k_z V_{ib})^2, \quad (18)$$

where k_z and l_θ are the longitudinal and azimuthal wavenumbers of the perturbation, ω is the perturbation frequency, and V_{ib} is the unperturbed longitudinal velocity of the ion beam. Substituting expression (18) into Eq. (15) yields

$$\begin{aligned} \beta\Delta\phi/4\pi e = \delta n_e, \quad \beta = 1 - \omega_{pi}^2/(\omega - k_z V_{ib})^2, \\ n_e = n_{0e} + \delta n_e. \end{aligned} \quad (19)$$

In the linear approximation, Eqs. (14) become

$$\begin{aligned} d_t(\omega_{He}/n_e) = -(e\omega_{He}/m_e n_{e0})ik_z^2\phi/(\omega - l_\theta\omega_{\theta 0}), \\ \omega_{\theta 0} \equiv V_{\theta 0}/r. \end{aligned} \quad (20)$$

Equations (19) and (20) give the following equation for ϕ:

$$\begin{aligned} (\omega_{pe}^2/\omega_{He}^2)\nabla_\theta\phi\partial_r\omega_{He} + \beta(\partial_t\Delta\phi + \omega_{\theta 0}\partial_\theta\Delta\phi) \\ = ik_z^2\phi\omega_{pe}^2/(\omega - l_\theta\omega_{\theta 0}). \end{aligned} \quad (21)$$

Under the assumption that the radial gradient of the magnetic field of a short solenoid, $\partial_r H_0$, is independent of radius, from Eq. (21) we obtain the following linear dispersion relation, which describes the development of instability:

$$\begin{aligned} 1 - \omega_{pi}^2/(\omega - k_z V_{bi})^2 \\ - \omega_{pe}^2(l_\theta/r)\partial_r(1/\omega_{He})/[k^2(\omega - l_\theta\omega_{\theta 0})] \\ - \omega_{pe}^2 k_z^2/[k^2(\omega - l_\theta\omega_{\theta 0})^2] = 0, \end{aligned} \quad (22)$$

where k is the wavenumber.

4. EXCITATION OF SMALL-AMPLITUDE FAST VORTEX PERTURBATIONS

By fast vortex perturbations, we mean the perturbations whose phase velocity is close to the azimuthal electron drift velocity, $V_{\rm ph} \approx V_{\theta 0}$. In turn, by the phase velocity, we mean the quantity $V_{\rm ph} \equiv {\rm Re}(\omega/k_\theta)$, where ${\rm Re}\,\omega$ is the real part of the frequency and k_θ is the azimuthal component of the wave vector. In the approximation in which $k_z = 0$, $\omega = \omega^{(0)} + \delta\omega$, and $|\delta\omega| \ll \omega^{(0)}$, linear dispersion relation (22) for fast vortex perturbations gives

$$\omega^{(0)} = \omega_{pi} = l_\theta\omega_{\theta 0},$$

$$\omega_{\theta 0} = (\omega_{pe}^2/2\omega_{He})(N_e/n_{0e}), \quad N_e \equiv n_{0e} - q_i n_{0i}/e, \quad (23)$$

$$\delta\omega = i\gamma_q, \quad \gamma_q \approx (\omega_{pe}/k)[(\omega_{pi}/2)(l_\theta/r)|\partial_r(1/\omega_{He})|]^{1/2},$$

where n_{0i} is the unperturbed ion density.

Formulas (23) imply that the azimuthal wavenumber of the excited vortex perturbations is equal to

$$l_\theta = \omega_{pi}/\omega_{\theta 0} = 2(m_e/m_i)^{1/2}(\omega_{He}/\omega_{pe})(n_{0e}/N_e). \quad (24)$$

From this expression we see that, for typical experimental parameters ($N_e/n_{0e} \approx 0.1$), the perturbations that are excited in a strong magnetic field at a low electron density are those with $l_\theta > 1$.

Formulas (23) also imply that the frequency at which fast vortex perturbations are excited is equal to the ion plasma frequency ω_{pi} and that the rate γ_q at which the perturbations grow is proportional to the square root of the radial magnetic field gradient $(\partial_r H_0)^{1/2}$.

In deriving formulas (23), we used the inequality

$$(N_e/n_{0e})(r/\omega_{He})\omega_{pe}^2|\partial_r(1/\omega_{He})| \ll m_e/m_i, \quad (25)$$

which is valid provided that the space charge of an ion beam is slightly overneutralized by the electrons of the lens ($N_e/n_{0e} \ll 1$), the electron gyrofrequency ω_{He} is slightly nonuniform, and the plasma density is low ($\omega_{pe}/\omega_{He} \ll 1$).

5. EXCITATION OF SMALL-AMPLITUDE SLOW VORTEX PERTURBATIONS

By slow vortex perturbations, we mean the perturbations whose phase velocity is much lower than the azimuthal electron drift velocity, $V_{\rm ph} \ll V_{\theta 0}$. At $k_z = 0$, linear dispersion relation (22) for such perturbations gives

$$\gamma_s \approx (\sqrt{3}/2^{4/3})[\omega_{pi}^2 l_\theta(\omega_{pe}^2/2\omega_{He})(N_e/n_{0e})]^{1/3}$$
$$= (\sqrt{3}/2^{4/3})[\omega_{pi}^2 l_\theta \omega_{\theta 0}]^{1/3}, \quad (26)$$
$$k^2 = -(1/V_{\theta 0})\omega_{pe}^2\partial_r(1/\omega_{He}), \quad {\rm Re}\,\omega_s = \gamma_s/\sqrt{3}.$$

where γ_s is the growth rate of the small-amplitude slow vortex perturbations and ${\rm Re}\,\omega_s$ is the real part of their frequency. From expressions (26) we see that the spatial scales on which slow vortex perturbations are excited are inversely proportional to the square root of the radial magnetic field gradient, $(\partial_r H_0)^{1/2}$. In other words, the smaller the magnetic field gradient, the wider the slow vortices. Expressions (26) also show that the growth rate of the slow vortex perturbations is proportional to the cube root of the angular frequency of rotation of the electrons in the crossed fields of the plasma lens, i.e., to the cube root of the degree to which the plasma is nonequilibrium.

Expressions (26) for the growth rate were derived under the inequality

$$l_\theta \gg (n_{0e}/N_e)2\omega_{pi}\omega_{He}/\omega_{pe}^2. \quad (27)$$

Using expressions (26) and inequality (27), it can be shown that the phase velocity of the perturbations is in fact much lower than the azimuthal electron drift velocity, $V_{\rm ph} \ll V_{\theta 0}$, and that the azimuthal wavenumbers l_θ of the excited perturbations are small.

Let us now consider how the finite value of the longitudinal wavenumber, $k_z \neq 0$, affects the instability growth rate. Taking into account the nonzero wavenumber k_z, from linear dispersion relation (22) we obtain the following expression for the growth rate of the slow vortex turbulence:

$$\gamma_s \approx (\sqrt{3}/2^{4/3})\omega_{pi}^{2/3}(l_\theta\omega_{\theta 0} - k_z V_{bi})^{1/3} \quad (28)$$
$$\times\{1 - k_z^2/[2k_z^2 + (l_\theta/r)(l_\theta\omega_{\theta 0} - k_z V_{bi})|\partial_r(1/\omega_{He})|]\}^{1/3}.$$

From this expression, we see that, when the longitudinal dynamics of the ions and electrons is taken into account, the result is that the growth rate becomes slower. The fastest growing perturbations are those with the smallest azimuthal wavenumbers k_z ($\approx \pi/L$), i.e., with the greatest longitudinal dimensions, which are close to the length of the plasma lens.

Comparing expressions (23) and (26) and using inequalities (25) and (27), it can be shown that the growth rate of slow vortex perturbations substantially exceeds that of fast vortex perturbations, $\gamma_s \gg \gamma_q$.

6. SPATIAL STRUCTURE OF A FAST VORTEX

Here, we describe the spatial structure of a fast vortex in a frame of reference in which the vortex is at rest and is steady. In other words, we consider the vortex in a frame of reference that rotates with the angular velocity $\omega_{\rm ph} \equiv V_{\rm ph}/r_q$, where r_q is the radial position of the vortex center. The instability that develops in an initially homogeneous plasma gives rise to a series of closely spaced regions in which the electron density is alternately elevated and depressed (for brevity, these regions will be referred to as electron bunches and electron cavities, respectively). We thus consider a sequence of alternating electron-bunch and electron-cavity vortices that is stretched along the azimuthal coordinate θ. In the approximation $(\omega_{pe}^2/\omega_{He}^2)(N_e/n_{0e}) \ll 1$, we ignore the time-dependent terms and the terms that are nonlinear in ϕ and obtain from Eqs. (9) the expression

$$\mathbf{V}_\perp = -e/(m_e\omega_{He})(\mathbf{e}_z \times \mathbf{E}_{r0}) + e/(m_e\omega_{He})(\mathbf{e}_z \times \nabla\phi), \quad (29)$$

which describes the quasi-steady electron dynamics in the fields of the plasma lens and of the vortex perturbation. Expression (29) gives the following expressions

for the radial and azimuthal components of the electron velocity:

$$V_r = -e/(m_e\omega_{He})\nabla_\theta\phi, \quad V_\theta = V_{\theta 0} + e/(m_e\omega_{He})\nabla_r\phi,$$
$$V_{\theta 0} = -e/(m_e\omega_{He})E_{r0} = (\omega_{pe}^2/2\omega_{He})(N_e/n_{0e})r. \quad (30)$$

We represent the azimuthal electron velocity V_θ as a sum of the phase velocity V_{ph} of the perturbation and the electron oscillatory velocity δV_θ in the azimuthal direction, $V_\theta = V_{ph} + \delta V_\theta$. Since, by definition, we have $V_\theta = rd\theta/dt$, we can represent the time derivative $d\theta/dt$ in the form $d\theta/dt = d\theta_1/dt + \omega_{ph}$, where $\omega_{ph} = (N_e/n_{0e})(\omega_{pe}^2/2\omega_{He})|_{r=r_q}$. From expressions (30) we then obtain the equations

$$d\theta_1/dt = (\omega_{pe}^2/2)(N_e/n_{0e})[1/\omega_{He}(r) - 1/\omega_{He}(r_q)] + e/(rm_e\omega_{He})\partial_r\phi, \quad (31)$$
$$dr/dt = -e/(m_e\omega_{He}r)\partial_\theta\phi.$$

We consider small deviations of r from r_q and take into account only the first nonzero term in the expansion of $\omega_{He}(r)$ in powers of $\delta r \equiv r - r_q$ in the vicinity of r_q. We then integrate Eqs. (31) to obtain the equation

$$(\delta r)^2 - 2\omega_{He}(r_q)\phi/[\pi e N_e r_q(\partial_r\omega_{He})|_{r=r_q}] = \text{const}, \quad (32)$$

which describes the electron oscillatory dynamics in the field of the vortex perturbation.

Using Eq. (32), we can show that the hump of the electric potential acts to trap the electrons and thereby to form a vortex. Let us determine the vortex boundary, i.e., the boundary between the trapped electrons, which move along closed orbits and form the vortex, and the transit electrons, which move outside the vortex and oscillate in its field. Using Eqs. (31), we can show that, in a frame of reference rotating with the angular velocity $\omega_{ph} = (N_e/n_{0e})(\omega_{pe}^2/2\omega_{He})|_{r=r_q}$, the electrons trapped by the cavity and the electrons trapped by the bunch rotate in opposite directions. Specifically, the electrons that are trapped by the bunch rotate in a clockwise direction. Note that, in the laboratory frame of reference, all the electrons also drift in the clockwise direction with the angular velocity $V_{\theta 0}/r$ along the azimuthal coordinate θ. In addition, from Eqs. (31), we can see that the electrons that are at large distances from the vortex boundary lag behind the vortex, while the electrons that are near the boundary of the vortex overtake it.

Using Eq. (32), from the condition $\delta r|_{\phi=-\phi_0} = \delta r_{cl}$ we obtain the following expression for the boundary of the electron-bunch vortex:

$$\delta r = \pm\{2(\phi + \phi_0) \times \omega_{He}(r_q)/[\pi e N_e r_q(\partial_r\omega_{He})|_{r=r_q}] + (\delta r_{cl})^2\}^{1/2}, \quad (33)$$

where δr_{cl} is the radial width of the vortex. Expressions (33) describe electron motion along the electron-bunch vortex boundary. From expression (33) we obtain the radial width of the electron-cavity vortex:

$$\delta r_q = [4\phi_0\omega_{He}(r_q)/[\pi e N_e r_q(\partial_r\omega_{He})|_{r=r_q}] + (\delta r_{cl})^2]^{1/2}. \quad (34)$$

From this expression, we see that the radial width of the electron-cavity vortex is greater than δr_{cl}. We also see that this width is inversely proportional to $[(N_e/n_{0e})(\omega_{pe}/\omega_{He})\partial_r\omega_{He}]^{1/2}$ and is directly proportional to $\phi_0^{1/2}$; in other words, the radial width of the electron-cavity vortex depends strongly on the radial magnetic field gradient and on the vortex amplitude. For small values of the ratios $N_e/2n_{0e}$ and ω_{pe}/ω_{He}, the radial width δr_q of the vortex at low values of ϕ_0 and (of course) at small electron density perturbations can become as large as $\delta r_q \approx R/2$, where R is the plasma lens radius.

Note that Eqs. (31) in which the electron gyrofrequency $\omega_{He}(r)$ is not expanded in powers of $\delta r \equiv r - r_q$ is also integrable. To see this, we approximate the electron gyrofrequency by $\omega_{He}(r) = \omega_{H0}(1 + \mu r^2/R^2)$. We can then integrate these equations to get

$$2\phi + \pi e N_e r^2[1 - \omega_{H0}/2\omega_{He}(r_q) - \omega_{He}(r)/2\omega_{He}(r_q)] = \text{const}. \quad (35)$$

From the condition $r|_{\phi=-\phi_0} = r_q + \delta r_{cl}$ and from solution (35) we obtain the following equation for the boundary of the electron-cavity vortex:

$$2(\phi + \phi_0)R^2\omega_{He}(r_q)/(\omega_{H0}\mu\pi e N_e) + r_q^2[r^2 - (r_q + \delta r_{cl})^2] - [r^4 - (r_q + \delta r_{cl})^4]/2 = 0. \quad (36)$$

In turn, Eq. (36) and the condition $r|_{\phi=-\phi_0} = r_q + \delta r_q$ yield the equation for the radial width of the electron-cavity vortex:

$$\phi_0 4R^2\omega_{He}(r_q)/(\pi e N_e\omega_{H0}\mu) = (\delta r_q - \delta r_{cl})(2r_q + \delta r_q + \delta r_{cl}) \times [r_q(\delta r_q + \delta r_{cl}) + (\delta r_q^2 + \delta r_{cl}^2)/2]. \quad (37)$$

7. STRUCTURE OF A SLOW VORTEX

Here, we consider a vortex whose phase velocity V_{ph} is much lower than the electron drift velocity, $V_{ph} \ll V_{\theta 0}$. In contrast to the case of a fast vortex, all the electrons

overtake a small-amplitude slow vortex by virtue of the condition $V_{ph} \ll V_{\theta 0}$.

In the laboratory frame, all of the electrons in a small-amplitude slow vortex rotate in a clockwise direction because, for such a vortex, the vorticity α has the same sign over the entire plasma lens, $\alpha > 0$.

To describe the spatial structure of the electron trajectories in the field of a small-amplitude slow vortex, we turn to Eqs. (30). We insert the definition $V_\theta = rd\theta/dt$ into these equations and eliminate θ in them to obtain the following equation for the electron trajectories in the field of a sequence of small-amplitude slow vortices that is stretched along the azimuthal coordinate θ:

$$r^2 + \phi/(\pi e N_e) = \text{const}. \tag{38}$$

Equation (38) describes the radial positions of the electrons through the dependence of the electric potential $\phi(\theta, r)$ on θ and r. It is also instructive to describe the radial positions of the electrons in terms of the dependence of their perturbed density $\delta n_e(\theta, r)$ on θ and r. To do this, we ignore k_z to obtain from Eqs. (16) and linearized equation (20) the equation

$$r - (\partial_r \omega_{He})^{-1}(\omega_{H0}/n_{e0})\delta n_e = \text{const}. \tag{39}$$

From Eq. (39), we see that the smaller the radial magnetic field gradient, the larger the amplitude of the radial oscillations of the electrons at a given amplitude of their density perturbation.

The structure of the slow vortices changes radically when their amplitudes become so large that the vorticity α no longer has the same sign ($\alpha > 0$) over the entire plasma lens. Namely, according to approximate expression (11), the vorticity α changes sign, $\alpha < 0$, within the electron cavities in a sequence of vortices of sufficiently large amplitudes (such that $\delta n_e > N_e$). In this case, within the electron-cavity vortices, the electrons rotate in the direction opposite to that of their rotation in the crossed fields of the plasma lens. Unlike in the case of a fast vortex, all of the electrons that move outside a large-amplitude slow vortex overtake it by virtue of the inequality $V_{ph} \ll V_{\theta 0}$. Under the condition $\delta n_e > N_e$, a slow vortex is similar in structure to the Rossby vortex [13].

8. EXCITATION OF NONLINEAR VORTICES

Here, we describe the excitation of small-amplitude nonlinear vortex perturbations to within terms containing quadratic nonlinearities. In this way, we describe the excitation of individual nonlinear vortices in the sequence; it will be seen later that the amplitude ϕ_0 of the individual vortices is smaller than the saturation amplitude of the strongly nonlinear individual vortices, $\phi_0 < \phi_{sm}$.

We use two small parameters—the small ratio $\omega_{pe}/\omega_{He} \ll 1$ and the small vortex amplitude ϕ_0. Since $\omega_{pe} \gg \omega$, we have $\omega/\omega_{He} \ll 1$ (where ω is the perturbation frequency). Comparing the second term on the left-hand side of the first of Eqs. (1) with the second term on the right-hand side of this equation, we see that the amplitude can be assumed to be small under the inequality

$$\phi_0 \ll (m_e/e)\omega_{He}^2 R^2/\pi^2. \tag{40}$$

A comparison of inequality (40) with relationship (62) (see below) shows that the amplitude of the vortex can be regarded as small if it is smaller than the saturation amplitude of the strongly nonlinear individual vortices, $\phi_0 \ll \phi_{sm}$.

Above, we have arrived at the following conclusion based on expression (28): the only vortices that are excited are those with the shortest possible longitudinal inhomogeneity scales consistent with the length of the plasma lens. This conclusion allows us to treat nonlinear vortices in the limit $k_z = 0$.

Since the ions fly rapidly through the plasma lens and are much heavier than the electrons, we can describe them in a linear approximation. In this case, the vortices can be described by Eqs. (9) and (16) and also, in accordance with Eqs. (14), (15), and (17), by the equations

$$\begin{gathered} d_t(\omega_{He}/n_e) \approx 0, \\ n_e = n_{e0} + (q_i/e)\delta n_i + \Delta_\perp \phi/(4\pi e), \end{gathered} \tag{41}$$

$$\partial_t^2 n_i \equiv (\partial_\tau - V_{v\theta}\nabla_\theta)^2 n_i = n_{i0}(q_i/m_i)\Delta_\perp \phi. \tag{42}$$

Using the time-independent linear terms of Eq. (9), or, equivalently, the time-independent terms of Eq. (10),

$$\mathbf{V}_\perp \approx \mathbf{V}_{\theta 0} + e/(m_e \omega_{He})(\mathbf{e}_z \times \boldsymbol{\nabla}_\perp \phi), \tag{43}$$

we obtain from Eqs. (16) and (41) the following nonlinear evolutionary equation, which contains higher order nonlinear terms and describes, together with Eq. (42), the excitation of nonlinear vortices and their spatial structure:

$$\begin{gathered} [\partial_\tau + (\mathbf{V}_{\theta 0} - \mathbf{V}_{v\theta}) \cdot \boldsymbol{\nabla}_\theta \\ + e/(m_e \omega_{He})((\mathbf{e}_z \times \boldsymbol{\nabla}_\perp \phi) \cdot \boldsymbol{\nabla}_\perp)]\omega_{He}/[n_{e0} \\ + (q_i/e)\delta n_i + \Delta_\perp \phi/(4\pi e)] \approx 0. \end{gathered} \tag{44}$$

Ignoring the nonlinear terms reduces Eqs. (42) and (44) to Eqs. (19) and (20) with $k_z = 0$, which describe the excitation of perturbations in a linear approximation. In the next two sections, we will use Eqs. (42) and (44) as the basis for describing nonlinear vortices.

9. EXCITATION OF A NONLINEAR SLOW VORTEX

In the steady-state case and without allowance for the interaction with ions, Eq. (44) yields the following

equation for a slow vortex whose azimuthal rotation velocity is low ($V_{\theta s} \ll V_{\theta 0}$):

$$[(V_{\theta 0} - V_{s\theta})\nabla_\theta + e/(m_e\omega_{He})((\mathbf{e}_z \times \boldsymbol{\nabla}_\perp\phi)\cdot\boldsymbol{\nabla}_\perp)] \times (\omega_{pe}^2 + \Delta_\perp\phi e/m_e)/\omega_{He} \approx 0. \quad (45)$$

Taking into account the fact that the unperturbed electron density is uniform in the radial direction, we can rewrite Eq. (45) as

$$(V_{\theta 0} - V_{s\theta})\boldsymbol{\nabla}_\theta\Delta_\perp\phi - (\boldsymbol{\nabla}_\theta\phi)\omega_{pe}^2\partial_r(1/\omega_{He}) + (e/m_e\omega_{He})((\mathbf{e}_z \times \boldsymbol{\nabla}_\perp\phi)\cdot\boldsymbol{\nabla}_\perp)\Delta_\perp\phi \approx 0. \quad (46)$$

It is seen that the dimensions of the vortex are determined by its amplitude ϕ_0; the radial nonuniformity of the electron gyrofrequency ω_{He}; and the extent to which the space charge of an ion beam is overneutralized, N_e/n_{0e} (in the expression for $V_{\theta 0}$). The higher the nonuniformity of the electron gyrofrequency ω_{He} and the less the extent N_e/n_{0e} to which the beam is overneutralized, the smaller the vortex with a fixed amplitude ϕ_0.

Equation (46) can be rewritten as

$$\begin{aligned}&(1 - V_{s\theta}/V_{\theta 0})\boldsymbol{\nabla}_\theta\Delta_\perp\phi \\ &- 2\omega_{He}(n_{0e}/N_e)(\boldsymbol{\nabla}_\theta\phi)r^{-1}\partial_r(1/\omega_{He}) \\ &+ 2(e/m_e\omega_{pe}^2)r^{-1}(n_{0e}/N_e)\{\phi, \Delta_\perp\phi\}_{r,\theta} = 0, \quad (47)\\ &\{\phi, \Delta_\perp\phi\}_{r,\theta} \equiv (\boldsymbol{\nabla}_r\phi)\boldsymbol{\nabla}_\theta\Delta_\perp\phi - (\boldsymbol{\nabla}_\theta\phi)\boldsymbol{\nabla}_r\Delta_\perp\phi \\ &= r^{-1}[(\partial_r\phi)(\partial_\theta\Delta_\perp\phi) - (\partial_\theta\phi)(\partial_r\Delta_\perp\phi)].\end{aligned}$$

Recall that the azimuthal rotation velocity of a slow vortex satisfies the condition $V_{\theta s} \ll V_{\theta 0}$. In the steady-state case, Eq. (47) for a slow vortex reduces to the corresponding equation derived in [8].

Let us now describe the excitation of a slow vortex. To do this, we take into account the ion contribution to Eq. (44) and retain the time-dependent terms (i.e., those with ∂_τ) in this equation. As a result, we arrive at the approximate equation

$$\partial_\tau\Delta_\perp\phi \approx -4\pi q_i(V_{\theta 0}\nabla_\theta))\delta n_i. \quad (48)$$

From Eqs. (42) and (48) we obtain the following partial differential equation, which describes the excitation of the vortex:

$$\partial_\tau^3\Delta_\perp\phi \approx -\omega_{pi}^2(V_{\theta 0}\nabla_\theta)\Delta_\perp\phi. \quad (49)$$

We ignore the change in the angular velocity of the vortex due to its interaction with the ions and use the relationship $\partial_\tau\phi = \gamma_{NLs}\phi$ (where γ_{NLs} is the nonlinear rate at which a slow vortex is excited) to represent Eq. (49) in the form

$$\gamma_{NLs}^3\Delta_\perp\phi \approx -\omega_{pi}^2(V_{\theta 0}\nabla_\theta)\Delta_\perp\phi. \quad (50)$$

We introduce the quantity $l_{\theta NL}$ through the relationship $\partial_\theta\phi|_{\phi = \phi_0/2} \equiv l_{\theta NL}\phi_0/2$. It can be seen that the quantity $l_{\theta NL}$ so introduced is determined by the angular dimensions of the vortex. Using Eq. (50), we can estimate the nonlinear rate of excitation of a slow vortex by

$$\gamma_{NLs} \approx [\omega_{pe}^2\omega_{\theta 0}l_{\theta NL}(m_e/m_i)]^{1/3} = (\omega_{pi}^2\omega_{\theta 0}l_{\theta NL})^{1/3}. \quad (51)$$

In the linear approximation, the quantity $l_{\theta NL}$ is the linear azimuthal wavenumber and, as is seen from expressions (26) and (51), the growth rate γ_{NLs}, to within a factor on the order of unity, passes over to the linear growth rate γ_s of the homogeneous slow vortex turbulence. From expression (51) we also see that the nonlinear excitation rate of the slow vortex is proportional to the cube root of the electron-to-ion mass ratio, $\gamma_{NLs} \propto (m_e/m_i)^{1/3}$, as is the case with γ_s.

10. EXCITATION OF A NONLINEAR FAST VORTEX

When the radial nonuniformity of the electron gyrofrequency ω_{He} is ignored, the rate of excitation of a fast vortex perturbation and the electron term in the dispersion relation both vanish. In this case, the linear ion contribution is to be taken into account even in the equation for a steady-state fast vortex. However, in the steady-state approximation, we ignore the radial nonuniformity of ω_{He}. As will be clear later, the vortex is only excited at the expense of the radial nonuniformity of the electron gyrofrequency.

In the steady-state case, from Eqs. (42) and (44) we obtain the equations

$$[(V_{\theta 0} - V_{\theta q})\boldsymbol{\nabla}_\theta + e/(m_e\omega_{He})\{\phi, \}_{r,\theta}] \times (\Delta_\perp\phi + q_i\delta n_i 4\pi) \approx 0, \quad (52)$$

$$\{\phi, \}_{r,\theta} = r^{-1}[(\partial_r\phi)\partial_\theta - (\partial_\theta\phi)\partial_r], \quad (\boldsymbol{\nabla}_{\theta q})^2\delta n_i \approx n_{0i}(q_i/m_i)\Delta_\perp\phi, \quad (53)$$

which can be reduced to the equation

$$[(V_{\theta 0} - V_{\theta q})\boldsymbol{\nabla}_\theta + e/(m_e\omega_{He})\{\phi, \}_{r,\theta}] \times [(V_{\theta q}\boldsymbol{\nabla}_\theta)^2 + \omega_{pi}^2]\Delta_\perp\phi \approx 0. \quad (54)$$

Recall that, in the steady-state linear approximation, the following relationships are valid: $V_{\theta q} \approx V_{\theta 0}$ and $(V_{\theta q}\boldsymbol{\nabla}_\theta)^2\phi \approx -\omega_{pi}^2\phi$. However, in the nonlinear case (i.e., when nonlinearities are taken into account), these relationships are satisfied only approximately.

Let us now describe the excitation of a fast vortex. To do this, we take into account the time-dependent term with ∂_τ in Eq. (44) and the radial nonuniformity of ω_{He}. As a result, we arrive at the equation

$$\partial_\tau\Delta_\perp\phi + 4\pi q_i\partial_\tau\delta n_i \approx (\boldsymbol{\nabla}_\theta\phi)\omega_{pe}^2\partial_r(1/\omega_{He}). \quad (55)$$

Since higher order terms in Eq. (54) satisfy the relationship $(V_{\theta q}\nabla_\theta)^2\phi \approx -\omega_{pi}^2\phi$, from Eqs. (42) and (55) we obtain the approximate equation

$$\partial_\tau^2\Delta\phi \approx (\omega_{pi}^2/2V_{\theta q})\phi\omega_{pe}^2\partial_r(1/\omega_{He}), \quad (56)$$

which describes the excitation of a fast vortex. We introduce the nonlinear wavenumber through the relationship $\Delta\phi \equiv -\kappa_{NL}^2\phi$. The nonlinear wavenumber κ_{NL} so introduced is determined by the radial and angular sizes of the vortex. Using Eq. (56), we obtain the following estimate for the nonlinear rate of excitation of a fast vortex:

$$\gamma_{NL}^{(q)} \approx (\omega_{pe}/\kappa_{NL})[(\omega_{pi}^2/2V_{\theta 0})\partial_r(1/\omega_{He})]^{1/2}. \quad (57)$$

A comparison of expression (57) with the last of expressions (23) shows that the growth rate $\gamma_{NL}^{(q)}$ is proportional to the linear growth rate of the homogeneous fast vortex turbulence. From expression (57), we also see that the vortex is excited by the radial gradient of ω_{He}. In the linear approximation in which the equality $\omega_{pi}/V_{\theta 0} = k_\theta$ is satisfied, the nonlinear wavenumber κ_{NL} is the linear wavenumber k and the nonlinear growth rate $\gamma_{NL}^{(q)}$ passes over to linear growth rate (23).

11. SATURATION OF THE EXCITED HOMOGENEOUS VORTEX TURBULENCE

In a homogeneous plasma, the instability appears as the bunching of uniformly distributed electrons. The instability stops growing (i.e., the bunching process terminates) when the electrons evolve into a slow (adiabatic) dynamic stage, in which the frequency Ω_{tr} of the oscillations of the electrons within the vortex (i.e., the electrons trapped by the vortex) exceeds the instability growth rate, $\Omega_{tr} > \gamma$. If the vortex continue to grow and, accordingly, continue to trap more and more electrons, then the equally dense layers of electrons with $V_\theta > V_{ph}$ and with $V_\theta < V_{ph}$ in the vicinity of the vortex boundary would mix to form a ring-shaped layer of the same density near the vortex boundary. Hence, the condition for saturation of the plasma instability against the excitation of homogeneous vortex turbulence has the form

$$\Omega_{tr} \geq \gamma. \quad (58)$$

Using formulas (23), (31), (33), and (58), we can show that the instability saturates when the electric potential ϕ_0 of the fast vortex increases to

$$\phi_{sat} \approx (m_e/e)[\omega_{He}\omega_{pi}/(l_\theta k^2)](2n_{0e}/N_e). \quad (59)$$

Hence, the amplitudes ϕ_0 of the vortex perturbations of the homogeneous plasma turbulence cannot exceed the saturation amplitude ϕ_{sat}. However, in a sequence of widely spaced individual vortices, the amplitudes of the vortex perturbations can continue to increase above the saturation amplitude because the electrons in vortices with $\phi_0 > \phi_{sat}$ can exhibit nonadiabatic dynamic behavior.

Let us compare the saturation amplitude ϕ_{saq} with the maximum possible amplitude ϕ_{sm} of the vortices in such a sequence. The amplitude ϕ_{sm} is determined by the condition that the magnetic force no longer keeps the electrons of a vortex in closed orbits around the vortex axis, so that the electrons can move across the magnetic field. In other words, an electron-bunch vortex can expand across the magnetic field. This indicates that the electron bunching process terminates. Thus, from the condition

$$m_e V_\theta^2/r - eE_r \geq m_e\omega_{He}V_\theta, \quad (60)$$

which indicates that the forces keeping the electrons in closed trajectories cease to be in balance, we can determine the maximum possible saturation amplitude ϕ_{sm} of the vortex. In condition (60), E_r is the electric field of the vortex, δn_{ev} is the perturbed electron density in the vortex, and V_θ is the azimuthal electron velocity in the vortex. This condition implies that, under the inequality

$$\omega_{pe}^2(\delta n_{ev} + N_e)/n_{0e} \geq \omega_{He}^2/2 \quad (61)$$

the electrons can move freely across the magnetic field and, accordingly, the vortex can expand freely across the field. As a result, using Poisson's equation (3), we arrive at the following expression for the saturation amplitude of the vortex:

$$\phi_{sm} \approx m_e/(ek^2)[\omega_{He}^2/2 - (N_e/n_{0e})\omega_{pe}^2]. \quad (62)$$

The saturation amplitude close to that given by expression (62) was obtained in [2]. From this expression we can see that, if the ion beam is overneutralized by the electrons nearly to the maximum possible extent, i.e., if

$$N_e \approx H_0^2/(8\pi m_e c^2), \quad (63)$$

then no vortex perturbations are excited within the plasma lens.

We now compare the saturation amplitude ϕ_{sat} of the instability of a plasma against the excitation of a homogeneous vortex turbulence with the amplitude ϕ_{sm} in the case when the extent to which the beam is overneutralized, N_e/n_{0e}, is far from maximal:

$$\phi_{sat}/\phi_{sm} \approx (4/l_\theta)(n_{0e}/N_e)(\omega_{pi}/\omega_{He}). \quad (64)$$

It can be seen from expression (64) that the inequality $\phi_{sat} \ll \phi_{sm}$ is satisfied for heavy ions and for strong magnetic fields. Consequently, there is an ample margin in the vortex amplitude with respect to the breaking of the growing homogeneous vortex turbulence into individual vortices.

12. CONCLUSIONS

We have theoretically investigated the excitation of vortices in a plasma lens for focusing high-current ion beams. It is shown that any perturbation of the density of electrons in a lens sets them into vortex motion. There are two types of vortex perturbations that can be excited on ion time scales in a plasma lens. These are fast perturbations whose phase velocities V_{ph} are close to the azimuthal electron drift velocity in the crossed radial focusing electric and longitudinal magnetic fields, $V_{ph} \approx V_{\theta 0}$, and slow perturbations with $V_{ph} \ll V_{\theta 0}$. The instability of a plasma against the excitation of homogeneous vortex turbulence saturates at a low level when the frequency of oscillations of electrons in closed orbits within a growing vortex becomes higher than the instability growth rate. At large amplitudes, a sequence of spatially separated nonlinear vortices is excited. The nonlinear growth rates are proportional to the linear growth rates of the instability of a plasma against the excitation of homogeneous vortex turbulence and depend on the amplitudes of the vortices.

Since the instability develops in an initially homogeneous plasma, the vortices are excited in pairs, namely, an electron bunch is excited simultaneously with a neighboring electron cavity.

Such behavior of electrons was observed in experiments with a purely electron plasma [4–6], with a charged plasma in a lens [2, 8], and with a plasma in crossed radial electric and longitudinal magnetic fields [10].

ACKNOWLEDGMENTS

This work was supported in part by the Science and Technology Center in Ukraine, project no. 1596.

REFERENCES

1. A. Goncharov, A. Dobrovolskiy, I. Protsenko, and A. Zataugan, IEEE Trans. Plasma Sci. **21**, 573 (1993).
2. A. A. Goncharov, A. N. Dobrovol'skiĭ, A. N. Kotsarenko, *et al.*, Fiz. Plazmy **20**, 499 (1994) [Plasma Phys. Rep. **20**, 449 (1994)].
3. A. A. Goncharov, S. N. Gubarev, V. I. Maslov, and I. N. Onishchenko, in *Problems of Atomic Science and Technology* (Kharkov, 2001), Vol. 3, p. 1524.
4. D. A. Schecter and D. H. E. Dubin, Phys. Rev. Lett. **83**, 2191 (1999).
5. Y. Kiwamoto, K. Ito, A. Sanprei, and A. Mohri, Phys. Rev. Lett. **85**, 3173 (2000).
6. K. S. Fine, A. C. Cass, W. G. Flynn, and C. F. Driscoll, Phys. Rev. Lett. **75**, 3277 (1995).
7. A. Kabantsev, C. F. Driscoll, D. H. E. Dubin, and D. Schecter, in *Proceedings of the 11th International Toki Conference on Plasma Physics, Toki, 2000*.
8. A. Goncharov and I. Litovko, IEEE Trans. Plasma Sci. **27**, 1073 (1999).
9. N. A. Keralishvili, Zh. Tekh. Fiz. **60** (2), 78 (1990) [Sov. Phys. Tech. Phys. **35**, 182 (1990)].
10. M. Kono and M. Y. Tanaka, Phys. Rev. Lett. **84**, 4369 (2000).
11. V. I. Petviashvili and O. A. Pokhotelov, Fiz. Plazmy **12**, 1127 (1986) [Sov. J. Plasma Phys. **12**, 651 (1986)].
12. M. V. Nezlin and G. P. Chernikov, Fiz. Plazmy **21**, 975 (1995) [Plasma Phys. Rep. **21**, 922 (1995)].
13. V. D. Larichev and G. M. Reznik, Dokl. Akad. Nauk SSSR **321**, 1077 (1976).

Translated by I.A. Kalabalyk

Plasma Physics Reports, Vol. 30, No. 8, 2004, pp. 671–686. Translated from Fizika Plazmy, Vol. 30, No. 8, 2004, pp. 722–738.

PLASMA KINETICS

Nonequilibrium Electron Distribution Functions in a Semiconductor Plasma Irradiated with Fast Ions

S. I. Kononenko[1], V. M. Balebanov[2], V. P. Zhurenko[1], O. V. Kalantar'yan[1], V. I. Karas'[3], V. T. Kolesnik[1], V. I. Muratov[1], V. E. Novikov[4], I. F. Potapenko[5], and R. Z. Sagdeev[6]

[1] *Kharkov National University, pl. Svobody 4, Kharkov, 61077 Ukraine*

[2] *Institute for Space Research, Russian Academy of Sciences, Profsoyuznaya ul. 84/32, Moscow, 117810 Russia*

[3] *National Science Center, Kharkov Institute for Physics and Technology, ul. Akademicheskaya 1, Kharkov, 61108 Ukraine*

[4] *Science and Technology Center of Electrophysical Treatment, National Academy of Sciences of Ukraine, Kharkov, Ukraine*

[5] *Keldysh Institute of Applied Mathematics, Russian Academy of Sciences, Miusskaya pl. 4, Moscow, 125047 Russia*

[6] *University of Maryland, College Park, MD, USA*

Received October 21, 2003

Abstract—A kinetic equation for the electrons scattered by acoustic phonons in a solid is derived, and relationships between power-law asymptotic solutions and the particle and energy fluxes in phase space are established. The dependence of the nonextensivity parameter on the intensity of the particle flow in phase space is determined for a nonequilibrium solid-state plasma with sources and sinks. The formation of a steady-state nonequilibrium electron distribution function in a semiconductor with a source and a sink in phase space is numerically simulated using the Landau and Fokker–Planck collision integrals. The nonequilibrium electron distributions formed in the solid-state plasmas of semiconductors and of a Sb/Cs cathode are studied experimentally. It is shown that, within the electron energy range of 5–100 eV, the electron distribution functions decrease with energy according to a power law. © *2004 MAIK "Nauka/Interperiodica".*

1. INTRODUCTION

At present, the development of high-power particle and radiation sources is stimulating great interest in the properties of nonequilibrium systems. The presence of sources and sinks in momentum space can lead to the formation of nonequilibrium particle distribution functions with power-law tails even in spatially uniform systems. The inapplicability of the local equilibrium approximation to such situations is related to the presence of particle flows in phase space. In the second section of this paper, the asymptotic properties of such nonequilibrium states are studied, their relation to the nonextensive Tsallis' thermodynamics is established, and the dependence of the nonextensivity parameter on the intensity of the particle flow in phase space (i.e., on the intensities of sources and sinks) is determined.

The third section is devoted to numerical simulations of the formation of a steady-state nonequilibrium distribution of particles with a long-range repulsion potential. The collisional dynamics of such a system is studied using spatially uniform nonlinear Landau and Fokker–Planck collision integrals, which are model representations of the Boltzmann collision integral. In numerical simulations, completely conservative difference schemes are used.

In the fourth section, we consider the conduction and emission properties of a semiconductor plasma irradiated with intense particle or laser beams.

In the fifth section, the formation of nonequilibrium electron distribution functions (EDFs) in the plasmas of semiconductors and of a Sb/CS cathode is studied experimentally. To study these functions, the method of the secondary electron emission induced by fast low-Z ions was employed. The formed EDFs are measured, the coefficients of the secondary ion-induced electron emission are determined, and their relationship to the source power in the ion's track is found.

2. STEADY NONEQUILIBRIUM STATES OF SYSTEMS WITH STATIONARY PARTICLE FLOWS IN PHASE SPACE

Quasi-steady nonequilibrium states of particle systems can be studied by solving kinetic equations with allowance for sources and sinks. Power-law particle energy distributions were first predicted theoretically in [1–4] and then observed experimentally in [5, 6]. In [1, 2], it was shown using a similarity transformation that the kinetic Boltzmann equation for a spatially uniform system has exact stationary power-law solutions. In [3, 4], it was shown by directly calculating the Boltzmann and Landau collision integrals in kinetic equations that the power-law distributions of the form

$$F(E) = AE^{-s}, \tag{1}$$

where s is an exponent and A is a constant, are stationary solutions for which particle (or energy) fluxes in

1063-780X/04/3008-0671$26.00 © 2004 MAIK "Nauka/Interperiodica"

phase space are nonzero constants. These particle states are similar to turbulent Kolmogorov spectra of waves and depend only on the integral characteristics of the source and sink [4].

In particular, nonequilibrium spatially uniform systems with a component obeying a power-law distribution include electron subsystems of semiconductors exposed to radiation with a photon energy on the order of the width of the forbidden zone [7] or electron subsystems in metals that undergo ionization caused by α particles propagating in them [5].

In [1–4], the exponent s of power-law solutions to the kinetic Boltzmann equation depended only on the degree of homogeneity of the particle interaction potential. In those papers, both the dispersion properties of a plasma with a power-law electron distribution and the ionization equilibrium in such nonequilibrium steady states were studied. In [8, 9], it was shown that plasma oscillations with a linear dispersion can exist in a plasma with two components of the distribution function, equilibrium and nonequilibrium. These plasma oscillations could be of importance for many interactions in semiconductor plasma, in particular, for the plasmon mechanism of superconductivity [10].

2.1. Basic Equations

It is of interest to examine the cases in which the effect of a source on the deviation of the distribution function from equilibrium can be clearly traced.

Exact solutions to the Boltzmann equation for a spatially uniform gas were first obtained in [11] within a special collisional model (a gas of Maxwellian molecules) for the relaxation to a thermodynamic equilibrium. The generalization to a nonequilibrium case was performed in [12]. Note that the method described in [11] was generalized to a wide class of power-law intermolecular potentials [13].

One can construct mathematical models for the collision integral in kinetic equations so that these equations, on one hand, become more appropriate for analysis and, on the other hand, still possess some of their important properties inherent to complete nonlinear equations, such as conservation laws and the H theorem [11, 14].

In this paper, we investigate the features of steady-state nonequilibrium particle distributions in systems with sources and sinks by the example of the interactions of electrons with phonons in a solid-state plasma. Main attention is paid to the evolution of such states with changes in the parameters of nonequilibrium (particle fluxes) in a system, rather than their time evolution.

To describe electron kinetics, we use a spatially uniform nonlinear (because of the incorporation of quantum statistics) kinetic equation with sources and sinks [15]:

$$\frac{\partial f}{\partial t} = -\frac{1}{4\pi v^2}\frac{\partial}{\partial v}\Pi\{f, v\} + \Psi(v). \quad (2)$$

In the case of an isotropic medium, it is convenient to change the variables: $\varepsilon = v^2/2$ and $F(\varepsilon) = 4\pi\sqrt{2\varepsilon}\,f(\sqrt{2\varepsilon})$, where v is the particle velocity normalized to the mean particle velocity v_{0T} in the initial state.

Let us consider an important class of sources that are localized in energy space, $S_+(\varepsilon) = Q_i\varepsilon_i\delta(\varepsilon - \varepsilon_i)$. The sinks are often written in the form $S_-(\varepsilon) = \nu(\varepsilon)F(\varepsilon)$. Using these model representations, the expression describing the sources and sinks can be written as

$$\Psi(\varepsilon) = S_+(\varepsilon) - S_-(\varepsilon). \quad (3)$$

For charged particles interacting with phonons, the expression for the particle flux in the kinetic equation takes a simple form,

$$\Pi(\{f\}, v) = D(v)\frac{\partial f}{\partial v} + F(v)f(v)(1 - f(v)), \quad (4)$$

where the diffusion coefficient $D(v)$ and the drag force $F(v)$ for a particle moving in phase space are power-law functions of the electron energy (the corresponding expressions for some particular cases are given in [16]). Within the region where the flux P is constant, the equation for the steady-state distribution function (for the above type of interaction) is

$$T_0\frac{\partial f}{\partial \varepsilon} + f - f^2 = \frac{P}{\varepsilon^2}, \quad (5)$$

where $T_0(\varepsilon) = \dfrac{D(\varepsilon)}{F(\varepsilon)}$. After substituting $f(\varepsilon) = -\dfrac{T_0}{y(\varepsilon)}\dfrac{dy(\varepsilon)}{d\varepsilon}$, this equation converts into the second-order linear equation

$$T_0^2\frac{d^2y(\varepsilon)}{d\varepsilon^2} + T_0\frac{dy(\varepsilon)}{d\varepsilon} + \frac{P}{\varepsilon^2}y(\varepsilon) = 0. \quad (6)$$

2.2. Solutions to Eq. (6)

A general solution to Eq. (6) is

$$y(\varepsilon) = C_1 I_\chi\left(\frac{\varepsilon}{2T_0}\right) + C_2 K_\chi\left(\frac{\varepsilon}{2T_0}\right), \quad \chi = \sqrt{\frac{1}{4} - \frac{P}{T_0^2}}, \quad (7)$$

where $I_\chi(z)$ and $K_\chi(z)$ are the modified Bessel function of the first and second kinds, respectively. The integration constants are determined from the matching condition for solution (7) and the equilibrium solution in the regions beyond the inertial interval.

To clarify the effect of the degree to which the system is nonequilibrium (the source intensity) on the shape of the EDF in a solid, we present the results from the numerical solution of the kinetic equation for several P values.

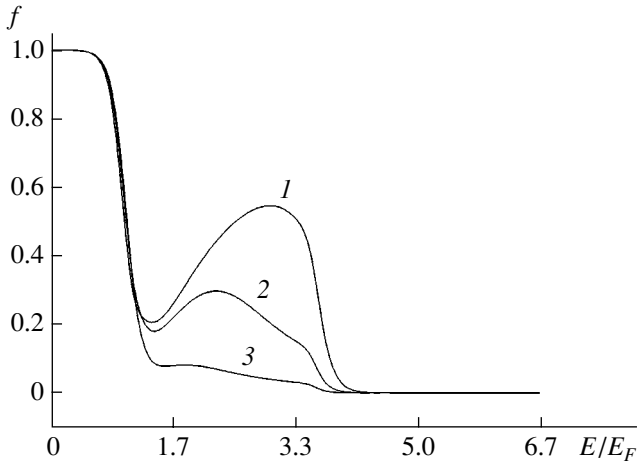

Fig. 1. Distribution functions of the electrons scattered by acoustic phonons at $T = 0.1E_F$ for P = (*1*) –0.81, (*2*) –0.4, and (*3*) –0.1.

The solutions to the kinetic equation for the case of electron scattering by the phonons with a temperature of $T_0 = 0.1E_F$ (where E_F is the Fermi energy) are shown in Fig. 1. It can be seen that the nonequilibrium part of the distribution function increases with source intensity.

The time evolution of the EDF is illustrated in Figs. 2–4. Figures 2 and 3 show how the distribution function and the particle flux in phase space relax to their steady-state values in the presence of sources and sinks. It can be seen from Fig. 3 that phase space regions with a quasi-constant energy flux eventually form. It follows from Figs. 3 and 4 that, in the region where the flux is constant, quasi-power-law zones arise in the distribution function. The regions with zero flux (see Figs. 2, 4) correspond to the equilibrium Fermi function.

In the region where the EDF is nonequilibrium, it is well approximated by power-law functions with an exponent that varies only slightly with increasing source intensity. This is clearly seen in Fig. 4, which shows a steady-state EDF between the source and sink on a double logarithmic scale.

2.3. Tsallis' Nonextensive Thermodynamics

As was mentioned above, steady-state nonequilibrium distributions (SND) of particles in phase space play the same role in spatially uniform systems as Maxwellian distributions in Gibbs' thermodynamics. The presence of such great deviations from the exponential dependence should significantly change the thermodynamic properties of a system.

Note that, over the last fifteen years, great progress has been achieved in the thermodynamics of strongly nonequilibrium systems; the results obtained indicate the existence of non-Gibbs (power-law) distributions in such systems. Let us briefly outline the results that will be needed further for our analysis.

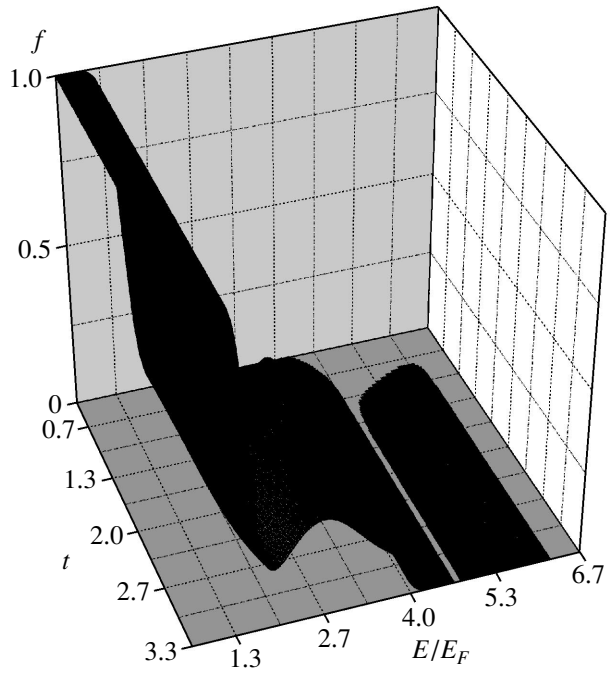

Fig. 2. Distribution function as a function of time and energy for P = –0.4.

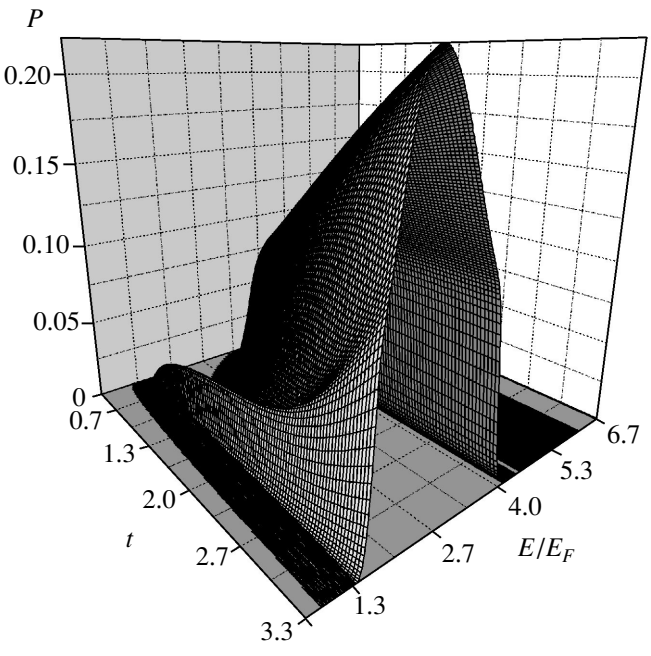

Fig. 3. Particle flux in phase space as a function of time and electron energy for P = –0.4.

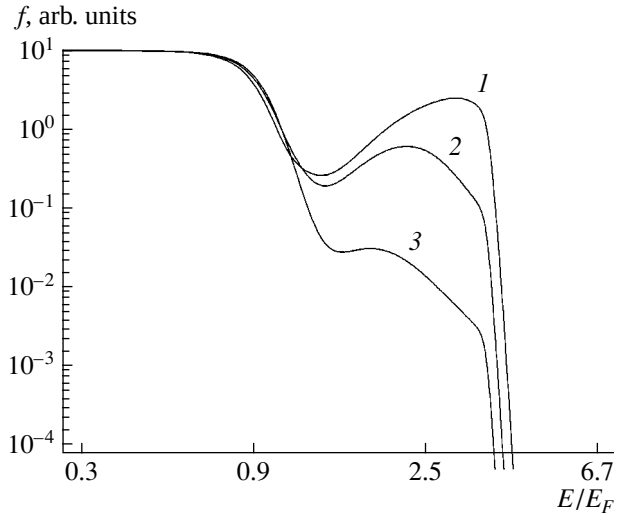

Fig. 4. Distribution functions for $P = (1) -0.81$, $(2) -0.4$, and $(3) -0.1$.

In 1988, K. Tsallis [17] attempted to extend the applicability range of thermodynamics and statistic mechanics to systems in which entropy does not possess the property of extensivity [17].

It is well known that, in conventional thermodynamics, the equilibrium state corresponds to the maximum possible entropy at a given energy, volume, etc. In addition, it is assumed that entropy is an extensive quantity. This assumption immediately leads to some important consequences.

Let us recall the definition of an extensive quantity. Let the system consists of two *independent* subsystems *A* and *B*. Entropy is an extensive quantity if the entropy of the entire system is equal to the sum of the subsystem entropies:

$$S(A + B) = S(A) + S(B).$$

In statistical physics, entropy is treated via the number of system microstates. In trying to define entropy so that it is an extensive quantity, statistical physics has to invoke a hypothesis of molecular chaos. This hypothesis assumes that, *before a collision*, any colliding molecules be definitely uncorrelated, i.e., not affecting one another. For many (but not for all) systems, this is a quite reasonable assumption. It is from this assumption that the Boltzmann expression for the entropy of a closed system follows:

$$S = -\sum_i p_i \ln(p_i),$$

where i is the number of the system microstate, p_i is the probability that the system is in this microstate, and the summation is performed over all microstates.

After [17], a great number of systems were studied in which the extensivity of entropy and the Boltzmann thermodynamics were violated. Examples of such systems are a cold interstellar dust cloud of sufficiently large size and a system of colliding high-energy hadrons whose interaction is characterized by strong correlations. There are other systems that cannot be described by Boltzmann thermodynamics. The reasons why Boltzmann thermodynamics is inapplicable are quite different [17]. These could be "memory effects," due to which the current state of the system depends not only on the values of the system parameters at a given instant but also on the values they had some time ago.

Memory effects can easily violate the hypothesis of molecular chaos. These effects imply that, before a collision, individual particles "remember" one another, so that their motion is not completely uncorrelated. Hence, thermodynamic relations must be refined with allowance for additional correlations. An attempt at such a refinement was made by Tsallis [17]. In his thermodynamics, the logarithmic and exponential functions in the conventional expressions for entropy and distribution function were formally replaced with expressions containing power-law functions:

$$\ln(x) \longrightarrow \ln_q(x) = \frac{x^{1-q} - 1}{1 - q},$$

$$\exp(x) \longrightarrow \exp_q(x) = (1 + (1 - q)x)^{1/(1-q)}$$

with a certain numerical parameter q. Note that, as q tends to unity, $\ln_q(x)$ and $\exp_q(x)$ transform into the ordinary logarithmic and exponential functions (this can easily be checked, e.g., by their differentiation). A new formula for entropy is

$$S_q = -\sum_i p_i^q \ln_q(p_i) = \frac{1 - \sum_i p_i^q}{q - 1}. \qquad (8)$$

As $q \longrightarrow 1$, the q-entropy converts into the conventional Boltzmann entropy.

The main consequence of such a substitution is that q-entropy is no longer an extensive function. When the system is divided into two independent subsystems, *A* and *B*, we obtain

$$S_q(A + B) = S_q(A) + S_q(B) + (1 - q)S_q(A)S_q(B).$$

Thus, the parameter q is a measure of system nonextensivity. We note that, generally, the parameter q is not in any way limited and can take any value from $-\infty$ to $+\infty$; certain restrictions can, however, be imposed in solving one or another specific problem.

In [18], it was shown that the condition for the q-entropy to be at maximum leads to power-law functions

$$p(E) = \exp_q(-(E/T)). \qquad (9)$$

The above functional form of the q-entropy was chosen rather arbitrarily, and its main importance is as a model description of nonextensivity.

Thus, there is a set of different thermodynamics. Indeed, for $q = 1$, the above general approach results in conventional thermodynamics. If q is not equal to unity, then the physical situation is qualitatively different from equilibrium thermodynamics.

2.4. Features of the Electron Kinetics in Semiconductor Plasma at Energies Higher than the Fermi Energy

In studying the relaxation of high-energy electrons in semiconductor plasma, it is best to use a kinetic equation in the form of a nonlinear Fokker–Planck equation with a Landau collision integral. Below, we use dimensionless variables: the velocity is in units of the thermal velocity and time in units of the electron–electron relaxation time τ_{ee}, which, in the case of Coulomb interaction, is equal to $\tau_{ee} = \dfrac{v_T^3 m^2}{4\pi n_p e^4 \ln\Lambda}$, where $\ln\Lambda$ is the Coulomb logarithm. The dimensionless EDF $f(v, t)$ is normalized so that $n_p = \int_0^\infty f(v,t)v^2 dv = 1$ and $E = \int_0^\infty f(v,t)v^4 dv = \dfrac{3}{2}T = 1$, where T is the electron temperature in energy units.

At high source intensities, the relaxation of the particle flow between collisions should be taken into account. For this reason, it is necessary to move from the conventional representation of the Fokker–Planck equation in the form of a parabolic equation to a set of equations of hyperbolic type:

$$\begin{aligned} \frac{\partial f}{\partial t} &= I_{nlFP}[f, f] + \Psi(v), \\ I_{nlFP}[f, f] &= -\frac{1}{4\pi v^2}\frac{\partial}{\partial v}J_{nl}\{f, v\}, \\ \tau\frac{\partial J_{nl}}{\partial t} + J_{nl} &= \Pi_{nl}(v, \{f(v)\}). \end{aligned} \tag{10}$$

To simplify analysis, we reduce the expression for the particle flux to a symmetric form [23],

$$\begin{aligned} &\Pi_{nl}(v, \{f(v)\}) \\ &= -\frac{4\pi}{v}\frac{\partial}{\partial v}\int_0^v [f(v)P(x) - f(x)P(v)]x^2 dx, \\ &P(v) = 2\int_v^\infty f(x)x dx. \end{aligned} \tag{11}$$

The calculation of flux (12) in velocity space for a power-law EDF described by Eqs. (10) yields the following expression:

$$\begin{aligned} \Pi(v, q) &= A\Big(C_{22}F_1\Big(\frac{3}{2}, \frac{1}{q-1}; \frac{5}{2}; -(q-1)v^2\Big) \\ &- 3\Big(5C_1 - C_2\exp_q(v^2)_2F_1\Big(\frac{5}{2}, \frac{1}{q-1}; \\ &\frac{7}{2}; -(q-1)v^2\Big)\Big)\Big), \end{aligned} \tag{12}$$

with the constants

$$\begin{aligned} C_1 &= v^{\frac{2}{q-1}} + 2(q-1)v^{\frac{2q}{q-1}} + (q-1)^2 v^{2+\frac{2q}{q-1}} \\ &- \Big(\frac{1}{q-1}\Big)^{\frac{1-2q}{q-1}}\Big(1 + \frac{1}{(q-1)v^2}\Big)^{\frac{1}{1-q}} \\ &\times\Big(\Big((q-1)^{-\frac{q}{q-1}} + (q-1)^{-\frac{1}{q-1}}v^2\Big)\Big)^2, \\ A &= \frac{(q-1)^2 v^{\frac{q-3}{q-1}}(1 + (q-1)v^2)^{\frac{1+q}{1-q}}\Gamma\Big(\frac{1}{q-1}\Big)\Gamma\Big(\frac{2-q}{q-1}\Big)}{15\pi^3\Gamma^2\Big(\frac{5-3q}{2q-2}\Big)}, \\ C_2 &= 2(q-1)v^{2+\frac{2q}{q-1}}\exp_q(v^2). \end{aligned} \tag{13}$$

This function, which represents a surface in (v, q) space, is shown in Fig. 5. The steady-state states correspond to regions in which the flux does not depend on velocity. Two such regions are seen in Fig. 5. The first is the region with $q = 1$, which corresponds to an equilibrium Maxwellian solution, while the second corresponds to states with power-law asymptotes obtained in [3–5].

The hyperbolic character of the set of equations allows one to efficiently use the method of straight lines to numerically analyze the system evolution. The dependence of the EDF on velocity (or energy) is represented by its values at discrete points. The time evolution of the EDF values at these points can easily be described by the set of nonlinear ordinary differential (over time) equations.

Note that, in the case of quantum statistics, the formal generalization of an equilibrium Maxwell–Gibbs distribution function with the use of function (12) to nonequilibrium states is ambiguous. Indeed, an equilib-

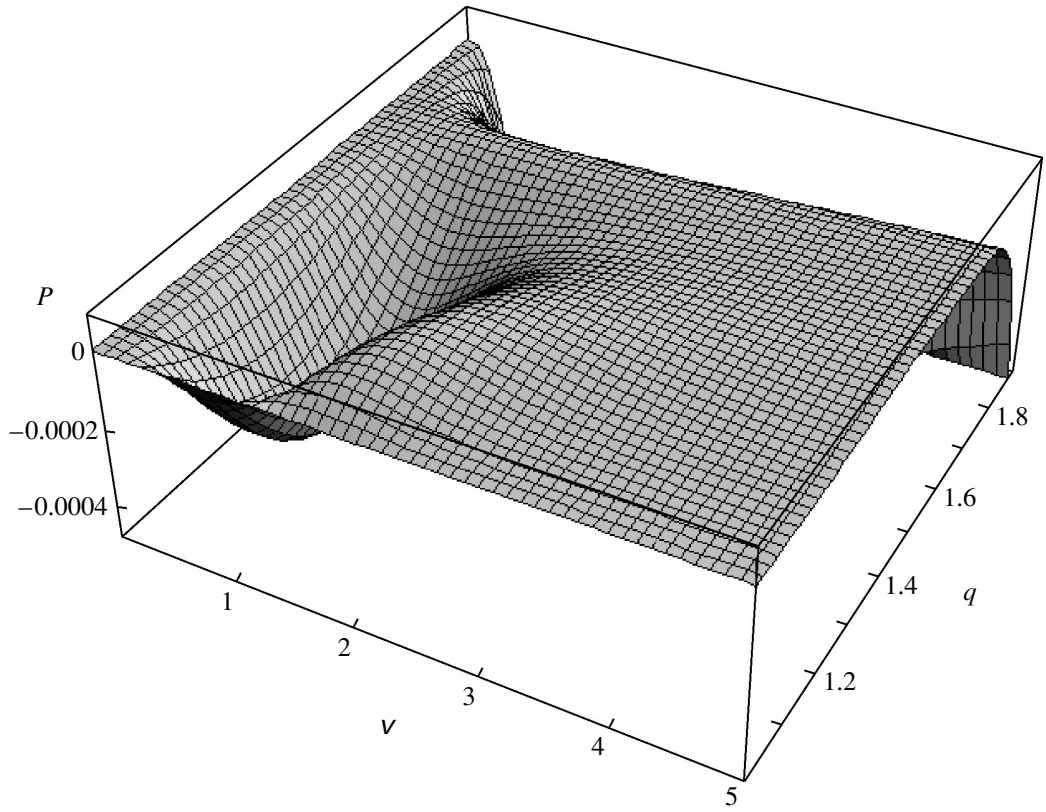

Fig. 5. Particle flux in phase space vs. velocity and nonextensivity parameter q.

rium Fermi function can be represented in two equivalent forms:

$$f(\varepsilon) = \frac{1}{1 + \exp\left(\frac{\varepsilon - E_F}{T}\right)} = \frac{\exp\left(-\frac{\varepsilon - E_F}{2T}\right)}{\exp\left(\frac{\varepsilon - E_F}{2T}\right) + \exp\left(-\frac{\varepsilon - E_F}{2T}\right)}. \quad (14)$$

Substituting function $\exp_q(x)$ for the exponential function in these expressions, we obtain two nonequivalent generalizations to nonequilibrium states for a Fermi function. At $q \longrightarrow 1$, both these functions convert into a Fermi distribution function. However, when deviating from equilibrium, variations in the distribution function

$$f_q(\varepsilon) = \frac{\exp_q\left(-\frac{\varepsilon - E_F}{2T}\right)}{\exp_q\left(\frac{\varepsilon - E_F}{2T}\right) + \exp_q\left(-\frac{\varepsilon - E_F}{2T}\right)} \quad (15)$$

occur mainly in the region near the Fermi energy, while the second function

$$f_q(\varepsilon) = \frac{1}{1 + \exp_q\left(\frac{\varepsilon - E_F}{T}\right)} \quad (16)$$

acquires a power-law asymptote at high energies. One can prove that distribution function (15) is a good approximation for the EDF formed in the interactions with phonons, while distribution function (16) adequately describes steady-state nonequilibrium solutions to a kinetic equation with a Landau collision integral with allowance for corrections related to the Fermi statistics.

So far, we have considered the formation of an SND with sources and sinks localized in momentum space. It should be noted that one often has to deal with systems in which both the source and the sink are nonlocalized. In particular, wake ionization is a source that is not localized in momentum (energy) space. Moreover, the source intensity is often insufficient to provide a universal nonequilibrium distribution throughout the interval between the source and sink (see [19, 20]). In these cases, it is necessary to resort to numerical simulations.

3. NUMERICAL SIMULATIONS OF THE FORMATION OF STEADY-STATE NONEQUILIBRIUM PARTICLE DISTRIBUTIONS

A specific feature of systems of particles interacting via the Coulomb potential is that the scattering cross section increases without bound as the momentum transferred tends to zero. For gaseous and semiconductor plasmas with a large Coulomb logarithm ($\ln\Lambda = 10$–15), one can restrict oneself to the expansion of the integrand in the collision integral in small momenta transferred (a diffusion approximation) and to represent the collision integral in the Landau or Fokker–Planck form [21, 22], which are model representations of the Boltzmann collision integral. In this model [23–25], the moments of the exact and model collision integrals coincide up to the third-order tensor moment and the forth-order scalar moment. Conservation laws for energy and the number of particles, as well as the Boltzmann *H* theorem, are valid. The model collision integral provides a correct representation of the equations for the twenty-moment Grad approximation. Finally, the exact solution to the Landau equation for Maxwellian molecules ($\beta = 4$) is the exact solution to the Boltzmann equation. Below, we will consider long-range potentials ($U \propto r^{-\beta}$, with $1 \le \beta \le 4$, where r is the distance between the interacting particles), for which a local nonequilibrium particle distribution can form (see [3]). Note that the dynamics of particles interacting via the Coulomb repulsion potential ($\beta = 1$) can be considered using kinetic equations in either the Landau or Fokker–Planck form.

3.1. Formulation of the Problem

In the case of an isotropic distribution function $f(v, t)$, the Landau collision integral is

$$\frac{\partial f}{\partial t} = I_L[f, f] = \frac{\Gamma}{v^2}\frac{\partial}{\partial v}\left\{\frac{1}{v}\int_0^\infty dw Q(v, w) \times\left[wf(w)\frac{\partial f(v)}{\partial v} - vf(v)\frac{\partial f(w)}{dw}\right]\right\}, \quad (17)$$

$$Q(v, w) = \frac{a(v, w)(v + w)^{\eta+4} + b(v, w)|v - w|^{\eta+4}}{(\eta + 2)(\eta + 6)},$$

$$0 \le v, \quad w < \infty, \quad t \ge 0,$$

$$a(v, w) = [vw - (v^2 + w^2)],$$

$$b(v, w) = [vw + (v^2 + w^2)], \quad \eta = (\beta - 4)/\beta,$$

where $\Gamma = 4\pi e^4(\ln\Lambda)/m$ and the symmetric kernel $Q(v, w) = Q(w, v)$ in the case of Coulomb potential has the form $Q(v, w) = -2/3w^3$ for $w \le v$ and $Q(v, w) = -2/3v^3$ for $w \ge v$. The equilibrium solution to Eq. (17) is a Maxwellian distribution function

$$f_{\text{Maxw}} = n\frac{4}{\sqrt{\pi}}v_T^{-3},$$

where $v_T = \sqrt{2k_B/m}$, k_B is the Boltzmann constant, and T is temperature. If there are no sinks (sources), then the number of particles and the system energy do not vary over time:

$$n_p = \int_0^\infty f(v, t)v^2 dv = \text{const},$$

$$E = \int_0^\infty f(v, t)v^4 dv = \frac{3}{2}k_B T = \text{const}.$$

The distribution function $f(v, t)$ is bounded at $v = 0$ and quite rapidly decreases as $t \longrightarrow \infty$. Below, we use dimensionless variables: the velocity in units of the thermal velocity $V_T = \sqrt{3/2}\,v_T$ and time in units of the electron–electron relaxation time τ_{ee}, which is $\tau_{ee} = \dfrac{v_T^3 m^2}{4\pi n_p e^4 \ln\Lambda}$ in the case of Coulomb interaction. The function $f(v, t)$ is normalized so that $n_p = 1$, $E = 1$ and $v_T^2 = 2/3$; consequently, in Eq. (17), the constant Γ is equal to unity.

Note that, when numerically simulating a low-density collisional plasma ($\beta = 1$) under laboratory conditions or for astrophysical applications, the Fokker–Planck collision integral

$$\frac{\partial f}{\partial t} = I_{FP}[f, f] = \frac{1}{v^2}\frac{\partial}{\partial v}\left[A(v)\frac{\partial f}{\partial v} + B(v)f(v, t)\right],$$

$$0 \le v < \infty, \quad t \ge 0,$$

is commonly used in the kinetic equation. For numerical simulations, it is most suitable to represent the Fokker–Planck equation in symmetric form (11).

We consider the formation of a steady-state nonequilibrium solution in the presence of particle or energy flows in velocity space using the above modified versions of the Landau and Fokker–Planck collision integrals in forms (17) and (11), respectively. In this case, the right-hand side of the kinetic equation is added with the terms accounting for the presence of a particle (energy) source (sink):

$$\frac{\partial f}{\partial t} = I_{FP, L}[f, f] + S_+ - S_-. \quad (18)$$

The source (sink) function was modeled by an exponential function with a variable width in momentum

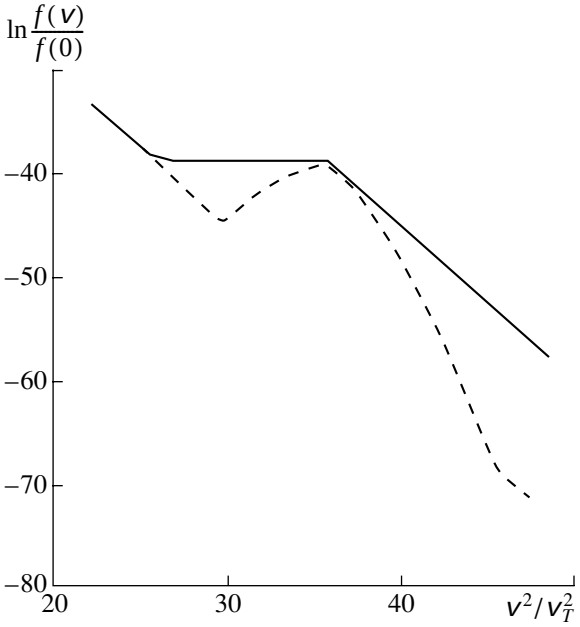

Fig. 6. Distribution functions obtained from the Fokker–Planck equation with a source and a sink of the form $S_\pm \sim I_\pm \exp\{-\alpha_1(v - v_\pm)^2\}$ with $\alpha_1 = 100$, $v_- = 4$, and $v_+ = 7$. The dashed and solid curves refer to the times $t = 25$ and 100, respectively.

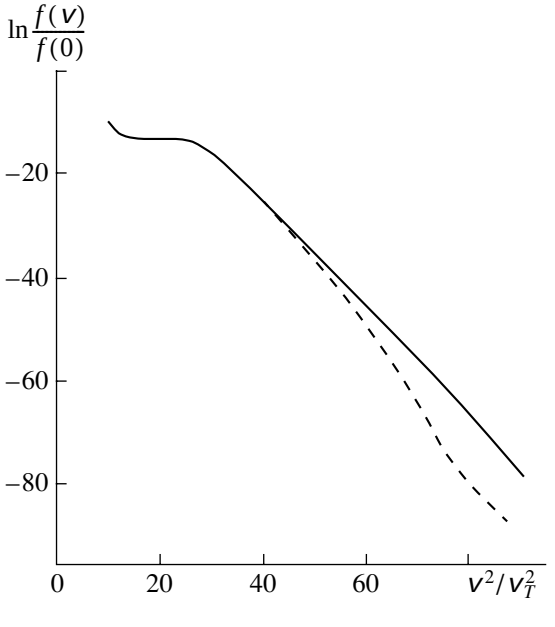

Fig. 7. Distribution functions obtained from the Fokker–Planck equation with a source and a sink of the form $S_\pm \sim I_\pm \exp\{-\alpha_1(v - v_\pm)^2\}$ with $\alpha_1 = 10$, $v_- = 3$, and $v_+ = 5$. The dashed and solid curves refer to the times $t = 25$ and 100, respectively.

space, $S_\pm \sim I_\pm \exp\{-\alpha_1(v - v_\pm)^2\}$; a δ function in the form $S_\pm \sim I_\pm \delta(v - v_\pm)/v^2$; or

$$S_\pm \sim I_\pm \frac{\delta(v - v_\pm)}{v^2} f(v_-, t). \qquad (19)$$

In this case, if $I_+ = I_-$, then an energy flow from the source to sink arises; if $I_+ = I_- \frac{v_-^2}{v_+^2}$, then a particle flow arises. The flow direction is determined by the positions of v_- and v_+. Either a Maxwellian distribution or a δ function was used as an initial distribution. In simulations, we employed a fully conservative implicit difference scheme [23–25], for which discrete analogues of conservation laws hold true and which allow one to perform long-run calculations without error accumulation. An infinite velocity interval was replaced with the maximum interval $10v_T$–$14v_T$, in which the distribution function was set at zero. The initial distribution $\delta(v - v_0)$ was approximated in the following way: the δ function was set at zero for all of the velocities except for one point (usually, $v_0 = 1$).

Since the problem of relaxation is a kind of test, we first consider the Cauchy problem for the initial distribution $f^0(v) = \delta(v - 1)/v^2$. In our calculations, we used the kinetic equation with either the Fokker–Planck or Landau collision integral in form (11) or (17), respectively. When $S_\pm = 0$, these equations are analytically equivalent and, in the limit $t \longrightarrow \infty$, lead to a Maxwellian distribution f_{Maxw}. Let us now discuss the results of numerical simulations.

3.2. Discussion of the Simulation Results

In [23], the formation of a nonequilibrium distribution function was numerically simulated for the kinetic equation with either the Landau or Fokker–Planck collision integral in the presence of energy and particle flows in momentum space that were sustained by a source and a sink. For this purpose, the right-hand sides of kinetic equations (17) and (11) were supplemented with various types of sources S_+ and sinks S_-. First, solutions were obtained for the case where the positions of a source and a sink in momentum space were matched with the direction of a flow sustained by collisions. Note that analytic consideration of equations for the case of a localized source and sink gives a correct flow direction, namely, from high to low velocities [3]. It was shown in [23] that, within the interval between the source and sink, an SND (of the Kolmogorov kind) of particles is established with time. This distribution corresponds to the presence of an energy flow in momentum space, whereas beyond this interval, the distribution function is thermodynamically equilibrium. When using the Landau equation, the particle distribution relaxes to an SND by more than one order of magnitude faster than when the Fokker–Planck equation is used. As was noted above, the positions of the

source and sink and the direction of flow in momentum space should be matched with one another. To make sure once again that this requirement is important, we performed calculations with the interchanged positions of the source and sink in energy space. It turned out that variations in the flow intensity by several orders of magnitude did not influence the equilibrium particle distribution when the source and sink positions were not matched with the flow direction.

The dependence of the EDF on the degree of the source and sink localization in energy space is illustrated in Figs. 6 and 7. It can seen that the behavior of the SND in most of the interval between the source and sink does not depend on the degree of the source (sink) localization; this indicates the local (universal) character of the solution.

Figure 8 shows the distribution functions for different flow intensities. It is found that, for low intensities of the source I_+ (sink I_-), a universal nonequilibrium distribution is formed in the velocity range $v \le v_+$. This is due to (i) a decrease in the cross section for Coulomb scattering with increasing velocity ($\sim v^{-3}$) and (ii) the ever-present flow of energy and particles (due to Coulomb diffusion) toward the region of the main ("background") equilibrium distribution. Consequently, as the source (sink) intensity increases, a universal nonequilibrium particle distribution is formed that occupies a progressively larger space between the source and sink. Such behavior is related to a decrease in the fraction of the flow transferred to the background plasma. It is worth noting that the increase in intensity is accompanied by an increase in the magnitude of the nonequilibrium distribution function in proportion to the flux magnitude [3].

Let us examine the form of the distribution function for power-law interaction potentials with the exponents $1 \le \beta \le 4$. Note that $\beta = 1$ corresponds to the Coulomb interaction potential, $\beta = 2$ corresponds to dipole interaction, and $\beta = 4$ describes the interaction of so-called Maxwellian molecules. Figure 9 shows nonequilibrium distribution functions for the case of a steady-state energy flow with an intensity of $I = 0.01$ and $\beta = 1$, 2, and 4. It can be seen that, for all these β values, the exponents of the formed nonequilibrium power-law distribution functions are close to one another, which agrees with the results of [3]. The magnitude of the nonequilibrium part of distribution function decreases with increasing β. These results are in qualitative agreement with the above analytic predictions.

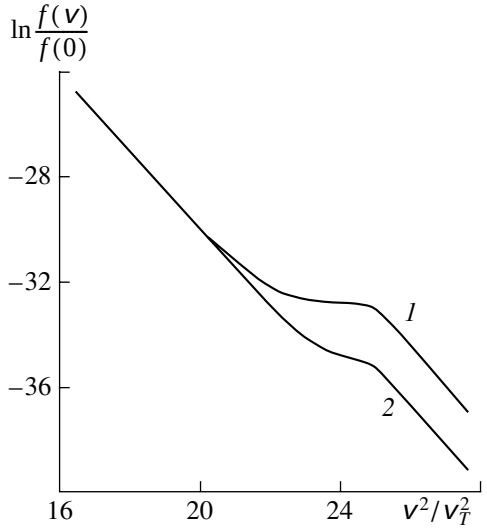

Fig. 8. Steady-state distribution function obtained from the Landau equation for $\beta = 1$ and an exponential source sink and sink at two values of the flux intensity in phase space: $I_1 = 0.01$ and $I_2 = 0.001$ ($v_- = 4$, $v_+ = 5$).

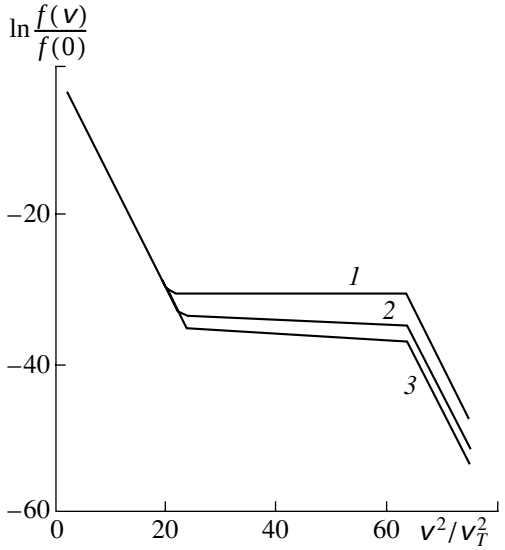

Fig. 9. Steady-state nonequilibrium distribution functions vs. squared velocity for a constant energy flux with an intensity of $I = 0.01$. The source and sink are in the form of δ function (19) with $v_- = 4$ and $v_+ = 8$. Curves *1*, *2*, and *3* are calculated using the collision integrals in the Landau form with exponents $\beta = 1$, 2, and 4, respectively.

4. FORMATION OF THE EDF IN THE INTERACTION OF RADIATION AND PARTICLE BEAMS WITH SOLID-STATE PLASMA

In this section, we consider the conduction and emission properties of a semiconductor plasma irradiated with intense particle or laser beams.

A comparison of the characteristic times of ionization and relaxation shows that, in the case at hand, the steady-state EDF should be determined mainly by electron–electron collisions [3]. Hence, it can be obtained from the condition that the Boltzmann collision integral (for a semiconductor plasma, the Landau or Fokker–Planck collision integral) be zero.

It follows from the above analysis that, for a semiconductor plasma in the energy range $E - E_F > E_F$, a power-law distribution with a nonzero flux of energy or particles in momentum space can be established. This distribution is formed due both to collisions with electrons whose energy is in the range $E - E_F > E_F$ and background (equilibrium) electrons.

It was shown above that a nonequilibrium electron distribution is close to a universal distribution if the intensity of the flow produced by the source and sink in momentum space is sufficiently high.

Let us consider, as an example, the irradiation of a solid-state plasma with a beam of fast ions (with velocities higher than the velocities of atomic electrons) or high-power electromagnetic radiation with the frequency ω satisfying the condition $\hbar\omega \gg k_B T$. In both these cases, a great number of high-energy electrons arise that, in accordance with the above consideration, form a nonequilibrium steady-state EDF. When the distribution function is nonequilibrium, the emission current density is anomalously high since the distribution function decreases very slowly over the inertial interval. The plasma conductivity is determined by the density of current carriers. In the case of a nonequilibrium EDF, the carrier density in semiconductor plasma is very high in comparison to the case of an exponentially decreasing equilibrium EDF. Therefore, when a semiconductor plasma is irradiated with intense radiation or particle beams, an anomaly in the emission and conduction properties of plasma should be observed. Indeed, such an anomaly was observed, e.g., in [26, 27].

Supplying additional kinetic energy to a solid-state plasma results in the ionization of atoms and the production of a rather large number of free electrons with energies higher than the equilibrium (thermal) energy [28]. Under these conditions, nonequilibrium distributions of free electrons can form [3, 4]. It was shown in a series of theoretical and experimental studies that, when a solid-state plasma is irradiated with fast ion beams, a steady-state nonequilibrium power-law EDF

$$f(E) = \alpha I^{1/2} E^{-s} \tag{20}$$

is formed in the plasma due to the presence of a particle (energy) flow produced by a source (ionization) and a sink (electron emission) in momentum space. In Eq. (20), α is the normalizing factor, I is the particle (energy) flux, s is an exponent [4, 5], and E is the total electron energy in a solid ($E = \varphi + E_F + eU$, where φ is the work function and eU is the energy relative to the electron energy in vacuum). Power-law distributions are characterized by a rather large fraction of high-energy electrons. For example, when a Be sample is irradiated with 4.9-MeV α particles, the fraction of electrons with energies higher than $E_p = 18.9$ eV (where E_p is the energy of plasma eigenmodes in beryllium) can exceed 37% [29].

When the velocity v of an incident ion is much higher than the velocities of the target's electrons, the elastic losses are negligibly small, whereas the inelastic energy losses, which are usually called ionization loss, are described by the Bethe–Bloch formula [30]

$$-dE/dx = (4\pi Z_1^2 e^4/mv^2) Z_2 N \ln(2mv^2/I), \tag{21}$$

where m is the electron mass; Z_1 is the charge number of the incident ions; Z_2 is the atomic number of the target material; and N and I are the density and the average excitation potential of the target's atoms, respectively. It follows from formula (21) that, at high energies, the ionization loss decreases as v^{-2}. The introduction of an extra charge in a quasineutral equilibrium solid-state plasma leads to the displacement of free electrons with respect to their equilibrium positions and to the excitation of plasma eigenmodes (plasmons) [31]. Thus, the energy lost by an ion due to its deceleration is transferred to the target's electrons in two ways: a certain fraction of the energy is spent on the excitation of plasmons, while the rest energy is transferred to individual electrons in collisions (in particular, in collisions with atoms, which then become ionized) [28]. Such a nonequilibrium external action significantly changes the distribution function of free electrons [4].

A fraction of the nonequilibrium electrons that have proper magnitudes and momentum directions can escape from the target; i.e., these electrons can take part in the process of secondary ion-induced electron emission (SIEE). The emission proceeds in three stages:

(i) origin of nonequilibrium electrons,

(ii) their collisions and motion (diffusion) toward the surface of a solid, and

(iii) overcoming the potential barrier by these electrons and their escape into vacuum.

Such an approach is believed to most comprehensively account for the SIEE features and has been widely used since the Sternglass study [32] (see also [33]). The processes of electron diffusion to the surface and overcoming the potential barrier seem to be the same for the electrons produced by ion bombardment and the electrons produced as a result of target irradiation by electron or laser beams [34].

An integral characteristic of SIEE is the SIEE coefficient γ, often called the electron yield (see [35]). The electron yield γ is defined as the ratio of the number of knocked-out secondary electrons N_e to the number of incident ions N_i,

$$\gamma = N_e/N_i. \tag{22}$$

The SIEE coefficient depends substantially on the energy of incident ions. It has been shown both theoretically and experimentally that, for low-Z ions, the electron yield γ is proportional to the average specific ionization loss of ion energy in matter, dE/dx [32, 35, 36].

A much more informative characteristic of SIEE is the electron energy distribution. It has been shown experimentally that the energy spectra of secondary electrons are of power-law character [6, 37, 38]. When

studying electron emission from some metals, it was shown that the distribution functions of the electrons knocked out by low-Z ions are piecewise power-law functions with different exponents s for different energy ranges [5, 6, 39].

As was shown in [40], emissivity variations accompanying the irradiation of a sample with intense charged particle beams can be efficiently used to create new energy sources. One such source is a secondary-emission radioisotope current source [41] that converts the energy of α particles into electrical energy using the nonequilibrium properties of the electron distributions. Since the efficiency of this source is proportional to the difference between the electron yields of the employed emitter materials ($\gamma_2 - \gamma_1$) [41], it is necessary to use an emitter with the maximum possible γ_2 value to increase the source efficiency.

At present, the available literature data on the emission properties of materials irradiated with fast ion beams mainly refer to metals. Note that no data are available in the literature on the efficient electron emitters widely used in the photoemission and electronic techniques. Among the most widely used efficient emitters of secondary electrons are emitters based on Sb/Cs compounds. Due to the large coefficients of secondary electron emission (SEE) and photoemission (this is usually related to the low potential barrier at the boundary between the sample surface and vacuum), such compounds have been widely used in manufacturing the photocathodes and dynodes in photomultipliers and other devices [42]. To illustrate, the SEE coefficient σ for Sb/Cs compounds is 3–4 at low energies of primary electrons ($E_e \sim 100$ eV) and reaches its maximum value of $\sigma_{max} = 8$–10 at $E_e = 500$–600 eV [42]. Such large SEE coefficients are presumably explained not only by the low work function for this material but also the formation of a power-law nonequilibrium distribution function.

5. EXPERIMENT

This section is devoted to our experimental studies aimed at revealing the main features of the EDFs formed during the irradiation of a Sb/Cs cathode and certain semiconductors with a beam of fast low-Z ions.

5.1. Experimental Setup

A schematic of the experimental setup used to study the EDFs formed in the solid-state plasmas of semiconductors and of a Sb/Cs cathode irradiated with a beam of fast low-Z ions is shown in Fig. 10.

An electrostatic Van de Graaf generator used as a source of primary particles provided beams of H^+ or He^+ ions. Energy spectra of SIEE electrons were measured for H^+ beams with ion energies from 1.00 to 2.25 MeV and He^+ beams with ion energies from 1.75 to 2.25 MeV. The ion energy was varied with a step of

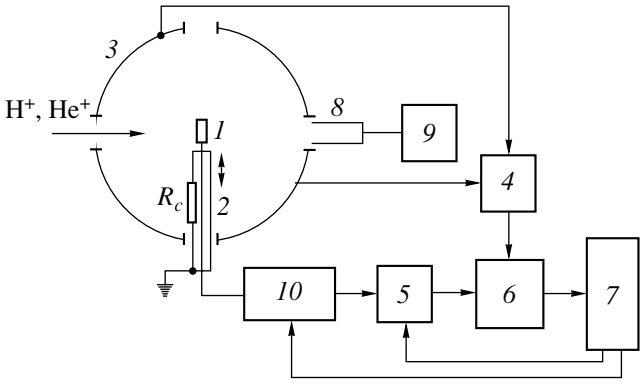

Fig. 10. Schematic of the experimental setup: (*1*) target, (*2*) target holder, (*3*) hemispheres, (*4*, *5*), electrometric amplifiers, (*6*) analog-to-digital converter, (*7*) PC, (*8*) Faraday cup, (*9*) F303 current meter, and (*10*) saw-tooth voltage generator.

0.25 MeV. The cathode used as a target was a Sb/Cs layer deposited on a massive nickel substrate. The layer thickness was less than the mean free path of the incident ions in Sb/Cs. A 10-mm-diameter target (*1*) fixed in a copper mount was installed on a movable holder (*2*). The ion beam collimated by a system of diaphragms was incident onto the target and caused SIEE from its surface. The target plane was normal to the beam axis. The beam diameter on the target surface was 3 mm, and the ion current density was no higher than 30 $\mu A/cm^2$. The chamber was evacuated with an NMD-0.4-1 magnetic-discharge pump and an NVPR-16D backing pump with a liquid nitrogen trap. In all our experiments, the residual gas pressure in the vacuum chamber was no higher than 10^{-6} torr.

The electrons emitted from the target surface were intercepted by a spherical collector consisting of two 100-mm-radius hemispheres (*3*). The target and the holder were set inside the collector. The gap between the hemispheres was 15 mm. The diameter of the entrance window of the hemisphere was 10 mm. Besides the collector current, we also measured the target current I_T, which was the sum of the beam ion current I_B and the current of the secondary electrons that reached the collector: $I_T = |I_C| + I_B$. The measured I_C and I_T currents amplified by electrometric amplifiers (*4* and *5*, respectively) were applied to a PC (*7*) through an analog-to-digital converter (*6*). To calibrate the measurement system, a Faraday cup (*8*) was set behind the rear hemisphere. The Faraday cup allowed us to directly measure the ion beam current I_{FC} when the target was removed from the beam path. The diameter and length of the Faraday cup were 20 and 130 mm, respectively. The current from the Faraday cup I_{FC} was measured with an F303 current meter (*9*). The SIEE coefficient was determined by the formula

$$\gamma = |I_C|/(I_T - |I_C|). \quad (23)$$

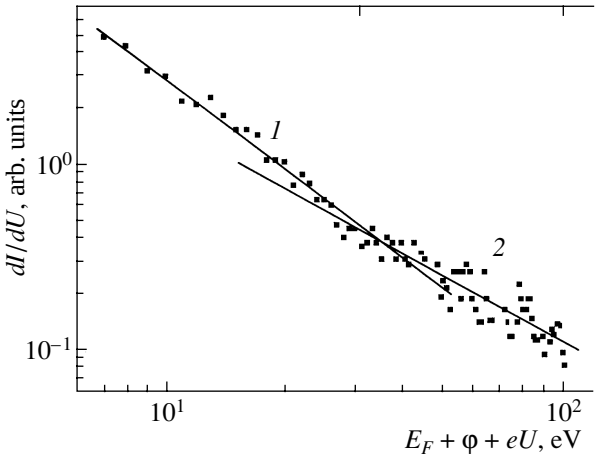

Fig. 11. Typical dependence of $\log(dI/dU)$ on $\log(E_F + \varphi + eU)$, plotted on a double logarithmic scale, for a Sb/Cs cathode bombarded with 1.75-MeV He^+ ions. Energy ranges *1* (5–30 eV) and *2* (30–100 eV) correspond to the exponents $s_1 = 2.9$ and $s_2 = 2.5$, respectively.

By measuring the energy spectrum of SIEE electrons with a spherical analyzer and assuming that emission is produced by a point source, one can reconstruct the EDF inside the target [20]. When the EDF is power-law function (20), the derivative of the emission current with respect to the electron energy, dI/dU, can be written as

$$dI/dU = B(E_F + \varphi + eU)^{-s+1}, \qquad (24)$$

where B is a constant. Hence, on a logarithmic scale, dependence (24) is a straight line with a slope equal to $-s + 1$.

The energy distributions of the secondary emission electrons were measured with a spherical collector operating in the energy-analyzer regime with a retarding field varied in the range 0–100 V with a step of 1 V. The retarding electric potential was applied between the target (*1*) and two hemispheres (*3*). Since the radius of the energy analyzer significantly exceeded the target size, the field distribution was close to spherical. A 5-mm-diameter ceramic tube with an outer surface covered with a resistive layer served as a target holder (*2*). The specific resistance of the layer R_c was varied nonlinearly along the tube so that the holder potential did not disturb the field inside the energy analyzer. One end of the resistive layer was in contact with the target, whereas its other end was grounded. The retarding potential was applied to the target from a saw-tooth generator (*10*) controlled by a PC (*7*). Thus, the current flowing along the resistive layer produced the needed potential distribution along the holder. In experiments, the secondary electrons moved along radial trajectories and reached the collector. When the retarding voltage was applied to the target, only the electrons whose energy was high enough to get through the retarding field reached the collector. The computer software for controlling the experiment allowed the gathering of a 7-s-long time sample consisting of 100 measurements of the electron emission current for each value of the retarding field. These 100 experimental points were then averaged, and the resultant value of the electron current was stored in the PC memory. By differentiating the measured dependence of the collector current on the retarding voltage (the so-called retarding curves), one can deduce the energy spectrum of SIEE electrons and then reconstruct the EDF.

Table 1

Ion	Energy, MeV	Exponent	
		s_1	s_2
H^+	1.25	2.9	2.5
	1.50	3.0	2.5
	1.75	2.9	2.5
	2.00	3.0	2.4
	2.26	3.0	2.6
He^+	1.75	2.9	2.5
	2.00	2.8	2.2
	2.26	2.8	2.3

The exponents s of power-law EDFs were evaluated as follows. First, the time samples of the electron emission current were processed and the delay curves were differentiated. Then, the dependences of dI/dU on the total electron energy $E_F + \varphi + eU$ in the compound under study, plotted on a logarithmic scale, were approximated by straight lines. According to formula (24), the slopes of these straight lines are equal to $-s + 1$.

5.2. Experimental Results and Discussion

The measurements of the energy spectrum of SIEE electrons show that, over the entire ion energy range under study, the nonequilibrium EDF formed in the plasma of a Sb/Cs cathode is a power-law function.

A typical nonequilibrium EDF obtained for a sample bombarded with 1.75-MeV He^+ ions is shown in Fig. 11. The experimental points are quite well fit by two straight lines corresponding to two different exponents, s_1 and s_2, in the energy ranges of 5–30 eV and 30–100 eV, respectively. These exponents for the two parts of the EDF in the above energy ranges are shown in Table 1 as functions of the energy of the incident H^+ and He^+ ions.

In our opinion, the exponent of a power-law distribution function of secondary electrons could depend on the energy (specific ionization loss) of fast ions. It seems that it is the specific ionization loss that determines the intensity of the source of extra particles in momentum space. It was shown in [4, 43] that, under certain conditions, the exponent is independent of the structure of the source and sink. In this case, it can be said to be a universal power-law distribution function with an exponent equal to –5/4 [43]. In our previous experiments with a He^+ beam and thin metal films, in which the exponents s were measured, it was shown that the absolute value of the exponent s_1 of a power-law distribution function in the first energy range corresponding to slow electrons ($E < 35$ eV) decreases with increasing specific ionization loss of ions in a substance [39]. In [38], it was pointed out that the fraction of fast electron increases with increasing energy of the incident ions. It can be seen from Table 1 that the exponents s_1 for different incident ions and, accordingly, different specific ionization losses in a Sb/Cs sample differ insignificantly, although, for protons, the exponent increases with ion energy and decreases with specific ionization loss. No such dependence was observed for helium ions. It should be noted that variations in the exponent do not exceed 10%; to deduce the exact dependence of the exponent on the energy loss requires additional study.

Figure 12 shows the dependence of the electron yield γ on the energy of the incident H^+ and He^+ ions for a Sb/Cs cathode. It can be seen that, for the Sb/Cs compound under study, the electron yield γ exceeds that for some metals [35]. The reason could be as follows. As was mentioned above, a fraction of the nonequilibrium electrons produced in a solid-state plasma under bombardment with a beam of fast charged particles diffuse toward the surface and escape into vacuum. Electron emission proceeds from the surface layer, whose thickness is much less than the depth to which the ions penetrate into the target and is determined by the features of the electron motion toward the surface. In metals, the generated electrons, while diffusing toward the surface, interact mainly with conduction electrons. This interaction may proceed via pair collisions and collective effects—the excitation of plasmons. Due to the large density of conduction electrons in metals, the probability of electron–electron interactions and, accordingly, the effective escape depth of secondary electrons are small. In semiconductors, the density of conduction electrons is low; hence, the escape depth of secondary electrons can be quite large. Since Sb/Cs compounds possess semiconductor properties [42], the escape depth of nonequilibrium electrons can be larger than in metals. The higher (compared to metals) value of the SIEE coefficient can be, to a certain extent, explained by this factor.

Sb/Cs compounds have low work functions [44]. The relatively low potential barrier at the boundary between such a compound and vacuum may lead to an increase in the fraction of nonequilibrium electrons leaving the solid. The work function determines the cutoff energy for the nonequilibrium power-law EDF formed in a solid-state plasma. Since the exponent within the first energy interval is fairly high (see Table 1 and [6, 37–39]), even a slight decrease in the work function leads to a significant increase in the SIEE coefficient.

Our experiments have shown that, for all of the energies of H^+ and He^+ ions, the EDFs formed in a semicon-

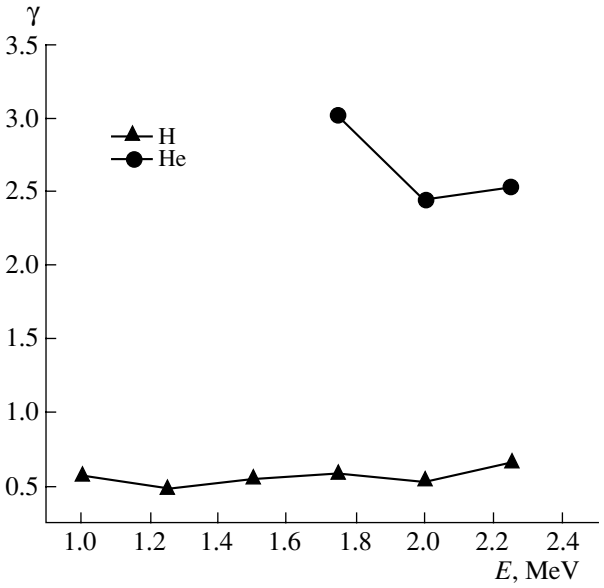

Fig. 12. Electron yield γ for a Sd/Cs cathode vs. energy of incident H^+ and He^+ ions.

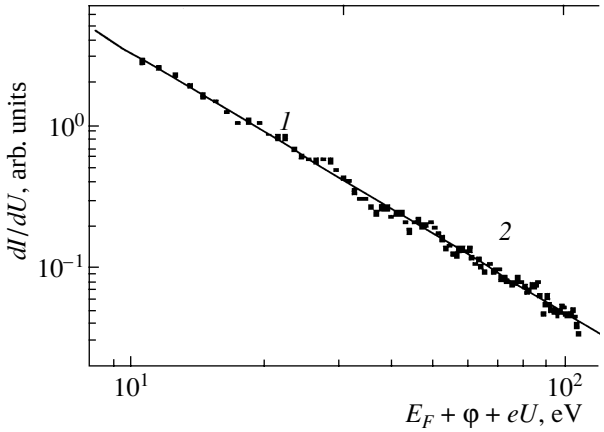

Fig. 13. Distribution function of the nonequilibrium electrons for GaAs bombarded with 1.25-MeV He^+ ions, plotted on a double logarithmic scale.

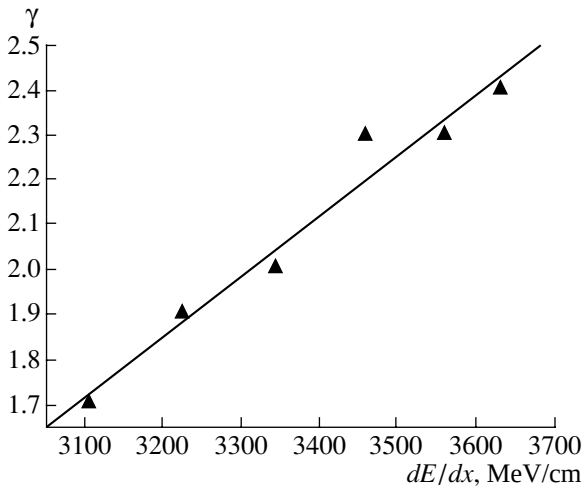

Fig. 14. Electron yield for germanium vs. specific ionization loss dE/dx for He^+ ions.

ductor plasma are power-law functions. Figure 13 shows (on a double logarithmic scale) a typical nonequilibrium EDF formed in a GaAs sample bombarded with 1.25-MeV He^+ ions. The experimental points can be well fit by a single straight line corresponding to the exponent $s = 2.9$ throughout the entire range of electron energies in vacuum (5–100 eV). Table 2 presents the exponents s obtained by processing the experimental data for all the samples under study and all the energies of the incident ions.

It was shown in our early experiments [20] that the EDFs formed in metal plasmas are piecewise power-law functions with different exponents in different energy ranges. At least two such ranges were revealed.

In our opinion, the piecewise power-law shape of the EDFs in experiments with metals, namely, the presence of two characteristic energy ranges, could be related to two different mechanisms for energy transfer from a fast incident ion to the electron subsystem of a solid. These mechanisms are (i) the excitation of collective plasma oscillations with a subsequent ionization in the electric field of these oscillations and (ii) inelastic collisions, resulting in the direct ionization of atoms. The energy of the electrons produced due to ionization via plasma oscillations cannot exceed the plasmon energy E_p in a substance. In semiconductors, the energy of plasmons related to conduction electrons is much lower than the ionization potential of atoms. For this reason, the distribution function in a semiconductor plasma is characterized by one power-law segment throughout the entire electron energy range under study.

The measurements of the energy spectrum of SIEE electrons have shown that, for all of the ion energies under study, the nonequilibrium EDFs formed in plasma are power-law in character.

As was mentioned above, the main integral characteristic of SIEE is the electron yield γ. Table 3 shows the yields of electron emission induced by He^+ ions for some semiconductors. It can be seen from Fig. 14 that, in germanium, the measured values of γ plotted versus the ionization loss dE/dx for He^+ ions are well fitted by a straight line; i.e., these quantities are indeed proportional to one another.

Table 2

Ion	Energy, MeV	Exponent s		
		GaAs	Ge	CdTe
He^+	1.00	–	2.8	–
	1.25	2.9	2.8	–
	1.50	2.9	2.8	–
	1.75	2.6	2.7	2.9
	2.00	2.6	2.8	2.8
	2.26	2.7	2.8	2.9
H^+	1.00	3.1	2.9	3.1
	1.25	2.9	2.8	3.0
	1.50	2.8	2.9	3.0
	1.75	2.8	2.6	2.7
	2.00	2.7	2.6	2.7
	2.26	3.0	2.8	2.8

Table 3

Energy, MeV	Electron yield γ		
	GaAs	Ge	CdTe
1.00	–	2.4	–
1.25	2.3	2.3	–
1.50	2.2	2.3	–
1.75	1.7	2.0	2.0
2.00	2.1	1.9	1.9
2.26	1.9	1.7	1.9

6. CONCLUSIONS

In this paper, we have shown that the presence of sources and sinks in a spatially uniform system leads to the formation of SNDs with power-law tails. A kinetic equation for the electrons scattered by acoustic phonons in a solid has been derived, and relations between power-law asymptotic solutions and the particle and energy fluxes in phase space have been established. The nonextensive thermodynamics of a nonequilibrium solid-state plasma has been developed based on the SNDs under study.

Numerical simulations of the formation of SNDs show that, for particles with Coulomb interaction, an SND is formed between the source and sink. Starting from a certain intensity of the source (sink), the power-law distribution function has the same exponent; i.e., it is universal. A radical change in the EEDF under nonequilibrium conditions leads to an anomalous increase in the conductivity and emissivity of the substance.

The experimental data on the EEDFs formed in the solid-state plasma of a Sb/Cs cathode irradiated with a beam of fast low-Z ions are presented. In all of the experiments with H^+ and He^+ ions, the nonequilibrium EEDFs in the energy range from 5 to 100 eV are found to have a piecewise power-law shape with different exponents in the energy ranges of 5–30 and 30–100 eV. The power exponents are expected to depend on the energy (specific ionization loss) of fast ions, and this was indeed observed for protons in the former energy range.

Our experimental studies of the formation of nonequilibrium electron distributions in a semiconductor plasma exposed to ion beams have shown that EEDFs have power-law asymptotes with one exponent. This is related to the low energy of the plasma oscillations carried by the conduction electrons.

ACKNOWLEDGMENTS

We are grateful to Prof. S.S. Moiseev (deceased), who initiated this study, for his continuous interest in this work. We are also grateful to the personnel of the VG-5 accelerator at the Kharkov Institute for Science and Technology and especially to V.M. Mishchenko for creating optimal conditions for our work. This study was supported by the Science and Technology Center in Ukraine, project no. 1862.

REFERENCES

1. A. V. Kats, V. M. Kontorovich, S. S. Moiseev, and V. E. Novikov, Preprint No. 42 (Institute of Radioelectronics, Academy of Sciences of the Ukr. SSR, Kharkov, 1974).
2. A. V. Kats, V. M. Kontorovich, S. S. Moiseev, and V. E. Novikov, Pis'ma Zh. Éksp. Teor. Fiz. **21**, 13 (1975) [JETP Lett. **21**, 5 (1975)]; Zh. Éksp. Teor. Fiz. **71**, 177 (1976) [Sov. Phys. JETP **44**, 93 (1976)].
3. V. I. Karas', S. S. Moiseev, and V. E. Novikov, Pis'ma Zh. Éksp. Teor. Fiz. **21**, 525 (1975) [JETP Lett. **21**, 245 (1975)]; V. I. Karas', Pis'ma Zh. Tekh. Fiz. **1** (21), 1020 (1975) [Sov. Tech. Phys. Lett. **1**, 438 (1975)].
4. V. I. Karas', S. S. Moiseev, and V. E. Novikov, Zh. Éksp. Teor. Fiz. **71**, 1421 (1976) [Sov. Phys. JETP **44**, 744 (1976)].
5. E. N. Batrakin, I. I. Zalyubovskiĭ, V. I. Karas', *et al.*, Zh. Éksp. Teor. Fiz. **89**, 1098 (1985) [Sov. Phys. JETP **62**, 633 (1985)].
6. E. N. Batrakin, I. I. Zalyubovskiĭ, V. I. Karas', *et al.*, Poverkhnost, No. 12, 82 (1986).
7. V. I. Karas', S. I. Kononenko, and V. I. Muratov, Vopr. At. Nauki Tekh., Ser.: Yad. Fiz. Issled. **1**, 71 (2001).
8. V. E. Novikov, A. V. Tur, and V. V. Yanovskiĭ, *Problems of Theoretical Physics* (Naukova Dumka, Kiev, 1986).
9. V. E. Novikov, S. S. Moiseev, and V. P. Seminozhenko, Fiz. Tekh. Poluprovodn. (Leningrad) **14**, 402 (1980) [Sov. Phys. Semicond. **14**, 236 (1980)].
10. V. I. Karas', V. E. Novikov, S. S. Moiseev, and V. P. Seminozhenko, Fiz. Nizk. Temp. **36**, 695 (1977) [Sov. J. Low Temp. Phys. **36**, 336 (1977)].
11. A. V. Bobylev, Dokl. Akad. Nauk SSSR **225**, 1041 (1975) [Sov. Phys. Dokl. **20**, 820 (1975)].
12. V. E. Novikov, S. S. Moiseev, *et al.*, Radiofiz. Radioastron. **4**, 160 (1999).
13. M. H. Ernst, in *Nonequilibrium Phenomena: I. The Boltzmann Equation*, Ed. by E. W. Montroll and J. L. Lebowitz (North-Holland, Amsterdam, 1983; Mir, Moscow, 1986), p. 51.
14. D. Petrina and A. Mishchenko, Dokl. Akad. Nauk SSSR **298**, 338 (1988) [Sov. Phys. Dokl. **33**, 32 (1988)].
15. V. E. Novikov, S. S. Moiseev, A. V. Tur, and V. V. Yanovskiĭ, Zh. Éksp. Teor. Fiz. **86**, 920 (1984) [Sov. Phys. JETP **59**, 537 (1984)].
16. F. G. Bass and Yu. G. Gurevich, *Hot Electrons and High-Power Electromagnetic Waves in Semiconductor Plasmas and Gas Discharges* (Nauka, Moscow, 1975).
17. C. Tsallis, J. Stat. Phys. **52**, 479 (1988); Braz. J. Phys. **29**, 1 (1999).
18. V. I. Karas' and V. E. Novikov, Vopr. At. Nauki Tekh., Ser.: Plazm. Élektron. Novye Metody Uskoreniya **4**, 157 (2003).
19. A. V. Bobylev, I. F. Potapenko, and V. A. Chuyanov, Zh. Vychisl. Mat. Mat. Fiz. **20**, 993 (1980).

20. V. M. Balebanov, V. I. Karas', I. V. Karas', *et al.*, Fiz. Plazmy **24**, 789 (1998) [Plasma Phys. Rep. **24**, 732 (1998)].
21. B. A. Trubnikov, in *Reviews of Plasma Physics*, Ed. by M. A. Leontovich (Gosatomizdat, Moscow, 1963; Consultants Bureau, New York, 1966), Vol. 1.
22. V. P. Silin, *Introduction to the Kinetic Theory of Gas* (Nauka, Moscow, 1971).
23. V. I. Karas' and I. F. Potapenko, Fiz. Plazmy **28**, 908 (2002) [Plasma Phys. Rep. **28**, 837 (2002)].
24. I. F. Potapenko, A. V. Bobylev, C. A. Azevedo, and A. S. Assis, Phys. Rev. E **56**, 7159 (1997).
25. I. F. Potapenko and V. A. Chuyanov, Zh. Vychisl. Mat. Mat. Fiz. **19**, 458 (1979).
26. A. S. Asseevskaya, E. B. Ivkin, and B. G. Kolomiets, Pis'ma Zh. Tekh. Fiz. **2**, 116 (1976) [Sov. Tech. Phys. Lett. **2**, 44 (1976)].
27. S. I. Anisimov, Ya. A. Imas, G. S. Romanov, and Yu. V. Khodyko, *The Effect of High-Power Radiation on Metals* (Nauka, Moscow, 1970).
28. N. P. Kalashnikov, V. S. Remizovich, and M. I. Ryazanov, *Collisions of Fast Charged Particles in Solids* (Atomizdat, Moscow, 1980).
29. V. P. Zhurenko, S. I. Kononenko, V. I. Karas', and V. I. Muratov, Fiz. Plazmy **29**, 150 (2003) [Plasma Phys. Rep. **29**, 130 (2003)].
30. Yu. V. Gott, *Particle Interaction with Substance in Plasma Studies* (Atomizdat, Moscow, 1978).
31. M. C. Steele and B. Vural, *Wave Interactions in Solid State Plasmas* (McGraw-Hill, New York, 1969; Atomizdat, Moscow, 1973).
32. E. J. Sternglass, Phys. Rev. **108**, 1 (1957).
33. H. Rothard, C. Caraby, A. Cassimi, *et al.*, Phys. Rev. A **51**, 3066 (1995).
34. B. A. Brusilovskiĭ, *Kinetic Ion–Electron Emission* (Énergoatomizdat, Moscow, 1990).
35. D. Hasselkamp, K. G. Lang, A. Scharmann, *et al.*, Nucl. Instrum. Methods Phys. Res. B **180**, 349 (1981).
36. J. Schou, Phys. Rev. B **22**, 2141 (1980).
37. W. Meckbach, G. Braunstein, and N. Arista, J. Phys. B **8**, L344 (1975).
38. D. Hasselkamp, S. Hippler, and A. Scharmann, Nucl. Instrum. Methods Phys. Res. B **18**, 561 (1987).
39. S. I. Kononenko, Dopovidi NANU, No. 1, 87 (2001).
40. V. I. Karas' and S. S. Moiseev, Ukr. Fiz. Zh. **24**, 1724 (1979).
41. V. M. Balebanov, S. S. Moiseev, V. I. Karas', *et al.*, At. Energ. **84**, 398 (1998).
42. N. A. Soboleva and A. E. Melamid, *Photoelectronic Devices* (Vysshaya Shkola, Moscow, 1974).
43. V. I. Karas', S. S. Moiseev, and A. P. Shuklin, Ukr. Fiz. Zh. **25**, 820 (1980).
44. V. S. Fomenko and I. A. Podchernyaeva, *Emission and Adsorption Properties of Substances and Materials* (Atomizdat, Moscow, 1975).

Translated by N.N. Ustinovskiĭ

Plasma Physics Reports, Vol. 30, No. 8, 2004, pp. 687–697. Translated from Fizika Plazmy, Vol. 30, No. 8, 2004, pp. 739–749.

ION AND PLASMA SOURCES

Low-Power Inductive RF Plasma Sources for Technological Applications

K. V. Vavilin*, A. A. Rukhadze, M. Kh. Ri*, and V. Yu. Plaksin***

**Moscow State University, Vorob'evy gory, Moscow, 119899 Russia*

***Prokhorov Institute of General Physics, Russian Academy of Sciences, ul. Vavilova 38, Moscow, 119991 Russia*

Received June 4, 2003; in final form, November 20, 2003

Abstract—The objective of the present paper is to develop an analytic theory of cylindrical low-power RF plasma sources operating at an industrial frequency ($f = 13.56$ MHz, $\omega = 8.52 \times 10^7$ s^{-1}). Inductive surface exciters of electromagnetic fields (exciting antennas) are considered that are positioned either at the side surface of the cylinder or at one of its end surfaces. In the latter case, the plasma flows out of the source through the opposite end surface of the cylinder. A study is made of elongated systems in which the length L of the cylinder exceeds its diameter $2R$ and of planar disk-shaped systems with $L < 2R$. Simple analytic expressions are derived for electromagnetic fields excited by the antenna in the source plasma. The equivalent plasma resistance and the equivalent RF power deposited in the plasma are calculated for systems with prescribed parameters, i.e., in a non-self-consistent model. Up to now, such sources have been investigated mainly through the numerical solution of the complicated general electrodynamic equations. In the Introduction, the problem is formulated in general terms and the geometry of the sources, as well as the characteristic parameters of the source plasma, is discussed. In Section 2, plasma sources operating without an external magnetic field are investigated. In Section 3, helicon plasma sources in a sufficiently strong external magnetic field are considered. Analytic predictions are compared with the results from solving the problem numerically without using the helicon approximation. Section 4 gives a brief discussion of an electron cyclotron resonance–based RF plasma source. In the Conclusion, the main results of the paper are summarized and the technological efficiency of the sources under consideration is estimated at a qualitative level. © *2004 MAIK "Nauka/Interperiodica"*.

1. INTRODUCTION

We begin by discussing the geometric features of the plasma sources that are the subject of the present study. We are interested in cylindrical sources elongated along the cylinder axis ($L > 2R$) and in planar disk-shaped cylindrical sources with $L < 2R$ (see Figs. 1a, 1b). The sources differ not only in shape but also in the arrangement of antennas at the cylinder surface. In an elongated plasma source, the electromagnetic field is produced by a current-carrying antenna positioned at the side surface of the cylinder (Fig. 1a) and, in a planar source, the antenna is positioned at the closed end, opposite to the end through which the plasma flows out of the cylinder (Fig. 1b).

In a planar source, the end surface through which the plasma flows out of the cylinder is a metal grid. Since the grid cells are assumed to be small, the boundary conditions at the grid can be written as

$$E_r\big|_{z=L} = E_\varphi\big|_{z=L} = 0. \tag{1.1}$$

For an elongated plasma source with an antenna at its side surface, the same boundary conditions are satisfied at the upper closed end of the cylinder. In a planar disk-shaped source, the current-carrying antenna is positioned at the upper end surface of the cylinder, so that the boundary conditions at this surface are not fixed but instead are derived from the field equations. As for the side surface of a planar source, it is usually metallic, so that the boundary conditions at this surface should have the form

$$E_\varphi\big|_{r=R} = E_z\big|_{r=R} = 0. \tag{1.2}$$

In contrast, in an elongated plasma source, it is at the side surface of the cylinder that the current-carrying antenna is positioned, so that the boundary conditions at this surface are not fixed but are derived from the field equations.

Let us now discuss the design of the antennas in question. In the most general case, the current density in the antenna positioned at the side surface of the cylinder can be represented as

$$\mathbf{j}(r) = \delta(r - R)\mathbf{F}_1(\varphi, z), \tag{1.3}$$

where $F_1(\varphi, z)$ is an arbitrary function of its arguments, which can be expanded in a Fourier series. Below, the problem will be solved for an individual term of the Fourier series under the assumption that the antenna current is azimuthally symmetric and the arbitrary function has the form $\mathbf{F}_1(\varphi, z) \sim \mathbf{i}_\varphi I_0 \sin\dfrac{\pi z}{L}$, where I_0 is the net antenna current and $\mathbf{i}_\varphi$ is a unit vector in the azimuthal direction (see formula (3.6) for details).

1063-780X/04/3008-0687$26.00 © 2004 MAIK "Nauka/Interperiodica"

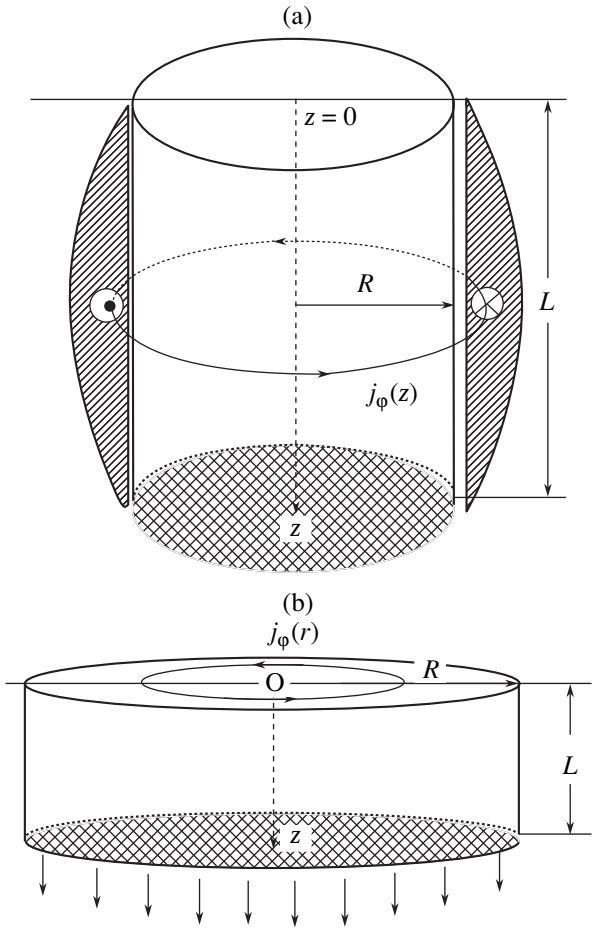

Fig. 1. Schematics of (a) an elongated plasma source and (b) a planar disk-shaped plasma source.

The current density in the antenna positioned at the end surface of the cylinder is represented in an analogous form. In the general case, the antenna current density can be written as

$$\mathbf{j}(r) = \delta(z)\mathbf{F}_2(\varphi, r). \quad (1.4)$$

In what follows, however, we will be interested in an azimuthally symmetric antenna current and will use the function $\mathbf{F}_2(\varphi, r) \sim \mathbf{i}_\varphi I_0 J_1\left(\frac{\mu r}{R}\right)$, where I_0 is the net antenna current, $J_1(x)$ is a first-order Bessel function, and $\mu \approx 3.8$ is the first root of the Bessel function ($J_1(\mu) = 0$) (see formula (2.2) for details).

Let us now discuss the mechanisms by which the RF energy is dissipated within the plasma of the source. We are interested in a plasma with the following parameters: the neutral gas pressure is $p_0 < 10^{-3}$ torr (which corresponds to a neutral density of $n_0 \le 3 \times 10^{13}$ cm^{-3}) and the electron density is $n_e \approx 10^{10}$–10^{13} cm^{-3}. In such a plasma, two dissipation mechanisms—collisionless dissipation due to the Cherenkov absorption of the field by the plasma and collisional field dissipation due to collisions of plasma electrons with plasma ions and with gas atoms and molecules—play an important role. In this case, the collision frequency can be represented as

$$\nu_e = \nu_{en} + \nu_{ei} \approx \sqrt{T_e}6 \times 10^9 p_0 + \frac{3 \times 10^{-5} n_e}{T_e 3/2}, \quad (1.5)$$

where the electron temperature T_e is in eV, the gas pressure p_0 is in torr, the electron density n_e is in cm^{-3}, and the collision frequency is in s^{-1}. Note that, in source plasmas, the electron temperature satisfies the condition $T_e \gg T_i \sim T_0$, where T_i is the ion temperature and T_0 is the gas temperature (which is usually on the order of room temperature). Such plasma parameters result from the large difference between the mass of the electrons and the masses of heavy particles (ions and neutrals), in which case the collisional energy exchange between electrons and heavy particles is hindered. For typical experimental conditions such that $T_e \sim 5$ eV and $V_{Te} \approx 10^8$ cm/s, and for $n_e \le 10^{13}$ cm^{-3} and $p_0 \le 10^{-3}$ torr, we have $\nu_e \le 3 \times 10^7$ s^{-1}. Under these conditions, the collisional dissipation of the RF energy in the plasma can be assumed to be weak because $\omega = 8.5 \times 10^7$ s$^{-1} \gg \nu_e \le 3 \times 10^7$ s^{-1}.

For the above plasma parameters, the mean free path of an electron is on the order of $l = V_{Te}/\nu_e \ge 3$ cm. It can be shown that the maximum efficiency of a plasma source operating in a steady mode is achieved when the length of the system only slightly exceeds the electron mean free path l, i.e., when

$$L \le (2\text{–}3) l_e \approx 10 \text{ cm}. \quad (1.6)$$

In what follows, this condition will be assumed to be always satisfied.

The second, purely collisionless, dissipation mechanism is governed by both the electron thermal motion and the geometric dimensions of the system. The contribution of this mechanism to the collision frequency is determined by the parameters $kV_{Te} \approx \pi V_{Te}/L$ and $\pi V_{Te}/R$. The characteristic geometric dimensions of an elongated RF plasma source are $L \ge 10$ cm and $R \le 10$ cm, while those of a planar source are $L \le 10$ cm and $R \ge 10$ cm. As a result, we have $kV_{Te} \approx (1\text{–}2) \times 10^7$ s$^{-1} \ll \omega$, so that the collisionless RF energy dissipation in the sources is also weak. On the other hand, we have $kV_{Te} \sim \nu_e$, which indicates that the collisionless dissipation is comparable in importance to the collisional dissipation. This is why we will assume that both of the dissipation mechanisms operate simultaneously in the plasma.

The external magnetic field is longitudinal only, $\mathbf{B}_0 \parallel \mathbf{z}$. It has an important effect on the operating modes of the plasma sources. It is easy to show that, even for

relatively weak external magnetic fields ($5 \le B_0 \le 500$ G), the following conditions hold:

$$\omega_{Le} \ge 10^{10}\ \mathrm{s}^{-1} > \Omega_e = \frac{eB_0}{mc} \ge \omega \approx 8.5 \times 10^7\ \mathrm{s}^{-1}, \quad (1.7)$$

where $\omega_{Le} = \sqrt{4\pi e^2 n_e/m_e}$ is the electron Langmuir frequency and $\Omega_e = eB_0/mc$ is the electron gyrofrequency. These conditions will be assumed to be satisfied for plasma sources with an external magnetic field. Sources with a longitudinal magnetic field are the subject of Sections 3 and 4 of the present paper. The objective of Section 2 is to investigate plasma sources without a magnetic field ($\mathbf{B}_0 = 0$).

Let us now discuss the question of the RF power that is to be deposited in the plasma of the source (i.e., the power that ensures the operation of the source). This power depends substantially on the mass of an ion, M, which is assumed to be about 30–40 masses of a hydrogen atom ($M \sim 10^{-22}$ g). In this case, the plasma flows out of the source with a velocity on the order of the ion acoustic speed (provided that the plasma ions are not accelerated by any additional means),

$$v_s = \sqrt{\frac{T_e}{M}} \approx 3 \times 10^5\ \mathrm{cm/s}.$$

For an ion density of $n_i \approx 10^{12}$ cm^{-3}, this formula yields the following estimate for the density of the ion current from the source:

$$j = en_i v_s \approx (5 \times 10^{-10})(10^{12})(3 \times 10^5)\left(\frac{1}{3 \times 10^9}\right)\frac{A}{\mathrm{cm}^2} \approx 5 \times 10^{-2}\frac{A}{\mathrm{cm}^2}. \quad (1.8)$$

Since the plasma thermal energy is determined by the electron temperature T_e, which is about 5 eV, the density of the power flux from the source through a unit area of the end surface of the cylinder is equal in order of magnitude to

$$P_W \approx n_i v_s T_e + n_i v_s M v_s^2 \approx 2n_i v_s T_e \approx 0.5\ \frac{\mathrm{W}}{\mathrm{cm}^2}, \quad (1.9)$$

so that the net power flux from the source is

$$\mathcal{P}_W = SP_W \approx 0.5S\ \mathrm{W}, \quad (1.10)$$

where the total area of the end surface of the cylinder, S, is expressed in cm^2. For an elongated system with $R < 10$ cm, we have $\mathcal{P}_W < 150$ W, whereas for a planar disk-shaped source with $R > 10$ cm, the net power flux is $\mathcal{P}_W > 150$ W.

It is also an easy matter to estimate the total power that is to be deposited in the discharge plasma in order to maintain the steady-state operation of the source. To do this, we must take into account not only the electron plasma heating to a temperature of $T_e \sim 5$ eV but also the power lost to ionize neutral gas atoms and, in the absence of a magnetic field, the power carried to the side surface of the cylinder by the plasma. Unfortunately, the amount of power expended on ionizing the gas atoms in an RF discharge is very high—about 100 eV (most of the field energy is spent on the excitation of atoms, which is followed by the emission of optical photons from the excited atomic states). As a consequence, the net RF power absorbed by the plasma in the source is higher than the net power flowing out of the source by one or even two orders of magnitude, i.e.,

$$\mathcal{P}_W \approx 10^3\text{–}10^4\ \mathrm{W}.$$

To conclude this section, we will say a few words about additional power losses during the acceleration of ions in plasma sources serving as ion implanters. The problem concerning the power of an ion accelerator is a separate issue and is not related to the problem of the RF power fed into a plasma source. In what follows, we will not deal with the ion-accelerator-related problem, because it goes beyond the scope of this paper, the primary goal of which is to investigate the steady-state operation of RF plasma sources. Strictly speaking, the above estimates are valid merely at a qualitative level. The problem of the power expenditure of the plasma source should be treated in terms of a self-consistent source model. Here, we restrict ourselves to a non-self-consistent model in which all the parameters of the source plasma are assumed to be prescribed and time-independent.

2. PLASMA SOURCE WITHOUT AN EXTERNAL MAGNETIC FIELD

Below, in order to illustrate how the theory of inductive plasma sources is to be constructed, we consider the simplest examples of these devices. We begin by considering plasma sources operating in the absence of an external magnetic field. It is easy to see that, in a plasma with the above densities, the electromagnetic field excited by an antenna in the frequency range under analysis is subject to the skin effect, the skin depth being $r_{sk} \sim c/\omega_{Le} \sim 3$ cm. This indicates that an elongated source without a magnetic field does not hold promise for technological applications: the parameters of such a plasma source are nonuniform in the radial direction because of the radially nonuniform distribution of the RF field. That is why, in this section, we restrict ourselves to planar disk-shaped plasma sources.[1]

In a planar disk-shaped plasma source, the current-carrying antenna is assumed to be positioned at the

[1] Here, the question about the equalization of each of the plasma parameters in the radial direction by different transport processes is deliberately set aside because it requires separate study.

upper end of the cylinder (Fig. 1b) and to have the form of an Archimedes spiral,

$$\rho = a\varphi, \tag{2.1}$$

where a is the spiral radius. In the limit $a \ll R$, the azimuthal current density in the antenna can be written, to a good accuracy, as

$$\begin{aligned} j_\varphi &= \frac{I_0 \mu \delta(z)}{R[1 - J_0(\mu)]} J_1\left(\mu \frac{r}{R}\right) e^{-i\omega t} \\ &= \frac{I_0}{R} q \delta(z) J_1\left(\mu \frac{r}{R}\right) e^{-i\omega t}, \end{aligned} \tag{2.2}$$

where I_0 is the net azimuthal current in the antenna, $J_1(x)$ is a first-order Bessel function, $\mu \approx 3.8$ is the first root of the Bessel function ($J_1(\mu) = 0$), and $q = \dfrac{\mu}{1 - J_0(\mu)} \approx 2.7$.

In the absence of an external magnetic field, the electromagnetic fields described by axisymmetric solutions to Maxwell's equations have three nonzero components:

$$E_\varphi(z, r) = E_\varphi(z) J_1\left(\mu \frac{r}{R}\right), \tag{2.3}$$

$$B_r(z, r) = B_r(z) J_1\left(\mu \frac{r}{R}\right) \text{ and } B_z(z, r) = B_z(z) J_0\left(\mu \frac{r}{R}\right).$$

For a source with the geometry in question, these components satisfy the following set of Maxwell's equations:

$$\begin{aligned} -ic\frac{\partial E_\varphi}{\partial z} + \omega B_r &= 0, \quad \frac{c\mu}{R} E_\varphi - i\omega B_z = 0, \\ \frac{\partial B_r}{\partial z} - \frac{\mu}{R} B_z + i\frac{\omega}{c} D_\varphi &= \frac{4\pi}{c} j_\varphi(z), \end{aligned} \tag{2.4}$$

where we have differentiated the components with allowance for their radial dependence. The azimuthal component of the electric induction, $D_\varphi(z)$, is assumed to be related to the electric field component $E_\varphi(z)$ by an integral relationship that is derived from the kinetic theory of a bounded plasma. Under the conditions of a pronounced anomalous skin effect, in which we are interested here, i.e., when the inequalities

$$\omega_{Le} \gg \omega, \quad L > c/\omega_{Le} \tag{2.5}$$

are satisfied, we can pass over to the limit of a plasma that is semi-infinite in the z direction, assuming that $L \longrightarrow \infty$. If we adopt a model in which the electrons are specularly reflected from the surface $z = 0$, then we obtain (see [1], Sections 17, 18)

$$D_\varphi(z) = \int_{-\infty}^{\infty} dz' \hat{\varepsilon}^{\text{tr}}(z - z', \omega) E_\varphi(z'). \tag{2.6}$$

Here, $\hat{\varepsilon}^{\text{tr}}(z - z', \omega)$ is the influence function, the Fourier transform of which,

$$\varepsilon^{\text{tr}}(\omega, k) = \int dz \hat{\varepsilon}^{\text{tr}}(z, \omega) e^{-ikz}, \tag{2.7}$$

is the transverse dielectric function of an isotropic collisional electron plasma [2],

$$\varepsilon^{\text{tr}}(\omega, k) = 1 - \frac{\omega_{Le}^2}{\omega(\omega + i\nu_e)} J_+\left(\frac{\omega + i\nu_e}{kV_{Te}}\right), \tag{2.8}$$

where $J_+(x) = xe^{\frac{x^2}{2}} \int_{i\infty}^{x} e^{\frac{\tau^2}{2}} d\tau$ (for details about the function $J_+(x)$, see [1, 2]).

Equations (2.4) can readily be reduced to one equation for the electric field component $E_\varphi(z)$ in the plasma region ($z \geq 0$):

$$\frac{\partial^2 E_\varphi}{\partial z^2} - \frac{\mu^2}{R^2} E_\varphi + \frac{\omega^2}{c^2} D_\varphi = -\frac{4\pi i\omega}{c^2} j_\varphi(z), \tag{2.9}$$

where the current density $j_\varphi(z)$ is given by expression (2.2) without the factor $J_1\left(\mu \dfrac{r}{R}\right) e^{-i\omega t}$. We solve this equation by the method described in Sections 17 and 18 of [1]. Specifically, we continue the function $E_\varphi(z)$ into the region $z < 0$ in such a way that the resulting function is even. To do this, we take into account the following boundary conditions, which are a consequence of Eqs. (2.4) themselves:

$$\{E_\varphi(z)\}_{z=0} = 0, \quad \left\{\frac{\partial E_\varphi}{\partial z}(z)\right\}_{z=0} = \frac{\alpha}{R} I_0, \tag{2.10}$$

where $\alpha = \dfrac{4\pi i\omega}{c^2} \dfrac{\mu}{1 - J_0(\mu)}$ and the braces denote the jump in the corresponding quantity at $z = 0$. Without going into the details of the technique for solving the problem at hand, we present the final expression for the field component $E_\varphi(z)$ in the plasma of the source:[2]

$$E_\varphi(z) = -\frac{E'_\varphi(0)}{\pi} \int_{-\infty}^{\infty} dk e^{ikz} \left(k^2 - \frac{\omega^2}{c^2} \varepsilon^{\text{tr}}(\omega, k)\right)^{-1}, \tag{2.11}$$

[2] Note that this way of solving the problem implies that the side metal surface of the source is continued into the vacuum region $z < 0$. This assumption makes it possible to find analytic solution (2.11) and, at the same time, it does not qualitatively change the final results, even if for no other reason than the field is not absorbed in this region.

where

$$E'_\varphi(0) = \frac{-\frac{\alpha}{R}I_0}{1 + \frac{k_0}{\pi}\int\limits_{-\infty}^{\infty} dk\left(k^2 - \frac{\omega^2}{c^2}\varepsilon^{\mathrm{tr}}(\omega, k)\right)^{-1}}, \quad (2.12)$$

with $k_0 = \sqrt{\frac{\mu^2}{R^2} - \frac{\omega^2}{c^2}} \approx \frac{\mu}{R}$ (which refers to the operating frequency $\omega = 8.52 \times 10^7$ s^{-1} of the RF plasma source under consideration).

We can now calculate the RF field power deposited in the plasma of the source and to determine the effective plasma resistance. To do this, we begin with the general expression (2.11), which is valid under the conditions of both weak and strong spatial dispersion, and also take into account the radial dependence of the electric field in the plasma. In this way, we arrive at the following general formula:

$$\mathcal{P}_W = \frac{2\omega}{\pi}|E'_\varphi(0)|^2 \int\limits_0^R r dr J_1^2\left(\mu\frac{r}{R}\right) \times \int\limits_{-\infty}^{\infty} \mathrm{Im}\,\varepsilon^{\mathrm{tr}}(\omega, k)\frac{dk}{\left(k^2 - \frac{\omega^2}{c^2}\varepsilon^{\mathrm{tr}}\right)\left(k^2 - \frac{\omega^2}{c^2}\varepsilon^{\mathrm{tr}*}\right)} \quad (2.13)$$

$$= \alpha^2 I_0^2 \frac{\omega}{2\pi} J_0^2(\mu) \frac{\int\limits_{-\infty}^{\infty} \mathrm{Im}\,\varepsilon^{\mathrm{tr}}(\omega, k)\left|k^2 - \frac{\omega^2}{c^2}\varepsilon^{\mathrm{tr}}\right|^{-2} dk}{\left|1 + \frac{k_0}{\pi}\int\limits_{-\infty}^{\infty} dk\left(k^2 - \frac{\omega^2}{c^2}\varepsilon^{\mathrm{tr}}\right)^{-1}\right|^2} = R_{\mathrm{eff}} I_0^2.$$

From formula (2.13), we can see that the deposited power $\mathcal{P}_W$ depends weakly on the source radius R; in particular, it is essentially independent of R in the range $R > 20$ cm. It can also be seen that, in the range of low plasma densities (when the spatial dispersion is negligible and the RF power dissipation is of a collisional nature), the deposited power increases in proportion to the density n_e; on the other hand, in the range of high plasma densities (under anomalous skin effect conditions), the deposited power decreases gradually according to the law $n_e^{-1/3}$ and the RF power is dissipated through collisionless Cherenkov absorption.

The results of calculations from formula (2.13) are illustrated in Fig. 2, which shows how the effective plasma resistance R_{eff} depends on the plasma density in the range $5 \times 10^{11} \le n_e \le 10^{13}$ cm^{-3} for sources of different radii R. The conclusion that follows from Fig. 2 is rather pessimistic: even for optimum conditions at $\omega \sim \frac{V_{Te}}{c}\omega_{Le}$ (according to this figure, such conditions correspond to sources with $R \ge 20$ cm and $n_e \sim 5 \times 10^{11}$ cm^{-3}), the effective plasma resistance does not exceed 1.5 Ω, which is clearly too low for technological applications.

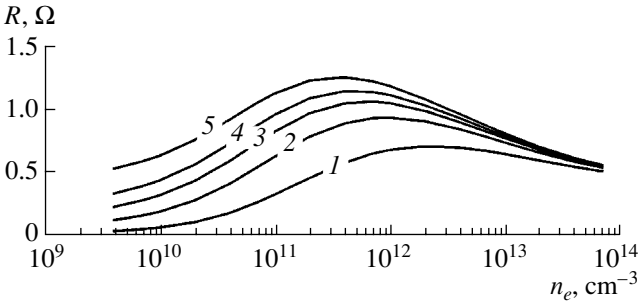

Fig. 2. Dependence of the effective resistance of the plasma on its density for R = (*1*) 5, (*2*) 10, (*3*) 15, (*4*) 20, and (*5*) 30 cm.

3. HELICON PLASMA SOURCES

In this section, we develop an analytic theory of RF plasma sources in an relatively weak external magnetic field. In the literature, such sources are known as helicon sources. The helicon plasma source was first proposed by R.W. Boswell [3] and its theory was first developed by F.F. Chen [4]. However, experimental investigations carried out by Aleksandrov *et al.* [5] failed to provide much support for Chen's theory, as was pointed out in a review by Shamray *et al.* [7] (review articles on plasma sources can be found in [7], which contains a detailed bibliography on the subject). A correct theory of helicon plasma sources was constructed in [8–10]. Here, we will follow those papers in general terms.

We restrict ourselves to elongated helicon plasma sources in which an antenna is positioned at the side surface of the cylinder[3] (see Fig. 1) and that operate with a constant external magnetic field $\mathbf{B}_0$ parallel to the z axis (i.e., $\mathbf{B}_0 \parallel \mathbf{z}$). The frequencies are assumed to satisfy the conditions

$$\nu_e \ll \omega \ll \Omega_e \ll \omega_{Le}, \quad (3.1)$$

which impose lower and upper (for $n_e \le 10^{13}$ cm^{-3}) limits on the magnetic field strength $\mathbf{B}_0$: $20 \ll \mathbf{B}_0 \ll 10^3$ G. The source plasma parameters are assumed to satisfy the conditions

$$\omega \gg \nu_e, \ \omega \gg k_z V_{Te}, \ \ \Omega_e \gg k_\perp V_{Te}, \quad (3.2)$$

[3] We do not consider here planar disk-shaped helicon sources because they have virtually no applications in plasma technologies.

where $k_z = \frac{\pi n}{L}$ ($n = 1, 2, 3, \ldots$) is the longitudinal component of the wave vector and $k_\perp = \frac{\mu_n}{R}$ is its transverse component, with μ_n being the roots of the Bessel function or of its derivative. Under these assumptions, we can describe the plasma by the dielectric tensor [2]

$$\varepsilon_{ij} = \begin{pmatrix} \varepsilon_\perp & ig & 0 \\ -ig & \varepsilon_\perp & 0 \\ 0 & 0 & \varepsilon_\parallel \end{pmatrix}, \tag{3.3}$$

with the elements

$$\varepsilon_\parallel = 1 - \frac{\omega_{Le}^2}{\omega^2}\left(1 - i\frac{\nu_e}{\omega}\right) + i\sqrt{\frac{\pi}{2}}\frac{\omega_{Le}^2\omega}{|k_z|^3 V_{Te}^3}\exp\left(-\frac{\omega^2}{2k_z^2 V_{Te}^2}\right),$$
$$\varepsilon_\perp = 1 + \frac{\omega_{Le}^2}{\Omega_e^2}\left(1 + i\frac{\nu_e}{\omega}\right), \quad g = \frac{\omega_{Le}^2}{\omega\Omega_e}\left(1 + 2i\frac{\omega\nu_e}{\Omega_e^2}\right). \tag{3.4}$$

The ranges and values of the plasma source parameters are the same as those given above, namely, $n_e = 10^{11}$–10^{13} cm^{-3}, $T_e = 5$ eV, $p_0 \approx 10^{-3}$ torr, $R \approx 5$ cm, and $L \approx 10$ cm. It is easy to see that these parameters satisfy conditions (3.1) and (3.2).

In cylindrical coordinates, Maxwell's equations for an axisymmetric low-frequency electromagnetic field in a magnetized plasma reduce to the following two coupled equations for H and E waves, i.e., for the field components B_z and E_z, represented in the form $f(r, z)\exp(-i\omega t)$:

$$\left(\tilde{k}_z^2 + \frac{g^2\omega^2}{\varepsilon_\perp c^2}\right)\Delta_\perp E_z - \hat{\xi}\frac{\varepsilon_\parallel}{\varepsilon_\perp}E_z = \frac{\omega}{c}\frac{g}{\varepsilon_\perp}\Delta_\perp\frac{\partial B_z}{\partial z},$$
$$\tilde{k}_z^2\Delta_\perp B_z - \hat{\xi}B_z = -\frac{\omega}{c}g\Delta_\perp\frac{\partial E_z}{\partial z} - \frac{4\pi}{c}\omega j_\varphi, \tag{3.5}$$

where

$$\Delta_\perp = \frac{1}{r}\frac{\partial}{\partial r}r\frac{\partial}{\partial r}, \quad \tilde{k}_z^2 = -\frac{\partial^2}{\partial z^2} - \varepsilon_\perp\frac{\omega^2}{c^2}, \quad \hat{\xi} = \tilde{k}_z^2 - g\frac{\omega^2}{c^2}.$$

The current density j_φ in an antenna positioned at the side surface of the source (Fig. 1a) is given by the expression

$$j_\varphi = I_0\frac{k_z}{2}\delta(r - R)e^{-i\omega t}\sin k_z z, \tag{3.6}$$

where $k_z = \frac{\pi}{L}$ is the longitudinal wavenumber and I_0 is the net antenna current.

In the general case, Eqs. (3.5) are very difficult to solve because they describe two coupled waves—the so-called E and H waves. It is only in the case of longitudinal propagation in a spatially infinite plasma that these waves are decoupled and are eigenmodes of the oscillations of a magnetized plasma, specifically, transverse eigenmodes (helicons) and longitudinal eigenmodes (Trivelpiece–Gould modes). For a cylindrical source, Eqs. (3.5) can generally be analyzed only numerically (this was done by Aleksandrov *et al.* [11]). However, in the so-called helicon limit, i.e., in the limit of a sufficiently dense plasma and sufficiently strong magnetic field,

$$E_z^h = \frac{ic}{r\omega\varepsilon_\parallel}\frac{\partial}{\partial r}rB_\varphi \longrightarrow 0, \tag{3.7}$$

the set of Eqs. (3.5), in a first approximation, can be split into two independent subsets: one for H waves and one for E waves. The conditions of applicability of limit (3.7) are given by the inequalities

$$\frac{c^2k^2}{\omega_{Le}^2} \ll 1, \quad \frac{\omega}{\Omega_e} < \frac{\omega^2}{c^2k_z^2}\varepsilon_\perp \approx \frac{\omega_{Le}^2\omega^2}{\Omega_e^2c^2k_z^2} \ll 1 \tag{3.8}$$

($k^2 = k_z^2 + k_\perp^2$), which are known as the applicability conditions for the helicon approximation and determine the region of sufficiently strong fields and sufficiently dense plasma. Note that the right-hand part of the second of inequalities (3.8) is the condition for the plasma to be transparent to the helicon field.

Inequalities (3.8) allow us to ignore the term with the field component E_z in the second of Eqs. (3.5) Then, taking into account the relationship

$$B_z = -i\frac{c}{\omega}\frac{1}{r}\frac{\partial}{\partial r}rE_\varphi,$$

we arrive at the following equation for the H wave, i.e., for the helicon field component E_φ^h:

$$\frac{\partial}{\partial r}\frac{1}{r}\frac{\partial}{\partial r}rE_\varphi^h - \left(\tilde{k}_z^2 - \frac{\omega^4g^2}{c^4\tilde{k}_z^2}\right)E_\varphi^h = -\frac{4\pi i\omega}{c^2}j_\varphi. \tag{3.9}$$

It is this equation that will be solved analytically below. Note that the quantity $\tilde{k}_z^2 = k_z^2 - \frac{\omega^2}{c^2}\varepsilon_\perp$ contains a small (second) term that correctly describes the absorption of a helicon field in a plasma because Img is negligibly small.

Hence, in the helicon approximation, we deal with the following situation. An antenna with an azimuthal current of density j_φ excites a purely helicon field (an H wave) in a magnetized dense plasma. This wave then generates a low-frequency quasi-potential E wave (an oblique Langmuir wave, or a Trivelpiece–Gould mode), which is described by the first of Eqs. (3.5). In contrast to the helicon wave (which, under the conditions adopted here, is weakly absorbed by the plasma because of the smallness of Img), the E wave field is

generally dissipated fairly efficiently and thereby heats the plasma.

We solve Eq. (3.9) separately for the region outside the plasma ($r > R$, $j_\varphi = 0$) and for the plasma region ($r < R$, $j_\varphi = 0$). Then, we match the solutions at the plasma surface with the help of the boundary conditions that can be obtained from Eqs. (3.5) by integrating them across an infinitely thin layer around the side surface of the source with allowance for the antenna current:

$$\{E_\varphi^h\}_{r=R} = 0, \quad \left\{\frac{\partial E_\varphi^h}{\partial r}\right\}_{r=R} = \frac{4\pi\omega}{c^2}\frac{k_z}{2}I_0. \tag{3.10}$$

These conditions were derived by using explicit expression (3.6) for the antenna current density at the side surface of the cylinder.

The general solution to Eq. (3.9) inside and outside the plasma region has the form

$$E_\varphi = \begin{cases} C_1 J_1(k_1 r), & r \le R \\ C_2 K_1(k_z r), & r \ge R \end{cases} \tag{3.11}$$

where

$$k_1^2 = \frac{\omega^4 g^2}{c^4 \tilde{k}_z^2} - \tilde{k}_z^2. \tag{3.12}$$

According to boundary conditions (3.10), the coefficients C_1 and C_2 satisfy the equations

$$\begin{aligned} C_1 J_1(k_1 R) - C_2 K_1(k_z R) &= 0, \\ C_1 k_1 J_1'(k_1 R) - C_2 k_z K_1'(k_z R) &= -\frac{2\pi\omega}{c^2} I_0. \end{aligned} \tag{3.13}$$

Resolving these equations, we readily obtain the following expressions for C_1 and C_2:

$$C_1 = -\frac{2\pi\omega k_z}{c^2} I_0 \frac{K_1(k_z R)}{k_1 J_1'(k_1 R) K_1(k_z R) - k_z J_1(k_1 R) K_1'(k_z R)}, \tag{3.14}$$

$$C_2 = -\frac{2\pi\omega k_z}{c^2} I_0 \frac{J_1(k_1 R)}{k_1 J_1'(k_1 R) K_1(k_z R) - k_z J_1(k_1 R) K_1'(k_z R)}. \tag{3.15}$$

Unlike in plasma sources operating without an external magnetic field, in the plasma sources under consideration, this field can excite internal waves within the plasma. The waves so generated are described by the dispersion relation

$$k_1 J_1'(k_1 R) K_1(k_z R) - k_z J_1(k_1 R) K_1'(k_z R) = 0, \tag{3.16}$$

which corresponds to the limit $C_{1,2} \longrightarrow \infty$. These are internal helicon waves satisfying the condition $k_1^2 > 0$. For an elongated plasma source (such that $L \ge 10$ cm, $R \le 5$ cm), this condition enables us to rewrite dispersion relation (3.16) in the form

$$\frac{J_1'(k_1 R)}{J_1(k_1 R)} = \frac{k_z}{k_1}\frac{K_1'(k_z R)}{K_1(k_z R)} \approx -\frac{0.6 k_z}{k_1} \ll 1. \tag{3.17}$$

To a good accuracy, the solutions to dispersion relation (3.17) can be represented as

$$k_1^2 R^2 \approx \pi^2\left(n + \frac{1}{2}\right)^2, \tag{3.18}$$

where $n = 1, 2, 3, \ldots$. Using these solutions, we obtain the following formula for determining the resonant values of the magnetic field (or of the plasma density):

$$\frac{\omega^2 \omega_{Le}^4 R^2}{\Omega_e^2 c^4 k_z^2} \approx \frac{\pi^2 R^2}{L^2} + \pi^2 (n + 1/2)^2. \tag{3.19}$$

Based on inequalities (3.8), we can write the applicability conditions for the helicon approximation in an explicit form:

$$\frac{3\times 10^{12}}{L^2}\left(1 + \frac{L^2}{R^2}\right) \ll n_e \ll 10^{11}\frac{B_0^2}{L^2},$$

$$n_e > \frac{5\times 10^{11} B_0}{L^2},$$

where the magnetic field is expressed in G and the dimensions are given in cm.

In the case of a source with $L = 15$ cm and $R = 5$ cm, these conditions can be satisfied only for sufficiently dense plasmas ($n_e \gg 10^{11}$ cm^{-3}) and sufficiently strong magnetic fields ($B_0 \gg 10$ G). It is also obvious that condition (3.19) for the existence of an internal helicon wave should not go beyond the applicability conditions for the helicon approximation. For the above values of the plasma parameters, this is in fact the case when $n_e > 7\times 10^{11}\frac{B_0}{RL} \ge 4\times 10^{11}$ cm^{-3}.

Thus, under conditions (3.16)–(3.19), i.e., when internal helicon waves can be excited, we arrive at the following expressions for the electric field components in the plasma region $r \le R$:

$$E_\varphi^h = C_1 J_1(k_1 r), \quad E_r^h = \frac{ig\omega^2}{c^2 k_z^2} E_\varphi^h, \tag{3.20}$$

where C_1 is given by formula (3.14).

During the excitation of internal helicon waves in an elongated plasma source, the field components E_φ^h and E_z^h at resonance become fairly large because of the

weak dissipation of the helicon field energy in the plasma. As a result, the helicon field (in particular, its component E_φ^h) begins to excite a low-frequency quasi-potential E wave (a Trivelpiece–Gould mode). To a high accuracy, this E wave is of a potential nature; the potential of its field is determined by Poisson's equation with a source term:

$$\frac{1}{r}\frac{\partial}{\partial r}r\varepsilon_\perp\frac{\partial\Phi}{\partial r} - k_z^2\varepsilon_\parallel\Phi = \frac{ig}{r}\frac{\partial}{\partial r}(rE_\varphi^h). \quad (3.21)$$

The right-hand side of this equation is assumed to be prescribed, so that we deal with a differential equation for oscillations subjected to a driving force. In fact, substituting the field component E_φ^h given by the first of expressions (3.20) into Poisson's equation (3.21) yields the equation

$$\frac{\partial^2\Phi}{\partial r^2} + \frac{1}{r}\frac{\partial\Phi}{\partial r} - k_z^2\frac{\varepsilon_\parallel}{\varepsilon_\perp}\Phi = \frac{ig}{\varepsilon_\perp}k_1C_1J_0(k_1r). \quad (3.22)$$

Solving this equation, we obtain the forced solution

$$\Phi(r) = -\frac{ig}{k_1^2\varepsilon_\perp + k_z^2\varepsilon_\parallel}C_1J_0(k_1r). \quad (3.23)$$

The field components E_z^L and E_r^L of the potential Trivelpiece–Gould mode excited by a helicon wave have the form

$$E_z^L = -\frac{\partial\Phi}{\partial z} = \frac{-gk_1k_z}{k_1^2\varepsilon_\perp + k_z^2\varepsilon_\parallel}C_1J_0(k_1r) \approx \frac{k_1\omega}{k_z\Omega_e}C_1J_0(k_1r),$$

$$E_r^L = -\frac{\partial\Phi}{\partial r} = \frac{igk_1^2}{k_1^2\varepsilon_\perp + k_z^2\varepsilon_\parallel}C_1J_1(k_1r) \quad (3.24)$$

$$\approx -i\left(\frac{k_1\omega}{k_z\Omega_e}\right)^2C_1J_1(k_1r).$$

These expressions show that, along with the helicon resonance, which is described by dispersion relation (3.16), there could, in principle, exist the Trivelpiece–Gould resonance, provided that the following condition is satisfied:

$$k_1^2\varepsilon_\perp + k_z^2\varepsilon_\parallel = 0. \quad (3.25)$$

This is the condition under which a helicon wave can excite internal potential E-waves. Under resonance condition (3.25), the field component E_z^L increases substantially; consequently, the maximum operating efficiency of a plasma source will obviously be achieved under the double resonance condition, i.e., when helicon resonance condition (3.16) and condition (3.25) for the resonant excitation of a potential Trivelpiece–Gould mode are satisfied simultaneously. It should be noted, however, that, for an elongated helicon plasma source for which inequalities (3.8) are satisfied, the second term in condition (3.25) is always much larger than the first term; in other words, in the helicon approximation, the Trivelpiece–Gould resonance is impossible, so that, in such a source, double resonance cannot occur.

In any case, the total field in the plasma is the sum of the helicon and potential fields:

$$E_z = E_z^L, \quad E_r = E_r^h + E_r^L \approx E_r^h, \quad E_\varphi = E_\varphi^h. \quad (3.26)$$

To conclude this section, we briefly discuss the question of the amount of RF field power that is absorbed by the plasma of the source,

$$\mathcal{P}_W = \frac{\omega}{4\pi}\int_0^R d\mathbf{r}\{\mathrm{Im}\,\varepsilon_\parallel|E_z|^2 + \mathrm{Im}\,\varepsilon_\perp|E_r|^2 + \mathrm{Im}\,g(E_zE_\varphi^* - E_\varphi E_z^*)\}. \quad (3.27)$$

The last term in braces in this expression can be ignored because of the smallness of $\mathrm{Im}\,g$. Substituting the explicit expressions for the field components E_z and E_r into formula (3.27) and performing integration in the resulting formula, we finally obtain

$$\mathcal{P}_W = \frac{4\pi^2\omega^2k_z^2I_0^2}{8c^4} \times \frac{\omega R^2LK_1^2(k_zR)}{\left|k_1J_1'(k_1R)K_1(k_zR) - k_zJ_1(k_1R)K_1'(k_zR)\right|^2} \times \left\{\left(\frac{k_1\omega}{k_z\Omega_e}\right)^2\mathrm{Im}\,\varepsilon_\parallel(J_0^2(k_1R) + J_1^2(k_1R)) + \mathrm{Im}\,\varepsilon_\perp\left(1 + \frac{g^2\omega^4}{c^4k_z^2}\right)(J_1^2 + J_2^2 - 2J_0^2J_1^2/k_1R)\right\} \equiv R_{\mathrm{eff}}I_0^2, \quad (3.28)$$

where R_{eff} is the equivalent ohmic resistance of the plasma in the source.

Figures 3–8 show the dependence of the resistance R_{eff} on the magnetic field B_0 for $R = 5$ cm and for different values of L and n_e. In these figures, the solid curves are the corresponding curves from [11] and the dotted curves were calculated from formula (3.28). We can see that, near the helicon resonances, which are given by approximate relationship (3.18), ohmic resistance increases abruptly by more than one order of magnitude. Moreover, the field components that are absorbed most efficiently are the E_r^h component of the helicon wave field and the E_z^L component of the potential field of the Trivelpiece–Gould mode. Note also that the curves calculated in the helicon limit agree qualitatively with those calculated exactly for a plasma trans-

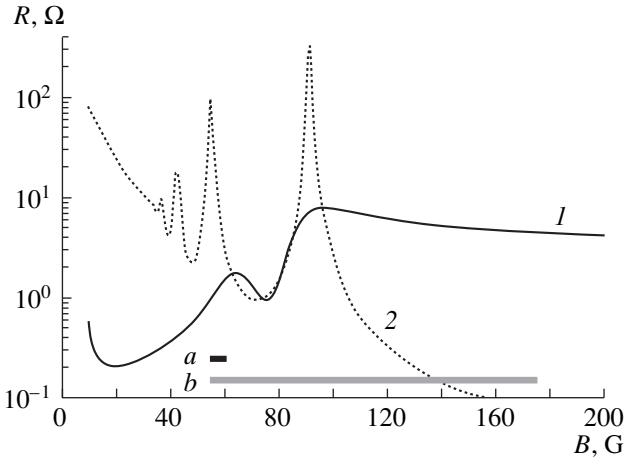

Fig. 3. Dependence of the effective plasma resistance on the magnetic field for $R = 5$ cm, $L = 10$ cm, and $n_e = 10^{12}$ cm^{-3}. Curve *1* is the corresponding curve from [11] and curve *2* was calculated from formula (3.28). Line *a* denotes the plasma region transparent to the helicon field and line *b* indicates the region of applicability of the helicon approximation.

parent to the helicon field. This qualitative agreement concerns the positions of resonances and the magnitudes of resistance at them. The plasma region transparent to the helicon field and the region of applicability of the helicon approximation are shown, respectively, by the black and gray lines at the bottom of each of Figs. 3–8. It should be stressed, however, that the curves obtained from the exact solution are smoother than those calculated from the helicon solution.

The general conclusion of this section can be formulated as follows. The above investigation of analytic solutions for a helicon plasma source in different limiting cases has confirmed the correctness of the numerical solution to the problem that was obtained in [11], according to which elongated helicon plasma sources are capable of operating efficiently over a broad range of plasma parameters both near to and far from the helicon resonances, because the effective plasma resistance in the density range $n_e \sim 10^{11}$–10^{13} cm^{-3} is higher than tens (or even hundreds) of ohms.

4. CYCLOTRON PLASMA SOURCE

In this section, we briefly discuss the prospects for utilizing an RF antenna in an electron cyclotron resonance–based plasma source. As is usual in cyclotron sources, use is made of short-wavelength microwaves in the centimeter range (see [12]). It will be shown, however, that, in sources with a plasma density of $n_e \leq 10^{11}$ cm^{-3}, an RF antenna may operate efficiently at the frequency $f = 13.56$ MHz.

First, note that the analysis of a cyclotron source is very similar to that carried out in Section 2 for a plasma source without a magnetic field. The reason is that the cyclotron wave in a plasma can be treated as if it were propagating in a "quasi-longitudinal" direction, in which case the electromagnetic wave field has the same nonzero components as the wave field considered in the previous section. The only difference is in the expression for the effective dielectric function [2] (cf. expression (2.8)):

$$\varepsilon_{\text{eff}}(\omega, k_z) = 1 - \frac{\omega_{Le}^2}{\omega(\omega + i\nu_e - \Omega_e)} J_+\left(\frac{\omega + i\nu_e - \Omega_e}{k_z V_{Te}}\right). \quad (4.1)$$

It is this expression that should be substituted into formula (2.13), in which, in addition, the integration over k should be replaced by integration over k_z. The results of calculations carried out in this approximation are

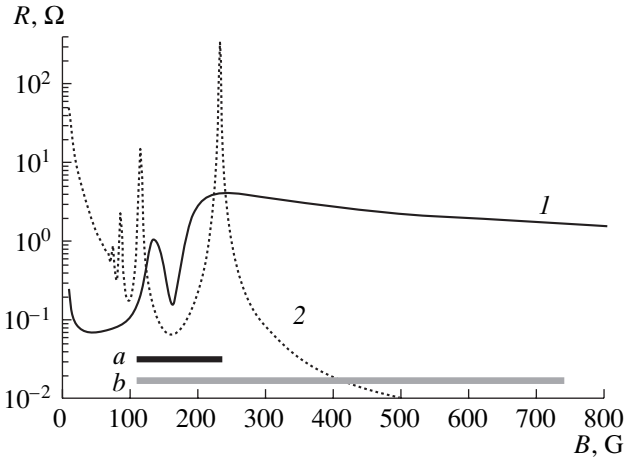

Fig. 4. The same as in Fig. 3, but for $L = 20$ cm.

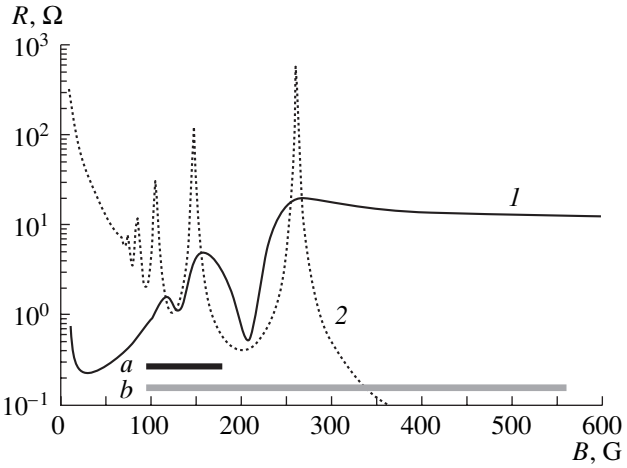

Fig. 5. The same as in Fig. 3, but for $n_e = 3 \times 10^{12}$ cm^{-3}.

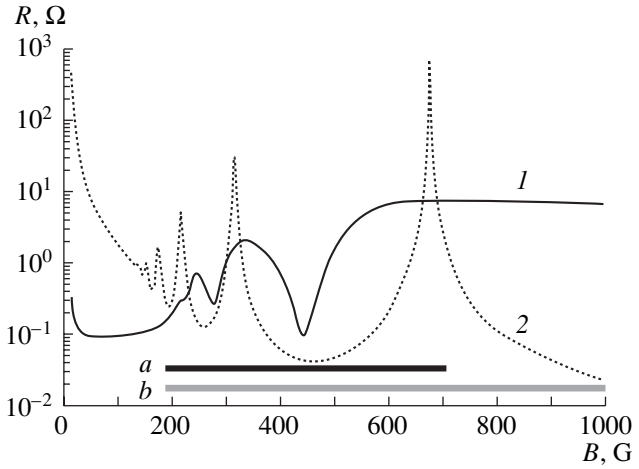

Fig. 6. The same as in Fig. 3, but for L = 20 cm and $n_e = 3 \times 10^{12}$ cm^{-3}.

illustrated in Fig. 9 in the form of the dependence $R_{\text{eff}}(n_e)$ for different values of B_0. We can see that the effective resistance R_{eff}, as a function of plasma density, has a broad peak that is displaced toward stronger magnetic fields as the density increases. This is a consequence of the collective nature of cyclotron waves: the higher the plasma density, the larger the amount by which the frequency of these waves deviates from Ω_e [2],

$$\omega_{\text{res}} = \Omega_e - \frac{\omega_{Le}^2 \Omega_e}{k^2 c^2}. \quad (4.2)$$

Relationship (4.2) implies that the resonant frequency is close to the electron gyrofrequency. Consequently, at a given operating frequency of the source, resonance is achieved only in the range $\Omega_e > \omega$ (i.e., only for $B_0 > 5$ G). At weaker magnetic fields, resonance does not occur, as can be seen from Fig. 9. Note also that expression (4.1) and the results obtained in this section are valid only under conditions corresponding to the quasi-longitudinal propagation of a cyclotron wave and to a small deviation of the resonant frequency from the cyclotron frequency (but when $|\omega - \Omega_e| \gg kV_{Te}$), i.e., under the conditions

$$\frac{\mu^2}{R^2} \ll \frac{\omega_{Le}^2}{c^2} \frac{\omega}{|\omega - \Omega_e|}, \quad \left(\frac{\Omega_e c}{\omega_{Le} V_{Te}}\right)^{1/3} \gg \frac{k^2 c^2}{\omega_{Le}^2} \gg 1. \quad (4.3)$$

For a plasma source with the parameters indicated in Fig. 9, these inequalities impose a lower limit on the allowable plasma density and an upper limit on the allowable external magnetic field.

It is important to emphasize that, according to Fig. 9, the effective plasma resistance is high, $R_{\text{eff}} > 20\ \Omega$, in the plasma density range $n_e \sim (1\text{–}5) \times 10^{10}$ cm^{-3}. This indicates that cyclotron RF sources hold great promise for plasma technology.

To conclude this section, note that the formulas derived here can also be used to describe cyclotron plasma sources operating at higher frequencies such that the vacuum wavelength is greater than the source radius, $\frac{2\pi c}{\omega} > R$, in which case the RF field that is excited by the antenna and maintains the plasma in the source can be described by the above approach. Progressing to higher frequencies and, accordingly, to stronger magnetic fields will make it possible to work with gases at higher pressures, to produce plasmas with higher densities n_e, and to increase the allowable nonuniformity of the magnetic field B_0. In this way, it seems expedient to raise both the frequency ω and magnetic field B_0 by approximately one order of magnitude (i.e., $f \sim$ 50–100 MHz and $B_0 \geq 100$ G), to utilize gases

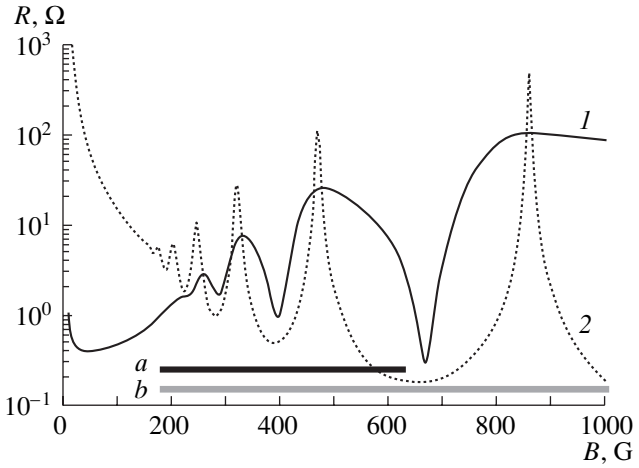

Fig. 7. The same as in Fig. 3, but for $n_e = 10^{13}$ cm^{-3}.

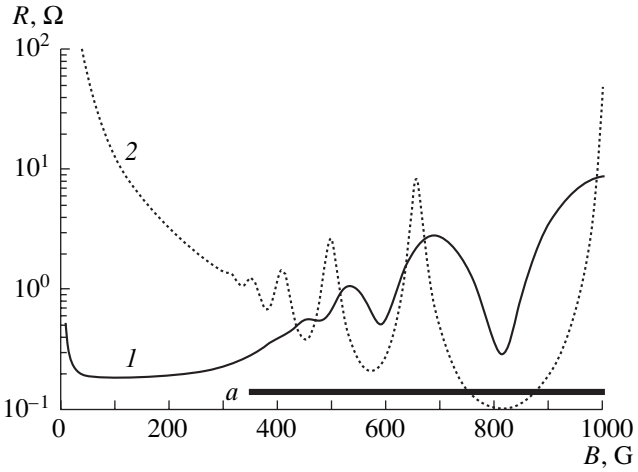

Fig. 8. The same as in Fig. 3, but for L = 20 cm and $n_e = 10^{13}$ cm^{-3}.

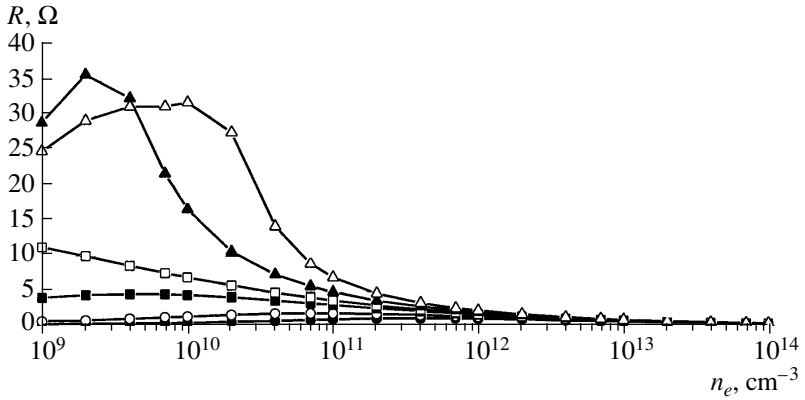

Fig. 9. Plasma resistance vs. plasma density for $R = 30$ cm and for different magnetic field strengths: $B_0 = 0$ G (closed circles), 2 G (open circles), 4 G (closed squares), 5 G (open squares), 7 G (closed triangles), and 9 G (open triangles).

at pressures of $P_0 \sim 10^{-2}$–10^{-1} torr, and thereby to achieve high operating efficiencies at plasma densities of $n_e \sim 10^{12}$–10^{13} cm^{-3}.

5. CONCLUSIONS

Summarizing the results of the above analytic study of inductive RF plasma sources, we can draw the following conclusions.

(i) Inductive RF plasma sources without an external magnetic field hold little promise for technological applications. Because of the pronounced skin effect, the only sources that can be of interest from a practical standpoint are planar disk-shaped sources, in which, even under optimum conditions ($R > 20$ cm, $n_e \sim 10^{11}$ cm^{-3}), the effective resistance of the plasma column is $\leq 1.5\ \Omega$. Consequently, such sources can operate efficiently only with antennas whose resistance is lower than $1\ \Omega$.

(ii) In contrast, elongated helicon RF plasma sources and planar disk-shaped ones (with a length of $L \geq 5$–10 cm) are far more efficient: over a broad density range ($n_e \sim 10^{11}$–10^{13} cm^{-3}) and at magnetic fields of $B_0 \sim 100$–200 G, the effective plasma resistance in the regions of helicon resonances is higher than tens of ohms, which provides efficient operation with almost all types of inductive antennas. It should be emphasized that, in helicon sources, the effective plasma resistance is governed not only by the absorption of the antenna-generated helicon wave but also by the absorption of the longitudinal wave (the Trivelpiece–Gould mode), which is excited in the plasma by the helicon field. In this case, the helicon field and the field of the Trivelpiece–Gould mode are of comparable importance.

(iii) An unexpected result is the efficient operation of cyclotron RF sources working under conditions of a broad resonance at plasma densities of $(1–5) \times 10^{10}$ cm^{-3} in a weak magnetic field ($5 < B_0 < 10$ G). The effective plasma resistance in planar disk-shaped cyclotron sources exceeds 20–30 Ω, so that choosing the type of an inductive antenna presents no problem.

ACKNOWLEDGMENTS

We are grateful to E.A. Kral'kina for numerous discussions of the results obtained. We also thank our anonymous referees for their valuable remarks.

REFERENCES

1. V. P. Silin and A. A. Rukhadze, *Electromagnetic Properties of Plasma and Plasma-Like Media* (Atomizdat, Moscow, 1961).
2. A. F. Alexandrov, L. S. Bogdankevich, and A. A. Rukhadze, *Principles of Plasma Electrodynamics* (Vysshaya Shkola, Moscow, 1988; Springer-Verlag, Berlin, 1984).
3. R. W. Boswell, Plasma Phys. Controlled Fusion **26**, 1147 (1984).
4. F. F. Chen, Plasma Phys. Controlled Fusion **33**, 339 (1991); F. F. Chen and G. Chelavier, J. Vac. Sci. Technol. A **10**, 1389 (1992).
5. A. F. Alexandrov, G. E. Bugrov, E. A. Kralkina, *et al.*, in *Proceedings of the 22nd International Conference on Phenomena in Ionized Gases, New-Jersy, 1995*, Vol. 4, p. 153; in *Proceedings of the 25th International Conference on Phenomena in Ionized Gases, Nagoya, 2002*, Vol. 3, p. 33.
6. K. P. Shamray, A. F. Alexandrov, E. A. Kralkina, *et al.*, J. Phys. III **10** (Suppl.), C4365 (1997); in *Proceedings of the 23rd International Conference on Phenomena in Ionized Gases, Touluse, 1997*.
7. *High Density Plasma Sources*, Ed. by O. A. Popov (Noyes, New Jersey, 1995).
8. N. F. Vorob'ev and A. A. Rukhadze, Fiz. Plazmy **20**, 1065 (1994) [Plasma Phys. Rep. **20**, 955 (1994)].
9. A. F. Aleksandrov, N. F. Vorob'ev, E. A. Kral'kina, *et al.*, Zh. Tekh. Fiz. **64** (11), 53 (1994) [Tech. Phys. **39**, 1118 (1994)].
10. A. F. Aleksandrov, G. E. Bugrov, E. A. Kral'kina, *et al.*, Prikl. Fiz., No. 1, 3 (1995).
11. A. F. Alexandrov, G. E. Bugrov, E. A. Kralkina, *et al.*, J. Russ. Laser Res. **24**, 301 (2003).
12. *Electron Cyclotron Emission and Electron Heating*, Ed. by G. Giruzzi (World Scientific, Paris, 2002).

Translated by I.A. Kalabalyk

Plasma Physics Reports, Vol. 30, No. 8, 2004, pp. 698–709. Translated from Fizika Plazmy, Vol. 30, No. 8, 2004, pp. 750–762.

NONLINEAR PHENOMENA

Excitation of Magnetic Fields by a Circularly Polarized Laser Pulse in a Plasma Channel

A. A. Frolov

Institute for High Energy Densities, Associated Institute for High Temperatures, Russian Academy of Sciences, Izhorskaya ul. 13/19, Moscow, 125412 Russia

Received November 4, 2003

Abstract—The excitation of quasistatic magnetic fields by a circularly polarized laser pulse in a plasma channel is considered. It is shown that, to second order in the amplitude of the electric field of the laser pulse, circular rotation of the plane of polarization of the laser radiation in a radially nonuniform plasma gives rise to a nonlinear azimuthal current and leads to the excitation of the radial and axial components of the magnetic field. The dependence of the magnetic field distribution over the plasma channel on the spatial dimensions of the pulse and on the channel width is investigated for a moderate-power laser pulse. The structure of the magnetic fields excited by a relativistic laser pulse in a wide plasma channel is analyzed. © *2004 MAIK "Nauka/Interperiodica".*

INTRODUCTION

As early as 1960, L.P. Pitaevskiĭ [1] predicted the effect of the magnetization of a medium by a circularly polarized electromagnetic field. This phenomenon, which is associated with the excitation of the axial component of the magnetic field during the propagation of circularly polarized electromagnetic radiation in a medium, was called the inverse Faraday effect (IFE), as opposed to the conventional Faraday effect—the rotation of the plane of polarization of an electromagnetic wave propagating along a constant magnetic field. Somewhat later, magnetization induced by a circularly polarized electromagnetic radiation was observed experimentally in paramagnetic crystals, diamagnetic glasses, and inorganic and organic liquids [2–4]. After the magnetization effect was revealed experimentally in a laboratory plasma [5], theoretical papers appeared in which the excitation of quasistatic magnetic fields in the field of a circularly polarized electromagnetic wave of constant amplitude was investigated using different approaches: macroscopic [6], quantum-mechanical [7], and hydrodynamic [8–10]. Recent advances in the generation of subpicosecond terawatt laser pulses have added to further interest in the IFE. Experimental investigations have been carried out on the excitation of an axial magnetic field in a plasma produced during the irradiation of solid-state and gaseous targets by circularly polarized laser pulses of moderate [11, 12] and relativistic [13] intensities, including the measurement of the magnetic field strength. There also appeared a large number of theoretical papers devoted to a description of the IFE effect for relativistically strong laser radiation [14–26]. In the literature, however, the data on the strength of the axial magnetic field at moderate and relativistic intensities of radiation fluxes are contradictory. Thus, according to the results presented in [14, 15], in the interaction of a circularly polarized nonrelativistic laser light with a homogeneous plasma, the strength of the axial magnetic field is proportional to the square of the laser field amplitude. More detailed investigations [16, 17] showed that the strength of the axial magnetic field in an initially homogeneous plasma irradiated by a low-energy radiation flux is proportional to the fourth power of the laser field amplitude, so that, in [14, 15], the axial magnetic field was greatly overestimated. The strength of the axial magnetic field is proportional to the squared amplitude of a low-intensity laser field only when the density distribution of the plasma electrons in a plane transverse to the propagation direction of the laser radiation is nonuniform. In [8, 9], it was shown that this is indeed the case for a circularly polarized electromagnetic wave of constant amplitude. As was already mentioned, the data on the axial magnetic field strength at relativistic laser intensities are also contradictory. In [13, 25], it was predicted that the magnetic field strength should increase linearly with the laser field amplitude. A logarithmic dependence of the strength of the axial magnetic field on the laser intensity was predicted in [15]. However, most authors [14, 18–20, 24] have arrived at the conclusion that the magnetic field strength should saturate at relativistic amplitudes of the laser field. In [13, 22], along with the conventional mechanism for the excitation of magnetic fields under IFE conditions (which is associated with the generation of an azimuthal current by a circularly polarized electromagnetic wave), another possible mechanism was discussed: the generation of axial magnetic fields by the betatron oscillations of fast electrons in a plasma channel. A strongly nonlinear regime of the excitation of the axial magnetic field during the self-focusing and channeling of a circularly polarized long relativistic laser pulse in a plasma was investigated numerically by Kim *et al.* [24]. In [25], Zhu *et al.* applied the kinetic model developed in

1063-780X/04/3008-0698$26.00

their earlier work [26] to explain the experimental results of Najmudin *et al.* [13] and also discussed the influence of suprathermal electrons on the strength of the axial magnetic field.

The present paper is devoted to an analytic study of the excitation of quasistatic magnetic fields by a circularly polarized laser pulse in a plasma channel with a radially nonuniform electron density distribution. The analysis that follows is based on the relativistic hydrodynamic equations for a cold plasma. The main objective of the paper is to generalize the results obtained in [9] in studying a circularly polarized electromagnetic wave of constant amplitude to the case of an arbitrary dependence of the laser field amplitude on the spatial coordinates. It is shown that, when the radial nonuniformity of the electron density and the finite spatial dimensions of a laser pulse are taken into account, circular rotation of the plane of polarization of the laser radiation gives rise to a nonlinear azimuthal current and generates the radial and axial magnetic field components, which, in a weakly relativistic approximation, are proportional to the second power of the laser field amplitude. This result differs radically from the one obtained for the interaction of a circularly polarized laser pulse with an initially homogeneous plasma, in which case the strength of the magnetic fields is proportional to the fourth power of the laser field amplitude [16, 17]. Another objective of the present paper is to examine in detail how the distribution of the magnetic field components over the plasma channel depends on the spatial dimensions and intensity of the plasma pulse and on the channel width. The spatial structures of the azimuthal current and axial magnetic field are investigated as functions of the plasma channel width for long laser pulses of moderate intensity. It is shown that a long laser pulse propagating in a wide plasma channel whose width considerably exceeds the plasma wavelength gives rise to two annular current layers, in which the currents flow in opposite directions. In this case, the axial magnetic field is analogous to that produced by two long coaxial solenoids: it is maximum at the channel axis, falls off to zero with distance from the axis, and then reverses its direction. For a moderate-intensity long laser pulse propagating in a narrow plasma channel whose width is less than the plasma wavelength, the axial magnetic field is maximum at the channel axis and decreases to zero away from the axis, but does not reverse its direction. In these circumstances, only one annular current layer arises in the plasma channel and the magnetic field is similar to that produced by a long solenoid. It is found that, when the finite length of the laser pulse is taken into account, the magnetic field acquires additional (radial and azimuthal) components. For a moderate-intensity laser pulse with spatial dimensions greater than the plasma wavelength, the condition is derived under which the radial and axial magnetic field components associated with the circular rotation of the plane of polarization of the laser radiation substantially exceed the azimuthal magnetic field component—the only one excited by a linearly polarized laser pulse. Under this condition, the spatial distribution of the magnetic field is investigated and the pattern of the magnetic field lines is outlined. It is shown that the spatial distribution of the magnetic field is then similar to that produced by a solenoid of finite length and that the laser pulse itself resembles a magnetic dipole traveling at the speed of light. The propagation of a relativistic laser pulse with large spatial dimensions in a wide plasma channel is investigated. It is shown that, for a relativistically strong radiation, the radial and axial magnetic fields are linearly proportional to the laser field amplitude and occur on spatial scales that exceed the laser pulse dimensions by a factor of $\sqrt{2}$.

1. BASIC EQUATIONS

We consider a plasma channel in which the electron density $N_e(r)$ depends only on the radial coordinate $r = \sqrt{x^2 + y^2}$ and assume that a circularly polarized laser pulse propagates along the channel axis (the z axis). The electric field of the pulse has the form

$$\mathbf{E}_L(\mathbf{r}, t) = \frac{1}{2}\exp(-i\omega_0 t + ik_0 z) \times \left\{\mathbf{e}_x + i\lambda\mathbf{e}_y + \frac{i\mathbf{e}_z}{k_0}\left(\frac{\partial}{\partial x} + i\lambda\frac{\partial}{\partial y}\right)\right\}E_0(r, \xi) + \text{c.c.} \quad (1.1)$$

Here, ω_0 and k_0 are the laser carrier frequency and laser wavenumber, respectively; $E_0(r, \xi)$ is the laser field amplitude, which is assumed to vary slowly with time (on the time scale ω_0^{-1}) and space (on the spatial scale k_0^{-1}); $\xi = z - V_g t$ is the longitudinal coordinate in a frame of reference comoving with the pulse; $V_g = c^2 k_0/\omega_0$ is the laser pulse group velocity; c is the speed of light; $\mathbf{e}_x$, $\mathbf{e}_y$, and $\mathbf{e}_z$ are unit vectors along the axes of a Cartesian coordinate system; and the quantity λ, which characterizes the rotation of the plane of polarization of the laser pulse, takes on the values $\lambda = \pm 1$, corresponding to the left-hand ($\lambda = 1$) and right-hand ($\lambda = -1$) polarized laser radiation. That the electric field of the laser pulse has a component along the z axis stems from the fact that laser radiation is a transverse electromagnetic field.

In order to investigate the generation of quasistatic magnetic fields by laser field (1.1) in a plasma channel, we turn to the following relativistic hydrodynamic equation for the averaged (over high-frequency laser oscillations) electron momentum $\mathbf{p}(\mathbf{r}, t)$ in a cold plasma (see, e.g., [14, 16]):

$$\frac{\partial}{\partial t}\mathbf{p} = e\mathbf{E} - m_e c^2 \nabla\gamma. \quad (1.2)$$

We also use Maxwell's equations for the quasistatic electric and magnetic fields, $\mathbf{E}(\mathbf{r}, t)$ and $\mathbf{B}(\mathbf{r}, t)$:

$$\nabla \times \mathbf{E} = -\frac{1}{c}\frac{\partial}{\partial t}\mathbf{B}, \tag{1.3}$$

$$\nabla \times \mathbf{B} = \frac{1}{c}\frac{\partial}{\partial t}\mathbf{E} + \frac{4\pi e}{m_e c\gamma}N_e(r)\mathbf{p} + \frac{4\pi}{c}\mathbf{j}_E, \tag{1.4}$$

$$\nabla \times \mathbf{p} + \frac{e}{c}\mathbf{B} = 0, \tag{1.5}$$

where e and m_e are the charge and mass of an electron. Equations (1.2)–(1.5) are written in the linear approximation in slowly varying quantities. In these equations, the influence of the laser pulse is taken into account through the relativistic factor γ, which, for circularly polarized laser field (1.1), has the form

$$\gamma = \sqrt{1 + \frac{e^2 E_0^2(r, \xi)}{m_e^2 \omega_0^2 c^2}}, \tag{1.6}$$

and also through the nonlinear current density $\mathbf{j}_E = e\langle \delta N_L \cdot \mathbf{V}_L \rangle$, which contains the averaged (over the high-frequency laser oscillations) product of the rapidly varying electron velocity $\mathbf{V}_L$ and the high-frequency electron density variation δN_L. Using the continuity equation

$$\frac{\partial}{\partial t}\delta N_L + \nabla \cdot (N_e(r)\mathbf{V}_L) = 0$$

and the equation for the electron momentum $\mathbf{p}_L = \gamma m_e \mathbf{V}_L$ in the laser field,

$$\frac{\partial}{\partial t}\mathbf{p}_L = e\mathbf{E}_L,$$

we obtain the following expressions for the rapidly varying perturbations of the electron density and electron velocity in an underdense plasma, $\omega_0 \gg \omega_p(r)$:

$$\delta N_L(\mathbf{r}, t) = \frac{eE_0(r, \xi)}{2m_e\omega_0^2}\exp(-i\omega_0 t + ik_0 z)$$

$$\times\left(\frac{\partial}{\partial x} + i\lambda\frac{\partial}{\partial y}\right)\left\{\frac{N_e(r)}{\gamma}\right\} + \text{c.c.},$$

$$\mathbf{V}_L(\mathbf{r}, t) = \frac{ie}{2m_e\omega_0\gamma}\exp(-i\omega_0 t + ik_0 z)$$

$$\times\left\{\mathbf{e}_x + i\lambda\mathbf{e}_y + \frac{i\mathbf{e}_z}{k_0}\left(\frac{\partial}{\partial x} + i\lambda\frac{\partial}{\partial y}\right)\right\}E_0(r, \xi) + \text{c.c.},$$

where $\omega_p(r) = \sqrt{\frac{4\pi e^2 N_e(r)}{m_e}}$ is the local plasma frequency.

Using these formulas, we find that the nonlinear current density $\mathbf{j}_E = j_E\mathbf{e}_\varphi$ has only the azimuthal component j_E. Under the condition $\omega_0 \gg \omega_p(r)$, this component satisfies the relationship

$$j_E = -\frac{\lambda e^3 E_0^2(r, \xi)}{2m_e^2\omega_0^3\gamma}\frac{\partial}{\partial r}\left(\frac{N_e(r)}{\gamma}\right), \tag{1.7}$$

where $\mathbf{e}_\varphi$ is a unit vector in the azimuthal direction. This relationship implies that the nonlinear current density $\mathbf{j}_E$ is directly related to the circular rotation of the plane of polarization, so that it vanishes for a linearly polarized ($\lambda = 0$) laser pulse. Relationship (1.7) is a generalization of the corresponding relationship obtained in [9] (in studying a circularly polarized constant-amplitude electromagnetic wave) to the case of an arbitrary dependence of the electric field amplitude $E_0(r, \xi)$ on the spatial coordinates.

Eliminating the electric and magnetic fields in Eqs. (1.2)–(1.5), we reduce them to a single equation that describes slow time variations of the electron momentum:

$$\left\{\frac{\partial^2}{\partial\xi^2} + \frac{k_p^2(r)}{\gamma}\right\}\mathbf{p} + \nabla \times (\nabla \times \mathbf{p}) = -\frac{4\pi e}{c^2}\mathbf{j}_E + m_e V_g\frac{\partial}{\partial\xi}\nabla\gamma, \tag{1.8}$$

where $k_p(r) = \frac{\omega_p(r)}{c}$ is the local plasma wavenumber.

If Eq. (1.8) is solved, then the quasistatic electric and magnetic fields generated by a laser pulse in a plasma channel can be calculated from relationships (1.2) and (1.5). Note that, when intense laser light irradiates a plasma, it gives rise to low-frequency electron density perturbations $\delta N_e(\mathbf{r}, t)$, which are described by the equation

$$\frac{\delta N_e}{N_e(r)} = \frac{1}{k_p^2(r)}\Delta\gamma - \frac{V_g}{4\pi e^2 N_e(r)}\frac{\partial}{\partial\xi}\nabla \cdot \mathbf{p}. \tag{1.9}$$

In deriving expression (1.7) for the nonlinear current, as well as in writing Eqs. (1.4) and (1.8), the density perturbations were assumed to be small and, accordingly, were ignored. This assumption corresponds to a linear approximation in the slowly varying quantities and is valid under the condition $\delta N_e \ll N_e(r)$. In expression (1.6) for the relativistic factor, the contribution of the slow electron motion is also ignored, which is valid under the condition $p_E^2 \gg \mathbf{p}^2$, where $p_E = eE_{0L}/\omega_0$ is the momentum of an electron in the laser field.

In accordance with formulas (1.6) and (1.7), Eq. (1.8) implies that the electron momentum has three

nonzero components, p_r, p_z, and p_φ, which are described by the equations

$$\frac{\partial^2 p_z}{\partial r \partial \xi} + \frac{k_p^2(r)}{\gamma} p_r = m_e c \frac{\partial^2 \gamma}{\partial r \partial \xi}, \tag{1.10}$$

$$\left[\frac{\partial^2}{\partial \xi^2} + \frac{k_p^2(r)}{\gamma}\right] p_z + \frac{1}{r}\frac{\partial}{\partial r} r\left(\frac{\partial p_r}{\partial \xi} - \frac{\partial p_z}{\partial r}\right) = m_e c \frac{\partial^2 \gamma}{\partial \xi^2}, \tag{1.11}$$

$$\frac{k_p^2(r)}{\gamma} p_\varphi - \frac{\partial}{\partial r}\frac{1}{r}\frac{\partial}{\partial r}(r p_\varphi) = -\frac{4\pi e}{c^2} j_E. \tag{1.12}$$

In deriving Eqs. (1.10) and (1.12), the group velocity of the laser pulse was assumed to be equal to the speed of light. This assumption is justified in view of the above condition $\omega_0 \gg \omega_p(r)$, which indicates that the plasma density is low.

According to formula (1.5), the radial and longitudinal components of the electron momentum, p_r and p_z, give rise to the azimuthal component of the magnetic field:

$$B_\varphi = \frac{c}{e}\left(\frac{\partial p_z}{\partial r} - \frac{\partial p_r}{\partial \xi}\right), \tag{1.13}$$

while the electron momentum component p_φ is responsible for the generation of the radial and axial magnetic field components, B_r and B_z:

$$B_r = \frac{c}{e}\frac{\partial p_\varphi}{\partial \xi}, \tag{1.14}$$

$$B_z = -\frac{c}{e}\frac{1}{r}\frac{\partial}{\partial r}(r p_\varphi) \tag{1.15}$$

From Eqs. (1.10)–(1.12) and relationships (1.6), (1.7) and (1.13)–(1.15), it follows that a linearly polarized laser pulse ($\lambda = 0$) excites only the azimuthal magnetic field B_φ in a plasma channel. The magnetic field excited by a circularly polarized laser pulse ($\lambda = \pm 1$) has three nonzero components, B_r, B_z, and B_φ, two of which—the radial (B_r) and axial (B_z) components—are completely governed by the circular rotation of the plane of polarization of the laser radiation.

In what follows, we will consider the propagation of a laser pulse in a plasma channel with a parabolic electron density profile,

$$N_e(r) = N_{0e}\left(1 + \frac{r^2}{R_{\rm ch}^2}\right), \tag{1.16}$$

where $R_{\rm ch}$ is the channel radius and N_{0e} is the electron density at the channel axis. We assume that the pulse is Gaussian in shape,

$$E_0(r, \xi) = E_{0L}\exp\left(-\frac{r^2}{2R_L^2} - \frac{\xi^2}{2L^2}\right), \tag{1.17}$$

where E_{0L} is the maximum amplitude of the electric field of the laser radiation and R_L and L are the radius of the pulse and its length. A laser pulse that has a moderate intensity such that the electron oscillatory velocity $V_E = eE_{0L}/(m_e\omega_0)$ in the laser field is much lower than the speed of light, $V_E \ll c$, and whose power does not exceed the critical power required for self-focusing,

$$\frac{V_E^2}{c^2} \ll \frac{1}{k_{p0}^2 R_L^2}, \tag{1.18}$$

can be consistent with the plasma channel under the condition

$$\frac{R_{\rm ch}}{R_L} = k_{p0} R_L, \tag{1.19}$$

where $k_{p0} = k_p$ ($r = 0$) is the plasma wavenumber at the channel axis. In this case, the transverse diffractive spreading of the laser pulse is prevented by the focusing effect of the plasma channel, and the propagating pulse keeps its radius unchanged [27–29].

2. SPATIAL DISTRIBUTION OF THE MAGNETIC FIELD EXCITED BY A MODERATE-INTENSITY LONG LASER PULSE IN A PLASMA CHANNEL

Let a moderate-intensity ($V_E \ll c$) laser pulse with a low power satisfying condition (1.18) and with a great length ($k_{p0}L \longrightarrow \infty$) propagate under consistency condition (1.19) in a plasma channel with an electron density profile in the form of (1.16). In this case, according to relationships (1.7) and (1.10)–(1.15), the pulse gives rise only to the azimuthal electron momentum component p_φ and to the axial magnetic field B_z, which, to second order in the laser field amplitude, is described by the equation

$$\begin{aligned} &B_z - \frac{1}{r}\frac{\partial}{\partial r}\frac{r}{k_p^2(r)}\frac{\partial}{\partial r} B_z \\ &= -\frac{\lambda e c}{2 m_e \omega_0^3}\frac{1}{r}\frac{\partial}{\partial r}\left(E_0^2(r)\frac{r}{N_e(r)}\frac{\partial}{\partial r} N_e(r)\right), \end{aligned} \tag{2.1}$$

where $E_0(r) = \lim\limits_{L\to\infty} E_0(r, \xi) = E_{0L}\exp\left(-\dfrac{r^2}{2R_L^2}\right)$.

Note that, according to Eq. (2.1), it is only for a channel with a radially nonuniform electron density distribution that the magnetic field strength is proportional to the squared amplitude of the electric field of

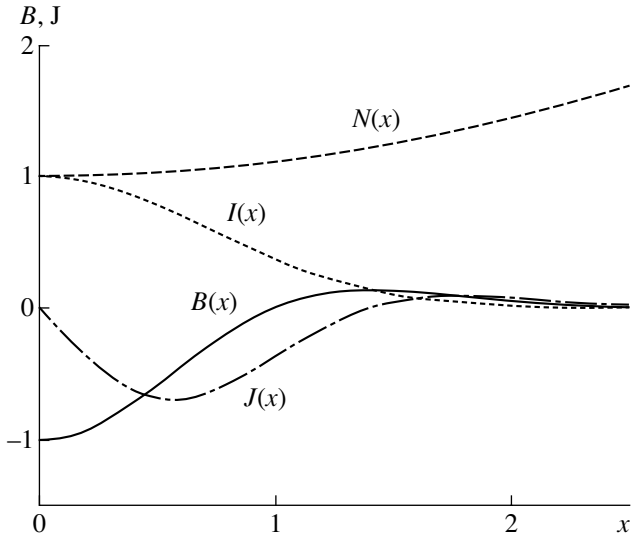

Fig. 1. Spatial profiles of the normalized magnetic field $B = B_z \frac{m_e \omega_0^3 R_{ch}^2}{2\lambda ec E_{0L}^2}$, normalized current density $J = j_\varphi \frac{m_e^2 \omega_0^3 k_{p0}^2 R_{ch}^2 R_L}{4\lambda e^3 E_{0L}^2 N_{0e}}$, normalized laser intensity $I = E_0^2(r)/E_{0L}^2$, and normalized electron density $N = N_e(r)/N_{0e}$ along the dimensionless transverse coordinate $x = r/R_L$ for a circularly polarized long ($k_{p0}L \longrightarrow \infty$) laser pulse propagating in a wide plasma channel ($R_{ch} = 3R_L$).

the laser pulse. For a spatially homogeneous plasma channel, the strength of the laser-generated quasistatic magnetic field is proportional to the fourth power of the laser field amplitude [16, 17].

Equation (2.1) can be readily solved in the two limiting cases: a wide laser pulse ($k_{p0}R_L \gg 1$) and a narrow laser pulse ($k_{p0}R_L \ll 1$). For a wide pulse ($k_{p0}R_L \gg 1$), the second term on the left-hand side of Eq. (2.1) is small and the radial profile of the magnetic field in the plasma channel is described by the expression

$$B_z = -\frac{\lambda ec}{2m_e\omega_0^3}\frac{1}{r}\frac{\partial}{\partial r}\left(E_0^2(r)\frac{r}{N_e(r)}\frac{\partial}{\partial r}N_e(r)\right). \quad (2.2)$$

This expression agrees with the corresponding expression obtained in [9] in studying the excitation of the axial magnetic field component by a circularly polarized constant-amplitude electromagnetic wave in a radially inhomogeneous plasma.

We substitute formula (1.16) for the electron density profile in the plasma channel into expression (2.2) and take into account the radial dependence $E_0(r)$ of the laser field amplitude. As a result, we arrive at the following explicit expression for the spatial structure of the magnetic field:

$$B_z = -\frac{2\lambda ec E_{0L}^2}{m_e\omega_0^3 R_{ch}^2}\left(1-\frac{r^2}{R_L^2}\right)\exp\left(-\frac{r^2}{R_L^2}\right). \quad (2.3)$$

Expression (2.3) was derived using consistency condition (1.9), which, for a wide laser pulse ($k_{p0}R_L \gg 1$) leads to the inequality $R_{ch} \gg R_L$. This radial profile of the magnetic field is governed by the total quasistatic azimuthal current with the density

$$j_\varphi = j_E + \frac{eN_e(r)}{m_e\gamma}p_\varphi. \quad (2.4)$$

The expression for this current density follows from Eq. (1.12) and relationship (1.7). In the nonrelativistic limit ($V_E \ll c$), and under the condition $k_{p0}R_L \gg 1$, it has the form

$$j_\varphi = \frac{\lambda e^3}{2m_e^2\omega_0^3}\frac{\partial}{\partial r}\frac{1}{r}\frac{\partial}{\partial r}\left(E_0^2(r)\frac{r}{k_p^2(r)}\frac{\partial}{\partial r}N_e(r)\right). \quad (2.5)$$

Expression (2.5) describes the total azimuthal current excited by a wide laser pulse in a plasma channel. This current turns out to be substantially lower than nonlinear current (1.7). The reason lies in the partial neutralization of the nonlinear current j_E and the current $\frac{eN_e(r)}{m_e}p_\varphi$, which is carried by the slow electrons. In fact, in the zeroth approximation, Eq. (1.12) in which the terms with small radial derivatives are ignored yields $j_E + \frac{eN_e(r)}{m_e}p_\varphi = 0$. This relationship corresponds to the condition for the total current to vanish, $j_\varphi = 0$. It is only in the first approximation that taking small radial derivatives into account in Eq. (1.12) leads to expression (2.5), in which case the total azimuthal current density is estimated by $j_\varphi \cong \frac{j_E}{k_{p0}^2R_L^2} \ll j_E$.

With allowance for the pulse shape and electron density profile in the plasma channel, we obtain from formula (2.5) the radial dependence of the current density:

$$j_\varphi = -\frac{4\lambda e^3 N_{0e}E_{0L}^2}{m_e^2\omega_0^3k_{p0}^2R_{ch}^2}\frac{r}{R_L^2}\left(2-\frac{r^2}{R_L^2}\right)\exp\left(-\frac{r^2}{R_L^2}\right). \quad (2.6)$$

Radial profiles of the axial magnetic field (2.3) and the total azimuthal current density (2.6) in a wide plasma channel are shown in Fig. 1. The magnetic field is strongest at the channel axis $r = 0$. As r increases, the magnetic field strength decreases. At $r = R_L$, the magnetic field vanishes and, at $r > R_L$, it points in the opposite direction. This magnetic field structure in a plasma channel is governed by the onset of two annular current

layers, in which the currents flow in opposite directions, and is similar to the field structure produced by two long coaxial solenoids. Since the current in the inner layer is stronger, it determines the direction and strength of the magnetic field in the axial region. The effect of the outer layer is less significant because of the lower current density. The larger the distance from the axis, the weaker the effect of the inner current layer. (This situation is similar to that with a solenoid, outside of which the magnetic field is weak.) At large distances from the axis, the direction of the magnetic field and its strength are governed by the outer layer, in which the current density is relatively low and the current flows in the direction opposite to that of the current in the inner layer. As a result, the magnetic field far from the axis of the plasma channel reverses its direction and is weaker than that in the axial region.

For a narrow laser pulse ($k_{p0}R_L \ll 1$), we obtain from Eq. (2.1) the relationship

$$\frac{\partial}{\partial r}B_z = \frac{\lambda ecE_0^2(r)}{2m_e\omega_0^3}\frac{\partial}{\partial r}k_p^2(r). \quad (2.7)$$

Using this relationship and taking into account the radial dependence of the laser field amplitude $E_0(r)$ and electron density profile (1.16), we can determine the spatial distribution of the magnetic field in the plasma channel:

$$B_z = -\frac{\lambda ecE_{0L}^2}{2m_e\omega_0^3R_L^2}\exp\left(-\frac{r^2}{R_L^2}\right). \quad (2.8)$$

The expression for the total azimuthal current that excites the magnetic field (2.8) in a narrow plasma channel follows from Eq. (1.12) in the nonrelativistic approximation under the condition $k_{p0}R_L \ll 1$. In this case, we find that the nonlinear current is considerably higher than the current carried by the slow electrons, $j_\varphi \cong j_E \gg \frac{e}{m_e}N_e(r)p_\varphi$, and the radial dependence of the current density j_φ has the form

$$j_\varphi = -\frac{\lambda e^3E_{0L}^2N_{0e}}{m_e^2\omega_0^3}\frac{r}{R_{\rm ch}^2}\exp\left(-\frac{r^2}{R_L^2}\right). \quad (2.9)$$

Radial profiles of the magnetic field (2.8) and the azimuthal current density (2.9) in a narrow plasma channel are shown in Fig. 2. The magnetic field is maximum at the channel axis and its strength decreases in the radial direction on the characteristic radial scale R_L, which is much larger than the channel radius, $R_L \gg R_{\rm ch}$. However, unlike the case of a wide plasma channel, the magnetic field does not reverse its direction. Such a distribution of the magnetic field results from the presence of only one annular current layer in the plasma channel and is analogous to the magnetic field distribution in a long solenoid.

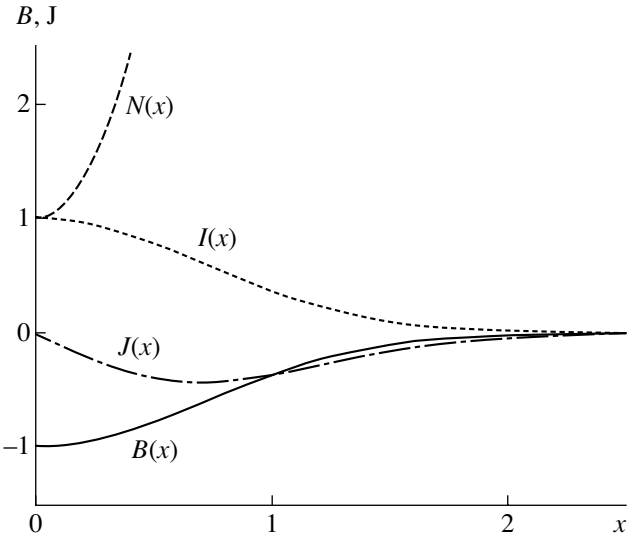

Fig. 2. Spatial profiles of the normalized magnetic field $B = B_z\frac{2m_e\omega_0^3R_L^2}{\lambda ecE_{0L}^2}$, normalized current density $J = j_\varphi\frac{m_e^2\omega_0^3R_{\rm ch}^2}{\lambda e^3E_{0L}^2N_{0e}R_L}$, normalized laser intensity $I = E_0^2(r)/E_{0L}^2$, and normalized electron density $N = N_e(r)/N_{0e}$ along the dimensionless transverse coordinate $x = r/R_L$ for a circularly polarized long ($k_{p0}L \longrightarrow \infty$) laser pulse propagating in a narrow plasma channel $\left(R_{\rm ch} = \frac{1}{3}R_L\right)$.

For an electromagnetic wave of constant amplitude ($R_L \longrightarrow \infty$), and for an arbitrary radial profile of the electron plasma density, Eq. (2.7) is also easy to integrate. Having done this, we obtain the following expression for the axial magnetic field:

$$B_z(r) = \lambda\frac{2\pi e^3E_{0L}^2}{m_e^2\omega_0^3c}N_e(r), \quad (2.10)$$

which, in the nonrelativistic limit, coincides with the corresponding expression derived in [9].

Note that, for a long nonrelativistic laser pulse, the conditions for the applicability of the linear approximation in the momentum of the slow electrons, $e^2E_0^2/\omega_0^2 \gg \mathbf{p}^2$, are satisfied by an ample margin. Note also that the electron density perturbations $\delta N_e \ll N_e(r)$ can be ignored under the inequality

$$\frac{V_E^2}{c^2} \ll k_{p0}^2R_L^2, \quad (2.11)$$

which follows from relationship (1.9).

Conditions (1.18) and (2.11) impose restrictions on the plasma density and on the laser field amplitude and

laser power. For a wide laser pulse, condition (2.1) is satisfied because its right-hand side is large, $k_{p0}^2 R_L^2 \gg 1$, and its left-hand side (the ratio of the electron oscillatory velocity to the speed of light) is small. In this case, inequality (1.18) imposes more stringent restrictions on the laser pulse parameters. For a narrow pulse, condition (1.18) is satisfied by an ample margin and the restrictions on the plasma density and laser field amplitude are replaced by inequality (2.11).

3. SPATIAL DISTRIBUTION OF THE MAGNETIC FIELD EXCITED BY A FINITE-LENGTH MODERATE-INTENSITY LASER PULSE IN A PLASMA CHANNEL

Here, we consider the effect of the finite length of the laser pulse on the magnetic field structure in the plasma channel. If the length L of the laser pulse is comparable to its radius R_L, then, according to Eqs. (1.10)–(1.12) and relationships (1.13)–(1.15), the pulse excites all the three components of the quasistatic current and magnetic field. Let us investigate the simplest case of the propagation of a moderate-intensity ($V_E \ll c$) laser pulse with a low power satisfying condition (1.18) and with large spatial dimensions ($k_{p0}L \gg 1$, $k_{p0}R_L \gg 1$) in a wide plasma channel ($R_{ch} \gg R_L$) under the consistency condition. In this case, to second order in the laser field amplitude, we obtain from Eqs. (1.10)–(1.12) the following expressions for the momentum components:

$$p_r = \frac{e^2}{2m_e\omega_0^2 c k_p^2(r)}\frac{\partial^2}{\partial r\partial\xi}E_0^2(r,\xi), \tag{3.1}$$

$$p_z = \frac{e^2}{2m_e\omega_0^2 c k_p^2(r)}\frac{\partial^2}{\partial\xi^2}E_0^2(r,\xi), \tag{3.2}$$

$$p_\varphi = \frac{\lambda e^2 E_0^2(r,\xi)}{2m_e\omega_0^3}\frac{1}{N_e(r)}\frac{\partial}{\partial r}N_e(r). \tag{3.3}$$

The spatial distribution of the magnetic field in a wide plasma channel can be determined from formulas (1.13)–(1.15) with allowance for relationships (3.1)–(3.3):

$$B_\varphi = -\frac{e}{2m_e\omega_0^2}\frac{\partial^2}{\partial\xi^2}\left(\frac{E_0^2(r,\xi)}{k_p^2(r)N_e(r)}\frac{\partial}{\partial r}N_e(r)\right), \tag{3.4}$$

$$B_r = \frac{\lambda ec}{2m_e\omega_0^3}\frac{\partial}{\partial\xi}\left(E_0^2(r,\xi)\frac{1}{N_e(r)}\frac{\partial}{\partial r}N_e(r)\right), \tag{3.5}$$

$$B_z = -\frac{\lambda ec}{2m_e\omega_0^3}\frac{1}{r}\frac{\partial}{\partial r}\left(E_0^2(r,\xi)\frac{r}{N_e(r)}\frac{\partial}{\partial r}N_e(r)\right). \tag{3.6}$$

Note that the magnetic fields excited by a long laser pulse ($k_{p0}L \gg 1$) do not extend beyond the pulse region. In the case of a short pulse ($k_{p0}L \leq 1$), this assertion is valid only for the axial and radial components of the magnetic field, in accordance with Eq. (1.12) and expressions (1.14) and (1.15). The azimuthal magnetic field excited by a short laser pulse in a plasma channel is nonzero not only in the pulse region but also in the region of the wake plasma wave behind the pulse; in the latter region, however, the azimuthal magnetic field decreases exponentially with distance from the trailing edge of the pulse [30–32].

Using expression (1.17) for the laser pulse shape and formula (1.16) for the electron density profile, we arrive at the following expressions describing the spatial structure of the magnetic fields in a wide plasma channel:

$$B_\varphi(r,\xi) = \frac{2eE_{0L}^2}{m_e\omega_0^2}\frac{1}{k_{p0}^2L^2}\left(1-2\frac{\xi^2}{L^2}\right)\frac{r}{R_{ch}^2} \times \exp\left(-\frac{r^2}{R_L^2}-\frac{\xi^2}{L^2}\right), \tag{3.7}$$

$$B_r(r,\xi) = -\frac{2\lambda ecE_{0L}^2}{m_e\omega_0^3}\frac{\xi}{L^2}\frac{r}{R_{ch}^2}\exp\left(-\frac{r^2}{R_L^2}-\frac{\xi^2}{L^2}\right), \tag{3.8}$$

$$B_z(r,\xi) = -\frac{2\lambda ecE_{0L}^2}{m_e\omega_0^3 R_{ch}^2}\left(1-\frac{r^2}{R_L^2}\right)\exp\left(-\frac{r^2}{R_L^2}-\frac{\xi^2}{L^2}\right). \tag{3.9}$$

Note that, for sufficiently long pulses satisfying the conditions

$$\frac{\omega_{p0}}{\omega_0}k_{p0}L \gg 1, \quad \frac{R_L}{L}, \tag{3.10}$$

where $\omega_{p0} = \omega_p$ ($r = 0$) is the plasma frequency at the channel axis, the magnetic field components B_r and B_z, which are associated with the circular rotation of the plane of polarization of the laser radiation, substantially exceed the B_φ component.

A short laser pulse ($k_{p0}L \leq 1$) propagating in a plasma channel predominantly excites the azimuthal magnetic field component B_φ, while the rotation of the plane of polarization plays a minor role in the excitation of the magnetic fields. In other words, the structure of the magnetic fields is the same as in the case of a linearly polarized pulse.

Note that the excitation of the axial, radial, and azimuthal components of the magnetic field in the interaction of a circularly polarized laser pulse of moderate intensity with an initially homogeneous plasma was considered by Gorbunov and Ramazashvili [17]. They found that the amplitudes of all the magnetic field components are proportional to E_{0L}^4. For the radial and axial components, this result can be readily understood in terms of expression (1.7) for the nonlinear current

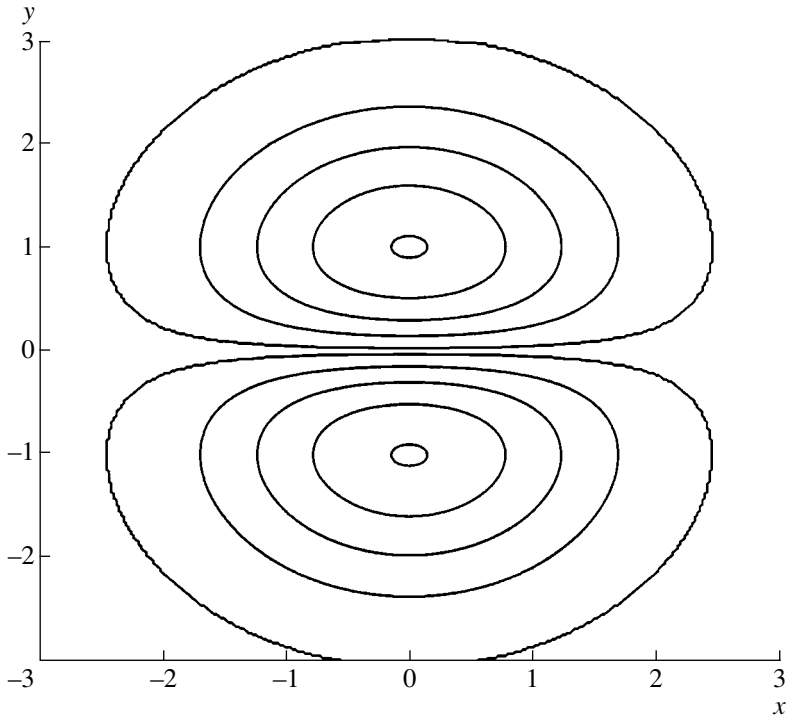

Fig. 3. Magnetic field lines in the plane of the dimensionless variables $y = r/R_L$ and $x = \xi/L$ in the case where a circularly polarized laser pulse whose length satisfies conditions (3.10) propagates in a wide plasma channel.

density. In fact, if the electron density is uniform, then the nonlinear current density (1.7) and the radial and axial magnetic field components (1.14) and (1.15) are proportional to the fourth power of the laser field amplitude. This dependence is determined by relativistic effects and also by the electron density perturbations due to the ponderomotive force effects of the laser radiation.

Let us now consider the magnetic field excited in a plasma channel by a long laser pulse whose length satisfies inequalities (3.10). In this case, the generation of a quasistatic magnetic field is largely governed by the circular rotation of the plane of polarization of the laser pulse and the axial and radial magnetic field components (3.9) and (3.8) appreciably exceed the azimuthal component (3.7). In this case, if the width of the laser pulse is much greater than its length, $B_r \gg L$, then the pulse predominantly generates the radial component of the magnetic field, $B_r \gg B_z$. The magnetic field excited in a plasma channel by a laser pulse whose width is less than its length, $L \gg R_L$, has a substantial axial component, $B_z \gg B_r$.

With allowance for expressions (3.5) and (3.6), the equation for the magnetic field lines,

$$\frac{B_r}{B_z} = \frac{dr}{dz}, \tag{3.11}$$

has the solution

$$\frac{\lambda ec}{2m_e\omega_0^3}\frac{rE_0^2(r,\xi)}{N_e(r)}\frac{\partial}{\partial r}N_e(r) = C. \tag{3.12}$$

Taking into account the laser pulse shape and the electron density profile in the plasma channel, we can reduce this solution to

$$\frac{\lambda ecE_{0L}^2}{m_e\omega_0^3}\frac{r^2}{R_{\rm ch}^2}\exp\left(-\frac{r^2}{R_L^2}-\frac{\xi^2}{L^2}\right) = C, \tag{3.13}$$

where C is an arbitrary constant.

Figure 3 shows the lines of the magnetic field excited by a laser pulse in a wide plasma channel. The direction of the magnetic field depends on the laser polarization. For a right-polarized pulse ($\lambda = 1$), the magnetic field in the axial region points in the positive direction along the z axis and, at large distances from the axis, it points in the opposite direction. For a left-polarized pulse, the magnetic field is oriented in the opposite manner. The magnetic field strength is determined by the concentration of the magnetic field lines and is maximum near the axis of the plasma channel. This magnetic field structure is governed by the azimuthal current, whose density j_φ is described by the expression

$$j_\varphi = -\frac{4\lambda e^3N_{0e}E_{0L}^2}{m_e^2\omega_0^3k_{p0}^2R_{\rm ch}^2R_L^2}r\left(2-\frac{r^2}{R_L^2}\right)\exp\left(-\frac{r^2}{R_L^2}-\frac{\xi^2}{L^2}\right), \tag{3.14}$$

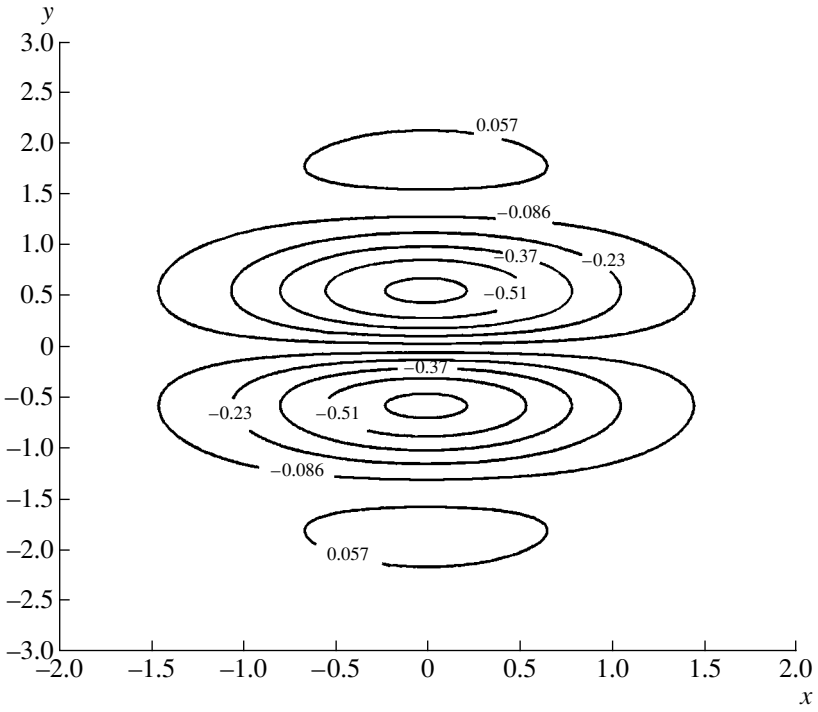

Fig. 4. Contours of the normalized quasistatic current $J = j_\varphi \dfrac{m_e^2 \omega_0^3 k_{p0}^2 R_{\rm ch}^2 R_L}{4\lambda e^3 N_{0e} E_{0L}^2}$ in the plane of the dimensionless variables $y = r/R_L$ and $x = \xi/L$ in the case when a circularly polarized laser pulse whose length satisfies conditions (3.10) propagates in a wide plasma channel.

which derives from formulas (2.4), (1.7), and (1.17) and Eq. (1.12) and differs from expression (2.6) in that it contains the finite length of the laser pulse (in the direction along the z axis).

Figure 4 shows contour lines j_φ = const of the quasistatic current density for a laser pulse propagating in a wide plasma channel. Near the channel axis, the density of the azimuthal current is high and the current itself flows in a counterclockwise direction. As the distance from the axis increases, the current decreases to zero and reverses its direction. The decisive role in the reversal of the magnetic field direction is played by the finite length of the laser pulse and the finite longitudinal size of the region where the azimuthal current flows, rather than by the presence of the second current layer, in which the current density is low. In this case, the spatial distribution of the magnetic field is analogous to that of the magnetic field of a finite-length solenoid and the laser pulse itself resembles a magnetic dipole propagating at the speed of light.

Let us check the conditions for the applicability of the linear approximation in the slowly varying quantities to a moderate-intensity laser pulse with large spatial dimensions. Taking into account expressions (1.6), (1.17), and (3.1)–(3.3), we can see from formula (1.9) that the electron density perturbations are small, $\delta N_e \ll N_e(r)$, under the conditions

$$\frac{V_E^2}{c^2} \ll k_{p0}^2 L^2, \quad k_{p0}^2 R_L^2 . \tag{3.15}$$

Since the quantities on the right-hand side are large and the left-hand side is the small ratio $V_E^2/c^2 \ll 1$, these conditions are satisfied by a large margin. From expressions (3.1)–(3.3) we find that the condition $p_E^2 \gg \mathbf{p}^2$, under which the momentum of the slowly moving electrons can be ignored, also holds. Another condition that relates the laser pulse parameters and the plasma density is given by inequality (1.18). For a pulse with large spatial dimensions ($k_{p0}^2 R_L^2 \gg 1$), it places a more severe restriction on the laser radiation intensity than does the condition that the electron oscillatory velocity be lower than the speed of light.

4. SPATIAL DISTRIBUTION OF THE MAGNETIC FIELD EXCITED BY A RELATIVISTIC LASER PULSE IN A PLASMA CHANNEL

Here, we consider the propagation of a relativistically strong ($p_E \geq m_e c$) laser pulse with large spatial

dimensions ($k_{p0}^2 L^2/\gamma \gg 1$, $k_{p0}^2 R_L^2/\gamma \gg 1$) in a wide plasma channel. In this case, the electron density perturbations are small and, by virtue of relationship (1.9), they can be ignored. From Eqs. (1.10)–(1.12) we then obtain the following expression for the electron momentum components

$$p_r = m_e c \frac{\gamma}{k_p^2(r)} \frac{\partial^2 \gamma}{\partial r \partial \xi}, \quad (4.1)$$

$$p_z = m_e c \frac{\gamma}{k_p^2(r)} \frac{\partial^2 \gamma}{\partial \xi^2}, \quad (4.2)$$

$$p_\varphi = \frac{\lambda e^2 E_0^2}{2 m_e \omega_0^3} \frac{1}{N_e(r)} \frac{\partial}{\partial r}\left(\frac{N_e(r)}{\gamma}\right). \quad (4.3)$$

Taking into account formulas (4.1)–(4.3), from relationships (1.13)–(1.15) we obtain expressions describing the spatial distribution of the magnetic field excited by a relativistic laser pulse in a wide plasma channel:

$$B_\varphi = \frac{m_e c^2}{e}\left\{\frac{\partial}{\partial r}\left(\frac{\gamma}{k_p^2(r)}\frac{\partial^2 \gamma}{\partial \xi^2}\right) - \frac{\partial}{\partial \xi}\left(\frac{\gamma}{k_p^2(r)}\frac{\partial^2 \gamma}{\partial r \partial \xi}\right)\right\}, \quad (4.4)$$

$$B_r = \frac{\lambda e c}{2 m_e \omega_0^3} \frac{\partial}{\partial \xi}\left(E_0^2(r,\xi)\frac{1}{N_e(r)}\frac{\partial}{\partial r}\left(\frac{N_e(r)}{\gamma}\right)\right), \quad (4.5)$$

$$B_z = -\frac{\lambda e c}{2 m_e \omega_0^3} \frac{1}{r}\frac{\partial}{\partial r}\left(E_0^2(r,\xi)\frac{r}{N_e(r)}\frac{\partial}{\partial r}\left(\frac{N_e(r)}{\gamma}\right)\right). \quad (4.6)$$

In the nonrelativistic limit ($p_E \ll m_e c$), relationships (4.4)–(4.6) give expressions (3.4)–(3.6), which imply that the magnetic field components are proportional to the squared amplitude of the electric field of the laser pulse.

We assume that, in the strongly relativistic limit, the laser pulse is described by Gaussian profile (1.17) with fixed spatial dimensions. At the same time, it is known [33] that, for $p_E \gg m_e c$, a laser pulse with an overcritical power is subject to relativistic self-focusing, enhanced by the focusing action of the plasma channel. However, calculations show that, in this case, the transverse dimensions of a laser pulse are reduced insignificantly. Thus, for the parameter values $k_{p0}^2 R_L^2/\gamma = 4$ and $R_L^2/R_{\rm ch}^2 = 0.1$, the radius of the pulse decreases by 25% as it travels a distance equal to one-half of the Rayleigh length. Assuming that the path of the laser pulse is much shorter than the Rayleigh length, taking into account expression (1.17) for the laser pulse shape, using the condition $R_{\rm ch} \gg R_L$, and adopting the ultrarelativistic limit $p_E \gg m_e c$, we obtain from relationships (4.4)–(4.6) expressions describing the spatial distribution of the magnetic field in a wide plasma channel:

$$B_\varphi(r,\xi) = \frac{e E_{0L}^2}{m_e \omega_0^2} \frac{1}{k_{p0}^2 L^2} \frac{r}{R_L^2} \exp\left(-\frac{r^2}{R_L^2} - \frac{\xi^2}{L^2}\right), \quad (4.7)$$

$$B_r(r,\xi) = \frac{\lambda c^2 E_{0L}}{2\omega_0^2} \frac{\xi}{L^2} \frac{r}{R_L^2} \exp\left(-\frac{r^2}{2R_L^2} - \frac{\xi^2}{2L^2}\right), \quad (4.8)$$

$$B_z(r,\xi) = \frac{\lambda c^2 E_{0L}}{2\omega_0^2 R_L^2}\left(2 - \frac{r^2}{R_L^2}\right)\exp\left(-\frac{r^2}{2R_L^2} - \frac{\xi^2}{2L^2}\right). \quad (4.9)$$

For a laser pulse long enough to satisfy the inequalities

$$\frac{\omega_{p0}}{\omega_0} k_{p0} L \gg \frac{p_E}{m_e c}, \quad \frac{R_L}{L}\frac{p_E}{m_e c}, \quad (4.10)$$

the radial and axial components of the magnetic field considerably exceed its azimuthal component. In this case, the excitation of the magnetic field is completely determined by the rotation of the plane of polarization of laser radiation and the magnetic field strength is linearly proportional to the laser field amplitude.

With allowance for relationships (4.5) and (4.6), Eq. (3.11) for the magnetic field lines has the solution

$$\frac{\lambda e c}{2 m_e \omega_0^3} \frac{r E_0^2(r,\xi)}{N_e(r)} \frac{\partial}{\partial r}\left(\frac{N_e(r)}{\gamma}\right) = C. \quad (4.11)$$

For a relativistically strong laser pulse ($p_E \gg m_e c$), this solution takes the form

$$\frac{\lambda c^2 E_{0L}}{2 m_e \omega_0^2} \frac{r^2}{R_L^2} \exp\left(-\frac{r^2}{2R_L^2} - \frac{\xi^2}{2L^2}\right) = C, \quad (4.12)$$

where C is an arbitrary constant. The pattern of the lines of the magnetic field excited by a long relativistic laser pulse in a wide plasma channel differs insignificantly from that shown in Fig. 3, which refers to a weakly relativistic laser pulse. Accordingly, the spatial distribution of the magnetic fields given by expressions (4.8) and (4.9) is analogous to that in the case of a moderate-intensity laser pulse. The only difference is that the dimensions of the region in which the magnetic field is localized are somewhat larger (by a factor of $\sqrt{2}$). The reason for this is that, in the strongly relativistic limit, the magnetic field strength is proportional to the first power of the amplitude of the electric field of the laser pulse.

In the strongly relativistic limit, the plasma density perturbations are small, $\delta N_e \ll N_e(r)$; they can be ignored under the conditions

$$\frac{p_E}{m_e c} \ll k_{p0}^2 L^2, \quad k_{p0}^2 R_L^2, \quad (4.13)$$

which follow from relationships (1.9), (1.6), and (1.17). All of the results obtained in this section are valid under inequalities (4.13), which place restrictions on the laser pulse intensity: although the pulse can be relativistically strong ($p_E \gg m_e c$), its intensity should not exceed the limits imposed by these inequalities.

CONCLUSIONS

In this paper, the generation of a quasistatic magnetic field by a circularly polarized laser pulse in a plasma channel with a parabolic radial electron density profile has been investigated. It is shown that, in a channel with a radially nonuniform electron density, circular rotation of the plane of polarization of moderate-intensity laser radiation leads to the excitation of the radial and axial magnetic field components, whose strengths are proportional to the squared amplitude of the electric field of the laser pulse. The above analysis differs from the conventional analysis of the inverse Faraday effect in an inhomogeneous plasma [9] in that it takes into account not only the excitation of the axial component of the magnetic field but also the excitation of the radial magnetic field component due to the finite length of the laser pulse. The spatial distribution of the magnetic field has been examined and the pattern of the magnetic field lines has been outlined for a relativistic laser pulse with spatial dimensions greater than the plasma wavelength. It has been pointed out that such a field is analogous to the magnetic field produced by a finite-length solenoid. The propagation of a relativistic laser pulse with large spatial dimensions in a wide plasma channel has also been considered, and it has been found that the strength of the radial and axial magnetic fields is proportional to the first power of the laser field amplitude.

Let us now apply formula (4.6) to estimate the strength of the axial magnetic field generated by a circularly polarized relativistic laser pulse under the experimental conditions of [13]. Note that expression (4.6) is valid not only for a plasma channel but also for arbitrary radial variations of the electron density. In the experiments of [13], laser pulses with the wavelength $\lambda_0 = 1.054$ μm, a duration of about one picosecond (10^{-12} s), an intensity of 10^{19} W/cm^2 (in vacuum), and a focal spot size of about 20 μm ($R_L = 10$ μm) (in vacuum) were focused onto a gaseous (helium) target. The density of the ionization-produced helium plasma was about 2.8×10^{19} cm^{-3}. The parameters of the plasma and of laser pulses in those experiments satisfied the applicability conditions for relationship (4.6), specifically, the spatial dimensions of strongly relativistic laser pulses exceeded the plasma wavelength, $k_{p0}^2 L^2 \gg \gamma$ and $k_{p0}^2 R_L^2 \gg \gamma$. Assume first that the electron density in the plasma column produced during the ionization of a gaseous target varies only slightly. Then, under the condition that the plasma density at the peak intensity of the pulse is essentially uniform, formula (4.6) yields the following expression for the maximum magnetic field strength at the pulse axis: $B_z(r = 0, \xi = 0) = \lambda c^2 E_{0L}/(\omega_0^2 R_L^2)$. Suppose next that, as a result of self-focusing, the maximum intensity of the laser radiation in the gas amounts to 10^{20} W/cm^2 [34] and that, in accordance with the energy conservation law, the transverse size of the pulse is equal to 3.2 μm. In this case, the strength of the axial magnetic field is estimated by ≈2.2 MG, which agrees with the experimental value of (2.6 ± 0.6) MG.

Note that, under the experimental conditions of [13], the finite duration of a laser pulse can lead to the generation of weak radial and azimuthal magnetic fields. However, in [13], nothing was said about the detection of such fields. According to formula (4.8), the radial magnetic field is maximum at $\xi = L$ and $r = R_L$: it is given by the expression $B_r = 0.184\lambda c^2 E_{0L}/(\omega_0^2 R_L L)$ and is equal to 4.3 kG, which is almost 500 times weaker than the axial magnetic field. Such a low strength of the radial magnetic field is attributed to the fact that laser pulses have a short duration (about one picosecond) and a long length ($L = 300$ μm). The azimuthal magnetic field is even weaker: according to expression (4.7), it is as low as about 400 G.

It should be stressed that, in [11–13], the results of all the experimental measurements were compared with the theoretical predictions of [15]. It was noted earlier that, in [15], the dependence of the strength of the axial magnetic field on the laser field amplitude for low-energy radiation fluxes was described incorrectly. In addition, for a relativistically strong laser pulse, formula (12) from [15] implies that, as the radiation intensity increases, the axial magnetic field strength decreases and vanishes when the laser field amplitude becomes equal to $e^2 E_{0L}^2/(m_e^2 c^2 \omega_0^2) = 15.801$. From the physical point of view, however, this result seems to be rather strange. The source of erroneous results lies in the fact that, in [15], Eq. (9) for the magnetic field contains not the current associated with the slow electron motion but rather the so-called magnetization current, which was found by summing up the magnetic moments of each electron in a homogeneous plasma and by calculating the total magnetization vector. This procedure for determining the plasma magnetization and magnetization current seems to be incorrect. The correct procedure is to calculate the magnetic field strength and plasma magnetization from Maxwell's equations, which take into account both the nonlinear current $\mathbf{j}_E$ and the current carried by the slowly moving electrons.

The attempt that was recently made in [25] to explain the experimental results of [13] cannot be considered successful. It is only for a plasma electron temperature of about 300 keV that the axial magnetic field obtained in [25] is relatively close to the magnetic fields measured experimentally in [13], but such a tempera-

ture cannot be achieved in ionizing a neutral helium gas by laser pulses. Moreover, some of the theoretical results derived in [25] are erroneous. Thus, formulas (11)–(13) from that paper imply that a circularly polarized relativistic laser pulse excites only the axial and azimuthal components of the magnetic field in a plasma and does not excite the radial component. In this case, however, the magnetic field lines are not closed and the condition $\nabla \cdot \mathbf{B} = 0$ fails to hold. Formulas (11)–(13) in [25] also imply that a linearly polarized laser pulse propagating in a plasma excites not only the azimuthal component of the magnetic field but also its radial component and that, even for an axisymmetric pulse, these two magnetic field components depend on the azimuthal angle, in which case the condition $\nabla \cdot \mathbf{B} = 0$ is again violated. Yet it is well known [35, 36] that a linearly polarized laser pulse propagating in a plasma excites only the azimuthal magnetic field component (in particular, in the region of the wake plasma wave behind its trailing edge).

In the present paper, it has been found that the axial and radial magnetic fields given by expressions (4.8) and (4.9) depend linearly on the amplitude of the electric field of a relativistically strong laser pulse. This linear dependence is associated with restrictions (4.13), which are imposed on the radiation intensity in linear theory (i.e., in the linear approximation in the slowly varying quantities). For larger laser pulse amplitudes, the magnetic field strength is likely to saturate, as evidenced by the results of numerical calculations of the axial magnetic field generated during the self-focusing and channeling of a circularly polarized relativistic laser pulse [24]. However, this problem goes beyond the scope of linear theory: it requires solving a very complicated, strongly nonlinear set of equations with allowance for cavitation effects.

ACKNOWLEDGMENTS

I am grateful to L.M. Gorbunov and N.E. Andreev for their useful remarks. This work was supported in part by the Russian Foundation for Basic Research, project nos. 01-02-16723 and 02-02-16110.

REFERENCES

1. L. P. Pitaevskiĭ, Zh. Éksp. Teor. Fiz. **39**, 1450 (1960) [Sov. Phys. JETP **12**, 1008 (1960)].
2. P. Pershan, Phys. Rev. **130**, 919 (1963).
3. J. van der Ziel, P. Pershan, and L. Malmstrom, Phys. Rev. Lett. **15**, 190 (1965).
4. P. Pershan, J. van der Ziel, and L. Malmstrom, Phys. Rev. **143**, 574 (1966).
5. J. Deschamps, M. Fitaire, and H. Lagoutte, Phys. Rev. Lett. **25**, 1330 (1970).
6. A. D. Steiger and C. H. Woods, Phys. Rev. A **5**, 1467 (1972).
7. D. Talin, V. P. Kaftanjian, and L. Klein, Phys. Rev. A **11**, 648 (1975).
8. A. Sh. Abdullaev and A. A. Frolov, Pis'ma Zh. Éksp. Teor. Fiz. **33**, 107 (1981) [JETP Lett. **33**, 101 (1981)].
9. A. Sh. Abdullaev and A. A. Frolov, Zh. Éksp. Teor. Fiz. **81**, 917 (1981) [Sov. Phys. JETP **54**, 493 (1981)].
10. A. Sh. Abdullaev, Yu. M. Aliev, and A. A. Frolov, Fiz. Plazmy **12**, 827 (1986) [Sov. J. Plasma Phys. **12**, 475 (1986)].
11. Y. Horovitz, S. Eliezer, A. Ludmirsky, *et al.*, Phys. Rev. Lett. **78**, 1707 (1997).
12. Y. Horovitz, S. Eliezer, Z. Henis, *et al.*, Phys. Lett. A **246**, 329 (1998).
13. Z. Najmudin, M. Tatarakis, A. Pukhov, *et al.*, Phys. Rev. Lett. **87**, 215004 (2001).
14. V. Yu. Bychenkov, V. I. Demin, and V. T. Tikhonchuk, Zh. Éksp. Teor. Fiz. **105**, 118 (1994) [JETP **78**, 62 (1994)].
15. Z. M. Sheng and J. Meyer-ter-Vehn, Phys. Rev. E **54**, 1833 (1996).
16. V. I. Berezhiani, S. M. Mahajan, and N. L. Shatashvili, Phys. Rev. E **55**, 995 (1997).
17. L. M. Gorbunov and R. R. Ramazashvili, Zh. Éksp. Teor. Fiz. **114**, 849 (1998) [JETP **87**, 461 (1998)].
18. G. Zeng, Phys. Rev. E **60**, 5950 (1999).
19. G. Zeng and X. He, Phys. Plasmas **6**, 2954 (1999).
20. G. Zeng, Phys. Plasmas **7**, 1539 (2000).
21. G. Shvets, N. J. Fisch, and J. M. Rax, Phys. Rev. E **65**, 046403 (2002).
22. I. Yu. Kostyukov, G. Shvets, N. J. Fisch, and J. M. Rax, Phys. Plasmas **9**, 636 (2002).
23. M. G. Haines, Phys. Rev. Lett. **87**, 135005 (2001).
24. A. Kim, M. Tushentsov, D. Anderson, and M. Lisak, Phys. Rev. Lett. **89**, 095003 (2002).
25. S. P. Zhu, C. Y. Zheng, and X. T. He, Phys. Plasmas **10**, 4166 (2003).
26. S. P. Zhu, X. T. He, and C. Y. Zheng, Phys. Plasmas **8**, 321 (2001).
27. P. Sprangle, E. Esarey, J. Krall, and G. Joyce, Phys. Rev. Lett. **69**, 2200 (1992).
28. P. Sprangle and E. Esarey, Phys. Fluids B **4**, 2241 (1992).
29. N. E. Andreev, L. M. Gorbunov, and V. I. Kirsanov, Phys. Plasmas **2**, 2573 (1995).
30. N. E. Andreev, L. M. Gorbunov, V. I. Kirsanov, *et al.*, Phys. Plasmas **4**, 1145 (1997).
31. N. E. Andreev, L. M. Gorbunov, and A. A. Frolov, Fiz. Plazmy **24**, 888 (1998) [Plasma Phys. Rep. **24**, 825 (1998)].
32. G. Shvets and X. Li, Phys. Plasmas **6**, 591 (1999).
33. A. V. Borovskiĭ and A. L. Galkin, *Laser Physics* (IzdAT, Moscow, 1996), Chap. 12–13.
34. K. Krushelnick, E. L. Clark, Z. Najmudin, *et al.*, Phys. Rev. Lett. **83**, 737 (1999).
35. L. M. Gorbunov, P. Mora, and T. M. Antonsen, Jr., Phys. Rev. Lett. **76**, 2495 (1996); Phys. Plasmas **4**, 4358 (1997).
36. Z. M. Sheng, J. Meyer-ter-Vehn, and A. Pukhov, Phys. Plasmas **5**, 3764 (1998).

Translated by O.E. Khadin

Plasma Physics Reports, Vol. 30, No. 8, 2004, pp. 710–713. Translated from Fizika Plazmy, Vol. 30, No. 8, 2004, pp. 763–766.

LOW-TEMPERATURE PLASMA

Production of XeI(B) and I_2(B) Molecules in the Plasma of a Steady Electric Discharge in Xe/I_2 Mixtures

A. K. Shuaibov, L. L. Shimon, and I. A. Grabovaya

Uzhhorod National University, vul. Pidgirna 46, Uzhhorod, 88000 Ukraine

Received May 6, 2003; in final form, December 22, 2003

Abstract—The production of excited xenon iodides and iodine dimers in the plasma of a longitudinal dc glow discharge is investigated. The discharge was ignited in iodine vapor and Xe/I_2 mixtures at xenon pressures of P(Xe) = 0.1–1.5 kPa and deposited powers of 10–100 W. The current–voltage characteristics of a glow discharge, the plasma emission spectra in the spectral range of 200–650 nm, and the intensities of spectral lines and molecular bands are studied as functions of the deposited power and the xenon partial pressure in a Xe/I_2 mixture. It is found that the discharge plasma emits within the spectral range of 206–343 nm, which includes the 206-nm resonant line of atomic iodine and the XeI(B–X) 253-nm and I_2(B–X) 343-nm molecular bands. The power deposited in the plasma and the xenon pressure P(Xe) are optimized to achieve the maximum UV emission intensity. The 7-W total UV power emitted from the entire surface of the cylindrical discharge tube is achieved with an efficiency of ≤5%. © *2004 MAIK "Nauka/Interperiodica".*

1. INTRODUCTION

The wide use of high-power sources of spontaneous UV and VUV emission in microelectronics, ecology, and medicine have inspired the study and development of active media for electric-discharge lamps based on noble gas monohalogenides and halogen dimers [1]. The most simple of these are low-pressure excimer–halogen lamps pumped by a dc glow discharge [2–5] operating mainly with mixtures of heavy noble gases with Cl_2 or HCl molecules. However, the lifetime of such lamps operating in a static-gas mode does not exceed 100 h per single gas fill [2]. This stems from the attachment of halogen-containing molecules to the metal electrodes and the quartz tube wall, which are significantly heated by a glow discharge at discharge currents higher than 20–30 mA. Insulating the electrodes from a corrosive chlorine-containing plasma (e.g., in low-pressure excimer lamps pumped by a barrier discharge) enables one to increase the lifetime of a sealed-off lamp to 2000 h [6]. The output power and efficiency of a lamp operating on the XeBr 283-nm emission band are 1.5–2 times higher than for lamps operating on the KrCl 222-nm and XeCl 308-nm emission bands. This means that it is expedient to use less corrosive halogens (bromine or iodine) in low-pressure excimer lamps. The use of such working mixtures also holds promise for lamps operating with a dc glow discharge; thus, a lifetime of 1000 h was achieved in a lamp operating on a Xe/I_2 ($P \le 600$ Pa) mixture [7]. In that paper, the main attention was given to the I* emission at $\lambda = 206$ nm. However, conditions for the production of XeI(B) and I_2^* molecules in a dc glow discharge and their contribution to the UV emission from a steady low-density plasma are still poorly studied [8]. These problems have been studied in more detail only for the plasma of a barrier discharge in $Xe(Kr)/I_2$ mixtures at total pressures of 34–50 kPa [9, 10].

This paper is devoted to studying conditions for the production of XeI(B) and I_2(B) molecules in a steady low-density electric-discharge plasma.

2. EXPERIMENTAL SETUP

A glow discharge in a Xe/I_2 mixture was ignited in a cylindrical quartz tube with a transparency at λ = 200-nm of no less than 70%. The inner diameter of the discharge tube was 1.4 cm. The distance between the cylindrical electrodes made of sheet nickel was 19 cm. High-purity iodine crystals were placed in a special socket behind the anode.

The plasma emission was studied using an MDR-2 monochromator and FÉU-106 photomultiplier. The relative spectral sensitivity of the recording system was calibrated by the emission from SI 8-200 U and DVS-25 lamps in the spectral ranges 400–1000 and 200–400 nm, respectively. A glow discharge was supplied by a high-voltage dc power source (J_{ch} = 1–50 mA, $U_{ch} \le 10$ kV). Before puffing xenon, the discharge tube was pumped down to a residual pressure of 5 Pa. When the residual pressure exceeded 30–40 Pa, emission from the 2^+ system of molecular nitrogen appeared within the spectral range of 300–400 nm against the background of the iodine bands. This was accompanied by a decrease in the lifetime of the iodine lamp. In experiments, we used high-purity xenon from the Balashikha Oxygen Works. The discharge tube was cooled with a fan, and the temperature of the socket with iodine crystals was usually close to room temperature.

1063-780X/04/3008-0710$26.00 © 2004 MAIK "Nauka/Interperiodica"

At the maximum discharge current, the tube temperature might exceed the room temperature by 10–15°C; hence, the pressure of the saturated iodine vapor in the tube was no higher than 130–170 Pa [11]. The total UV emission power was measured by the method described in [12]. Since we used a UFS-5 light filter, only the emission power in the wavelength range of $\lambda \le 400$ nm was determined. This fact should be taken into consideration for an I_2 plasma, because it is an intense emission source in the visible and IR spectral regions.

3. PLASMA EMISSION CHARACTERISTICS

The dc glow discharge in Xe/I_2 mixtures was quite homogeneous only at xenon partial pressures of $P(Xe) \le 400$ Pa and average currents of ≥40–50 mA. For such mixtures, a decrease in the discharge current led to the appearance of a bright plasma filament against the weak blue background emission of a diffuse discharge. The diameter of the filament decreased from 8–10 to 2–3 mm with decreasing discharge current. As the xenon partial pressure increased to 1.0–1.5 kPa, the glow discharge existed in the form of a plasma filament (whose diameter decreased with xenon partial pressure) against the background of the weak glow discharge emission throughout the range of the discharge currents under study. Such behavior of the discharge corresponds to the regime of dynamic contraction of a glow discharge. Typical current–voltage characteristics are shown in Fig. 1. For a noncontracted glow discharge, the subnormal and normal stages can be distinguished. For a contracted discharge, the ignition voltage decreases with increasing $P(Xe)$, while the discharge voltage varies nearly in inverse proportion to the average current.

The emission spectra from the plasma of a glow discharge in iodine vapor and Xe/I_2 mixtures are shown in Fig. 2. For a discharge in iodine vapor, the spectrum contains the 206-nm resonant line of atomic iodine and the system of $I_2(B–X)$ vibronic bands within the spectral range of 320–342 nm. In Xe/I_2 mixtures, there is also the quite intense XeI(*B–X*) 253-nm band. The emission intensity from the high-lying ($v = 9, 10$) vibrational levels of $I_2(B)$ (the 318- to 330-nm band system in Fig. 2a) decreases because of the vibrational relaxation in collisions with Xe atoms. For a glow discharge in a Xe/I_2 mixture at $P(Xe) = 266$ Pa, the relative emission intensities of I_2^*, XeI*, and atomic iodine, measured with allowance for the relative spectral sensitivity of the monochromator and photomultiplier, were found to be 1.0/0.3/0.7, respectively. Hence, due to the large width of the molecular bands, the spectral range 230–342 nm contains more than one-half of the total UV emission power from the glow discharge plasma.

The most intense spectral lines of iodine and xenon atoms were observed within the range of 400–600 nm against the background continuum. The emission intensities of the molecular bands and atomic lines as func-

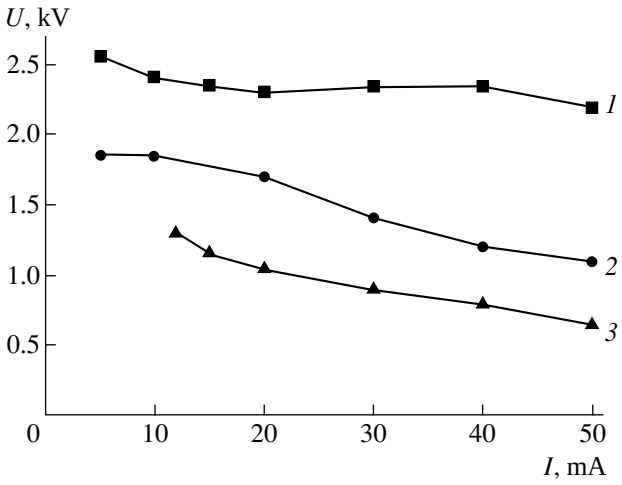

Fig. 1. Current–voltage characteristics of a longitudinal glow discharge in Xe/I_2 mixtures at $P(Xe)$ = (*1*) 133, (*2*) 800, and (*3*) 1600 Pa.

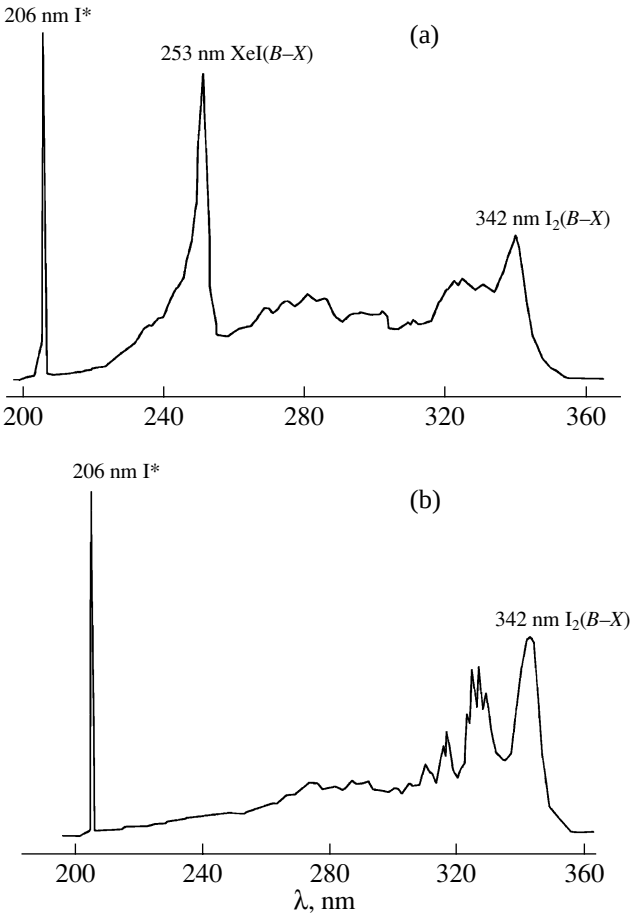

Fig. 2. Emission spectra of a glow discharge in (a) Xe/I_2 mixture at $P(Xe) = 133$ Pa and (b) iodine vapor.

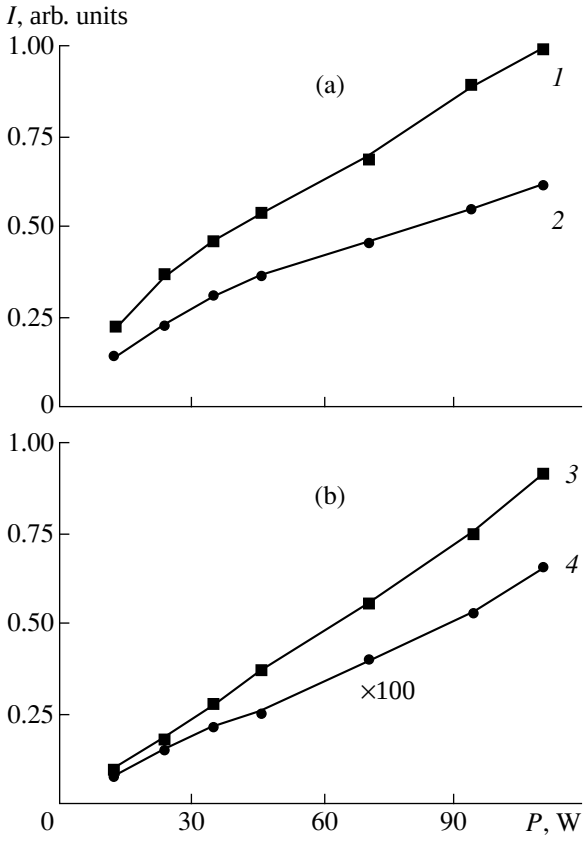

Fig. 3. Emission intensities of (a) the molecular bands and (b) the atomic spectral lines vs. power deposited in a glow discharge in a Xe/I_2 mixture at $P(Xe) = 133$ Pa: (*1*) XeI(*B*–*X*) 253 nm, (*2*) I_2(*B*–*X*) 342 nm, (*3*) II 206 nm, and (*4*) XeI(7p–6s) 476.1 nm.

tions of the power deposited in the discharge are shown in Fig. 3. The increase in the power from 10 to 110 W resulted in a nearly linear increase in the emission intensities of iodine and xenon iodide molecules. The emission intensity of the 253-nm band was approximately twice as high as the intensity of the 342-nm band. The emission intensities of the spectral lines of atomic iodine and xenon also depended almost linearly on the glow discharge power. Therefore, the excitation of atoms in the plasma under study is most probably related to direct electron impacts and (for iodine atoms) to the reaction of the dissociative excitation of iodine molecules by electrons.

Maximum emission intensities of the spectral lines and bands versus the xenon partial pressure and the power deposited in a discharge in Xe/I_2 mixtures

λ, nm	Power, W	Xenon pressure, Pa			
		0.13	0.26	0.80	1.60
206	15	10.3	38.3	16.4	10.2
I*	30	20.5	72.9	25.2	12.6
	45	31.6	100	32.5	–
253	15	0.32	2.09	0.58	0.32
XeI (*B*–*X*)	30	0.48	2.86	0.55	0.18
	45	0.58	0.54	0.48	–
342	15	0.18	0.23	0.1	0.022
I_2 (*B*–*X*)	30	0.29	0.37	0.09	0.018
	45	0.37	0.48	0.07	–

The results of the optimization of the emission intensity of the I_2(*B*–*X*) and XeI(*B*–*X*) bands, as well as the resonant line of atomic iodine, with respect to the xenon partial pressure and the power deposited in the discharge are shown in the table.

It can be seen that the most efficient production of excited molecules takes place in a noncontracted glow discharge at $P(Xe) = 130$–270 Pa. A further increase in $P(Xe)$ (to higher than 270 Pa) affects first of all the emission intensity of the iodine dimer band. The production efficiency of XeI* molecules decreases sharply as $P(Xe)$ decreases from 270 to 130 Pa. At $P(Xe) >$ 130 Pa, the production efficiency of xenon iodide decreases as the discharge power increases to greater than 30 W.

The UV power emitted through the sidewall of discharge tube was as high as 6–7 W at an efficiency of ≤5%. The lamp lifetime for a single gas fill was no shorter than 500 h.

In summary, the study of the production of excited iodine dimers and xenon iodide in a longitudinal dc glow discharge have shown that the UV emission spectrum from the plasma in the spectral range 230–350 nm consists of two broad bands with maxima at λ = 342 and 253 nm, the intensities of which exceed the intensity of the II 206-nm emission line. In contrast to excimer–halogen UV–VUV sources operating with Ar(Kr, Xe)/Cl_2 mixtures, in lamps working with iodine vapor, the resonant line emission of atomic iodine comprises a significant fraction of the total emission. The optimum partial pressure of xenon lies in the range 130–270 nm. For the most uniform stage of a glow discharge (at $P(Xe) \le 130$ Pa), the emission intensities of the molecular bands and the 206-nm line increase linearly with the discharge power in the range of 10–130 W without any tendency to saturation. The maximum UV emission power of 7 W has been achieved with an efficiency of ≈5%.

REFERENCES

1. I. W. Boyd and J.-Y. Zhang, Mater. Res. Soc. Symp. Proc. **617**, J4.4.1 (2000).
2. A. P. Golovitskiĭ and S. N. Kan, Opt. Spektrosk. **75**, 604 (1993) [Opt. Spectrosc. **75**, 357 (1993)].
3. A. I. Panchenko and V. F. Tarasenko, Opt. Spektrosk. **84**, 389 (1998) [Opt. Spectrosc. **84**, 337 (1998)].

4. A. K. Shuaibov, A. I. Dashchenko, and I. V. Shevera, Kvantovaya Élektron. (Moscow) **31**, 371 (2001).
5. A. K. Shuaibov, L. L. Shimon, A. I. Dashchenko, and I. V. Shevera, Zh. Tekh. Fiz. **71** (2), 77 (2001) [Tech. Phys. **46**, 207 (2001)].
6. E. A. Sosnin, M. V. Erofeev, V. F. Tarasenko, and D. V. Shitts, Prib. Tekh. Éksp., No. 6, 118 (2002).
7. M. I. Lomaev and V. F. Tarasenko, Proc. SPIE **4747**, 390 (2002).
8. M. I. Lomaev, A. N. Panchenko, and V. F. Tarasenko, Opt. Atmos. Okeana **10**, 1271 (1997).
9. J.-Y. Zhang and I. W. Boyd, J. Appl. Phys. **84**, 1174 (1998).
10. G. N. Gerasimov, G. A. Volkova, and G. N. Zvereva, in *Proceedings of the 5th International Conference on Atomic and Molecular Pulsed Lasers, Tomsk, 2001*, p. 91.
11. *Properties of Inorganic Compounds: Handbook* (Khimiya, Leningrad, 1983), p. 304.
12. A. K. Shuaibov, L. L. Shimon, A. I. Dashchenko, and I. V. Shevera, Prib. Tekh. Éksp., No. 1, 104 (2002).

Translated by N.N. Ustinovskiĭ

Plasma Physics Reports, Vol. 30, No. 8, 2004, pp. 714–715. Translated from Fizika Plazmy, Vol. 30, No. 8, 2004, pp. 767–768.

BRIEF COMMUNICATIONS

The Presence of a Local Minimum in the Dependence of Breakdown Delay Time on Magnetic Field Strength

K. M.-R. Kishov* and M.-R. G. Kishov**

**Dagestan State University, ul. M. Gadzhieva 43a, Makhachkala, Dagestan, 367025 Russia*

***Dagestan State Technical University, pr. Shamilya 70, Makhachkala, Dagestan, 367015 Russia*

Received April 3, 2002; in final form, December 8, 2003

Abstract—The experimentally observed nonmonotonic dependence of the breakdown delay time on the magnetic field strength is analyzed theoretically. Calculations with allowance for both an increase in the electric field in the avalanche head because of the change in the diffusion coefficients and an apparent increase in the pressure in the presence of a magnetic field demonstrate that such a dependence is indeed possible. © *2004 MAIK "Nauka/Interperiodica".*

1. INTRODUCTION

Electron avalanches are initial macroscopic objects determining the further evolution of breakdown. Their time behavior [1, 2] in the delayed stage of breakdown is very difficult to diagnose; this dictates the necessity of the development of advanced avalanche models. It has been shown experimentally [3, 4] that, both in the longitudinal ($H_\parallel$) and transverse ($H_\perp$) magnetic fields, the breakdown delay time τ_0, which is primarily determined by the time during which an avalanche (or avalanches) evolves to the critical size, can be a nonmonotonic function of the magnetic field (under the conditions of [3, 4], a local minimum was observed in the dependence $\tau_0 = f(H)$. This is difficult to explain in terms of a single electron avalanche, taking into account that, in contrast to the classical concept, an avalanche in a strong electric field can split into space charge bunches [5].

This paper (which is a continuation of papers [2–4]) is aimed at the numerical study of the possibility of the existence of a nonmonotonic dependence $\tau_0 = f(H)$ in the delayed stage of breakdown. The study of this problem is of fundamental importance from the theoretical standpoint, as well as for solving the applied problems of gas insulation. Under experimental conditions such that the oscillation period of a pulsed magnetic field is ~150 μs and the breakdown lasting ~1 μs is synchronized with the maximum magnetic field, we can assume that the field H varies only slightly in the course of breakdown. The time τ_0 is determined from the waveform of the voltage (from the instant at which the voltage reaches its maximum value to the instant when it abruptly falls off). Note that both the classical and state-of-art streamer concepts of the streamer development admit the presence of avalanches propagating at a certain angle to the main direction of the discharge. It is also well known that, when breakdown develops from multiple avalanches, as in the cases under consideration here, the distribution of the field and space charge also predetermine the possibility of developing such avalanches.

2. RESULTS AND THEIR ANALYSIS

It is well known [1] that $\tau_0 = (1/(\alpha_0 v_0))[\ln(J_K/J_0)]$, where J_0 is the current of the seed electrons, J_K is the current by the instant at which the voltage sharply falls off, α_0 is the first ionization coefficient, and v_0 is the drift electron velocity. In the presence of a magnetic field, we have $\tau_H = (1/(\alpha_H v_H))[\ln(J_K/J_0)]$. In terms of the concept of equivalent pressure [6] (the magnetic field action is considered to be equivalent to an increase in the collision frequency), assuming that the ratio J_K/J_0 is weakly sensitive to variations in H, we obtain $\tau_H = [(1 + k^2)/(\alpha_H v_H)]\ln(J_K/J_0)$. Here, $k = \omega\tau$, ω is the Larmor frequency, and τ is the mean free time of a particle.

Taking into account that $\alpha/P = f(E/P)$, where P is the gas pressure and E is the external electric field, we have $\alpha_H = P_0 A\sqrt{(1 + k^2)}\exp[(-BP\sqrt{(1 + k^2)})/(E + \Delta E_H)]$, where A and B are constants and ΔE_H is the increase in the electric field in the avalanche head in the presence of a magnetic field. According to [7], this increase can be estimated from the relationship $r_H = r_0[(3 + k^2)/3(1 + k^2)^2]^{1/2}$, where r_H and r_0 are the radii of the avalanche head in the presence and absence of a magnetic field, respectively.

From the condition that, irrespective of external conditions, the electric field in the avalanche head during the avalanche–streamer transition must be equal to the external field (the Mick condition), we have $E_0 = E_H$, where E_H and E_0 are the electric fields in the avalanche head in the presence and absence of a magnetic field, respectively. The increase in the avalanche field in the longitudinal magnetic field $H_\parallel$ is then $\Delta E_H =$

Table

Gas	α/P (cm torr)$^{-1}$ \ H, kOe	0	12	25	50	75	100	150
Nitrogen	α_0/P	0.0598	0.0594	0.0544	0.0484	0.0444	0.0413	0.0260
	α_H/P	0.0598	0.0605	0.0623	0.0586	0.0519	0.0460	0.0365
Argon	α_0/P	0.0621	0.0610	0.0601	0.0448	0.0310	0.0131	0.0095
	α_H/P	0.0621	0.0632	0.0664	0.0587	0.0514	0.0429	0.0320
Helium	α_0/P	0.0634	0.0603	0.0511	0.0275	0.0112	0.0038	–
	α_H/P	0.0634	0.0712	0.0646	0.0470	0.0412	0.0372	–

$e\exp(\alpha l)/\{4\pi\varepsilon_0 r_0^2[(3+k^2)/3(1+k^2)^2]\}$, because at $H=0$ we have $\Delta E_0 = e\exp(\alpha l)/4\pi\varepsilon_0 r_0^2$. Here, l is the distance covered by the avalanche (for rough estimates, this distance can be assumed to be equal to the interelectrode distance d), e is the electron charge, and ε_0 is a constant.

The table presents the results of calculations of α_0/P and α_H/P as functions of E/P with account taken of the changes ΔE_0 and ΔE_H, respectively. The values of A and B are given in the literature. For example, for He under these conditions, we find $A \approx 3$ and $B \approx 26$, while for nitrogen we have $A \approx 8.8$ and $B \approx 275$. The quantities A and B have dimensions of (cm torr)$^{-1}$ and V/(cm torr), respectively. The values of the dimensionless quantity k are also known.

In the table, the conditions for all of the gases are identical: P = 760 torr, the interelectrode distance is 0.3 cm, and the overvoltage is 10%. The voltages are specified as follows: 11.9 kV for nitrogen, 3.2 kV for argon, and 1.4 kV for helium.

Our calculations have shown that, when ΔE_H is substituted for ΔE_0, a region where α reaches its maximum appears in the dependence $(\alpha/P)_H = f(E/P)_H$, which agrees qualitatively with the experimental results [2–4]. In the case of a multiple avalanche, the interpretation of the problem can be ambiguous, whereas in the case of a single avalanche, the development of breakdown seems to be more monotonic and no minima occur in the dependence $\tau_0 = f(H_\parallel)$. Let us estimate the efficiency with which the magnetic field affects the breakdown. For nitrogen at P = 760 torr, d = 0.1 cm, E/P = 50 V/(cm torr), and H = 100 kOe, we have $\Delta P \approx 10\%$. Under the same conditions, but for H = 200 kOe, we have $\Delta P \approx 40\%$. For argon at d = 0.2 cm, P = 760 torr, E/P = 13 V/(cm torr), and H = 100 kOe, we have $\Delta P \approx$ 20%, whereas for H = 200 kOe, we have $\Delta P \approx 55\%$. For helium under similar conditions, the values of ΔP are equal to 30 and 75%, respectively. Therefore, under identical conditions, the magnetic field more efficiently influences breakdowns in helium, which is quite a natural result.

It is evident that, in the longitudinal field $H_\parallel$, the time τ_0 should be shorter because of the increase in the space charge density in an avalanche, whereas in the transverse field $H_\perp$, this time should be longer because the electron heating slows down. The nonmonotonic effect of the magnetic field on τ_0 may be attributed to a competition of the factors ΔE, ΔE_H, and ΔP at certain strengths of the magnetic field H.

The main result of this study is that the calculated data correlate satisfactorily with the experimental dependences, demonstrating a nonmonotonic effect of the magnetic field on the breakdown delay time. This effect is explained by the presence of avalanches propagating in different directions. The effect is more pronounced during the avalanche–streamer transition.

REFERENCES

1. É. D. Lozanskiĭ and O. B. Firsov, *Theory of Spark* (Atomizdat, Moscow, 1975).
2. M.-R. G. Kishov, Fiz. Plazmy **6**, 1361 (1980) [Sov. J. Plasma Phys. **6**, 746 (1980)].
3. M.-R. G. Kishov, Fiz. Plazmy **19**, 137 (1993) [Plasma Phys. Rep. **19**, 71 (1993)].
4. M.-R. G. Kishov and N. A. Akopdzhanov, Izv. Vyssh. Uchebn. Zaved. Radiofiz. **27**, 383 (1984).
5. A. N. Pavlovskiĭ, L. P. Babich, T. V. Soboleva, and B. N. Shamraev, Dokl. Akad. Nauk SSSR **266**, 840 (1982) [Sov. Phys. Dokl. **27**, 844 (1982)].
6. H. A. Blewin and S. C. Haydon, J. Phys. **151**, 340 (1958).
7. K. Mitani and N. Kubo, J. Phys. Soc. Jpn. **15**, 678 (1960).

Translated by N.F. Larionova